

REPORT DOCUMENTATION PAGE

Form Approved
OMB No. 0704-0188

Public reporting burden for this collection of information is estimated to average 1 hour per response, including the time for reviewing instructions, searching data sources, gathering and maintaining the data needed, and completing and reviewing the collection of information. Send comments regarding this burden estimate or any other aspect of this collection of information, including suggestions for reducing this burden to Washington Headquarters Service, Directorate for Information Operations and Reports, 1215 Jefferson Davis Highway, Suite 1204, Arlington, VA 22202-4302, and to the Office of Management and Budget, Paperwork Reduction Project (0704-0188) Washington, DC 20503.

PLEASE DO NOT RETURN YOUR FORM TO THE ABOVE ADDRESS.

1. REPORT DATE (DD-MM-YYYY)			2. REPORT DATE		3. DATES COVERED (From - To)	
12-20-2001			Fourth Annual Report		15/08/00 - 15/08/01	
4. TITLE AND SUBTITLE			5a. CONTRACT NUMBER			
1997 MURI in RF Photonics: RF Photonics for Array Processing			5b. GRANT NUMBER MURI 1997 GN00014-97-1-1006			
			5c. PROGRAM ELEMENT NUMBER			
6. AUTHOR(S)			5d. PROJECT NUMBER			
Kelvin H. Wagner, University of Colorado, Boulder Dana Anderson, University of Colorado, Boulder Zoya Popovic, University of Colorado, Boulder Randall W. Babbitt, Montana State University Andre Knossen, University of California, Davis Lloyd Griffiths, George Mason University			5e. TASK NUMBER			
			5f. WORK UNIT NUMBER			
7. PERFORMING ORGANIZATION NAME(S) AND ADDRESS(ES)			8. PERFORMING ORGANIZATION REPORT NUMBER 153 6702			
University of Colorado Optoelectronic Computing Systems Center Campus Box 525 Boulder, CO 80309						
9. SPONSORING/MONITORING AGENCY NAME(S) AND ADDRESS(ES)			10. SPONSOR/MONITOR'S ACRONYM(S)			
Dr. William Miceli Office of Naval Research code 313 Ballston Tower #1, Rm. 619 Arlington, VA 22217			Dr. Stephen A. Pappart US Navy SPAWAR Systems Center SSC-SD D825 53560 Hull St, San Diego, CA 92152-5001			
			11. SPONSORING/MONITORING AGENCY REPORT NUMBER			
12. DISTRIBUTION AVAILABILITY STATEMENT			13. SUPPLEMENTARY NOTES			
Unlimited			Distribution Unlimited			
DISTRIBUTION STATEMENT A Approved for Public Release			20020304 088			
Funded by OSD DDR&E						
14. ABSTRACT						
This report covers the fourth year of progress of the 1997 MURI on RF Photonics for Antenna Arrays at the University of Colorado, Montana State University, George Mason University, and the University of California Davis. Novel techniques for optical control and processing of the wideband RF and microwave signals encountered in phased array antennas are being developed, guided by research in spatio-temporal adaptive processing algorithms and active quasi-optical RF antenna arrays. The primary goal of this research is to develop enabling optical techniques that provide dramatic improvements in antenna array performance over conventional RF, optical, and digital techniques, allowing the efficient processing of large broadband antenna arrays. Coherent modulation and detection is made robust and practical by the use of dynamic holography in photorefractive and optical coherent transient media. This report summarizes the teams management, educational, and outreach activities, as well as technical progress in the 4th year on the constituent projects - broadband adaptive optical array processing, spatio-temporal array processing algorithms, coherent-transient true-time delay, photorefractive signal extraction, optical antenna control, and polymer in-line fiber modulators.						
15. SUBJECT TERMS						
Phased array antennas, coherent transients, photorefractive, RF photonics, STAP processing						
16. SECURITY CLASSIFICATION OF:			17. LIMITATION OF ABSTRACT		18. NUMBER OF PAGES	
a. REPORT	b. ABSTRACT	c. THIS PAGE	Unlimited - UL		119	
Unclassified	Unclassified	Unclassified			19a. NAME OF RESPONSIBLE PERSON Kelvin H. Wagner	
			19b. TELEPHONE NUMBER (Include area code) 303 492 4661			

RF Photonics for Array Processing MURI 3rd year summary

1997 Topic: *Photonics in RF Systems*

Funded by the Office of the Secretary of Defense, DDR&E

Attention: **George D. McNeal**,
ONR 313, 800 N Quincy St., Arlington, VA 22217-5660

Principal Investigator: **Kelvin Wagner, CU-ECE**
Dept. of ECE and OCS, Box 425, University of Colorado, Boulder CO, 80309-0425
kelvin@optics.colorado.edu, (303)-492-4661 (5810 FAX)

<http://optics.colorado.edu/MURI>

University of Colorado Co-PI: **Dana Anderson, CU-Physics**

University of Colorado Co-PI: **Zoya Popović, CU-ECE**

George Mason University Co-PI: **Lloyd Griffiths, GMU-EE**

Montana State University Co-PI: **Randall Babbitt, MSU-Phys**

University of California at Davis Co-PI: **Andre Knoesen, UCD-ECE**

1 4th Year Executive Summary

This report summarizes the fourth year of the MURI in RF Photonic Systems which assembles the University of Colorado, the University of California-Davis, Montana State University, and George Mason University into a systems oriented research team investigating the application of photonic techniques to the control and processing of RF phased arrays. Under this MURI funding, the prime contract is administered through the University of Colorado under the direction of Prof. Kelvin Wagner.

Photonic techniques have emerged as the preferred approach to RF communication and remoting tasks throughout the microwave/millimeter-wave bands, when size, weight, power, and dispersion free bandwidth are key factors. In addition, applications such as controlling time delay, spectral filtering, mixing, frequency generation, antenna array control, beam forming, wide-band signal processing, and target recognition are being implemented optically. Much of this development has been driven by the evolution of high frequency photonic devices such as 100 GHz detectors, 40 GHz modulators, 20 GHz lasers, and 3 THz fiber optic transmission and delay lines. Often these technologies have been used as direct replacement

of individual RF components with their optical counterparts, relying on the smaller size and lighter weight of the optical components and waveguides to yield a resulting system advantage. More sophisticated applications utilize the incredibly large bandwidth of optical transmission to simultaneously wavelength-multiplex a large number of RF signals for efficient parallel transmission or to control the element time delays through dispersion. The approach of this MURI team takes RF photonics to an even higher level of sophistication, in which the massive parallelism possible using dynamic volume holography in photorefractive and photon-echo materials enables the implementation of optimal adaptive and nonlinear algorithms for array processing in the optical domain.

The system research groups comprising this MURI team are pursuing several different avenues towards a common goal of inserting photonics into RF array systems. We are developing solutions that build on the strengths of each approach, and identifying the optimal combination of devices, materials, algorithms, and systems. The BEAMTAP approach (Broadband and Efficient Adaptive Method for True-time-delay Array Processing) is being investigated theoretically and implemented experimentally to demonstrate efficient adaptive beam forming using acousto-optic deflectors, traveling-fringes detectors, and photorefractive adaptive weights. The novel physics of optical coherent transients (OCT) are being developed for applications as programmable RF time delays as well as array signal processors, since these nonlinear materials can directly produce the necessary delayed RF signals as photon echoes. Both of these approaches utilize coherent beam forming in the optical domain which can improve the noise figure of optically remoted arrays and optical novelty filtering developed at CU can enable robust RF signal combination even in the presence of phase errors and drifts. Optically controlled quasi-optical active antenna arrays provide a near term test vehicle for optical controlled arrays, allowing rapid switching between polarizations, transmit/receive (T/R) mode, and frequency response, and in addition will demonstrate the capability of producing multiple simultaneous true-time-delay (TTD) beams as a front end for beam-space adaptive optical processors. Optical nonlinearities are being explored as an approach to dynamically solving the problem of signal extraction from small RF antenna arrays. Practical polymeric in-line fiber (PILF) modulators with high-speed coplanar waveguide (CPW) electrode structures are being developed as the front end RF-to-optical transducers for the antenna arrays. All of these efforts are being tied together by investigations of spatio-temporal signal processing algorithms compatible with RF photonic technology, which allows us to evaluate and compare the various optical systems techniques being investigated. As an example system developed as a unique collaboration between MURI team members, and RF antenna array has coupled into a photorefractive optical system for extracting the principle component in the RF signal environment and package as a portable suitcase demonstrator.

7 Quasi-optical Antennas for Optical Processing Front Ends	95
7.1 Smart Lens Array Antennas for RF-optical Front Ends	95
7.2 Feasibility study: QO lens arrays for passive millimeter-wave ranging	100
7.3 Summary of evaluation of progress based on plans from last year	105
8 PILF modulators	109
8.1 Introduction	109
8.2 PILF Modulator	110
8.2.1 Description	110
8.2.2 The PILF as a Phase Modulator	110
8.2.3 Simulation of PILF as a Phase Modulator	111
8.3 Feasability Experiment	112
8.3.1 Description	112
8.3.2 Results	112
8.4 Self-Homodyne Phase Measurement Method	113
8.4.1 Description	114
8.4.2 Results	114
8.5 Future Work	115

2 Education, Presentations, Outreach, and Management

2.1 MURI Team

This MURI effort has directly or indirectly funded the 6 principal investigators, 5 post-doctoral or visiting research scientists, 12 graduate students, 11 undergraduate students, 2 research assistants, and fractions of a financial manager and secretary.

2.1.1 Principal Investigators

The original MURI team of 6 PIs was joined by Andre Knoesen from UC Davis in year 2 year, replacing Ted Weverka. Prof. Andre Knoesen worked on PILF modulators on a separately funded subcontract which ends this year. Weverka's project on coherent optical beam combination for phased array processing is being continued at the University of Colorado as the required front end to the BEAMTAP processor.

Table 1: Principal investigators involved in the RF Photonic Systems program.

* indicates that Weverka ended his participation in the MURI team in Jan 2000.

Researcher	Department	Institution
Prof. Kelvin Wagner	ECE/OCS	CU-Boulder
Prof. Zoya Popović	ECE	CU-Boulder
Prof. Dana Anderson	JILA	CU-Boulder
Prof. William Randall Babbitt	Physics	Montana State University
Dean Lloyd Griffiths	ITE	George Mason University
Prof. Andre Knoesen	ECE	UC-Davis

Zoya Popović and Dana Anderson, Co-PIs, were on sabbatical for 6 months in 2001, with one summer month supported by this project. They continued to work on the MURI research program and gave numerous talks in Germany about their MURI research.

2.2 Students, Post-Doctoral Researchers, and other Personnel

Table 2: Undergraduate students who have been involved in MURI related research during the past year. Again, those who worked on closely related projects in collaboration with the MURI effort are indicated by *.

Undergrad	Status	Position	Advisor	Dept.	Inst.
Eric Hoyt	continuing	Undergraduate	Wagner	OCS	CU
John Jost	Assistant	Undergraduate	Anderson	Phys	CU
Joe Fischer*	continuing	Undergrad	Babbitt	Physics	MSU
Zeb Barber	continuing	Undergrad	Babbitt	Physics	MSU

Table 3: MURI personnel indicating those funded by this program. Those who worked on closely related projects in collaboration with the MURI effort are indicated by *.

Researcher	Status	Position	Advisor	Dept.	Inst.
G.S.Pati	9/99 -1/01	Post-doc	Wagner	OCS	CU
Valeria Damiao	3/01-4/01	Post Doc	Wagner	OCS	CU
Bruce Tieman	3/01-4/01	Post Doc	Wagner	OCS	CU
Kris Merkel	continuing 50%	Research Scientisit	Babbitt	Physics	MSU
Kevin Repasky*	continuing	Research Scientist	Babbitt	Physics	MSU
Mingzhen Tian	continuing	Research Scientist	Babbitt	Physics	MSU
Diego Yankelevich	3/99-present	Adjunct Prof.	Knoesen	EE	Davis
Joe Shamir	8/01-10/01	Visiting MURI fellow	Wagner	OCS	CU
Edilene Fotheringham	continuing	Grad Student	Anderson	JILA	CU
Valeria Damiao	PhD finished Nov 00	Grad Student	Anderson	JILA	CU
Amy Sullivan*	Spring00 OSEP	Grad Student	Anderson	JILA	CU
Greg Kriehn	DoD fellowship	Grad Student	Wagner	OCS	CU
Paulo Silveira	PhD finished 3/01	Grad Student	Wagner	OCS	CU
Friso Schlottau	continuing	Grad Student	Wagner	OCS	CU
Ken Anderson*	PhD finished 5/01	Grad Student	Wagner	OCS	CU
Jim Vian	PhD finished 11/00	Grad Student	Popović	ECE	CU
Darko Popovic*	continuing	Grad Student	Popović	ECE	CU
Paul Smith*	continuing	Grad Student	Popović	ECE	CU
Jack Hong Loui	new 8/01 -	Grad Student	Popović	ECE	CU
Bob Peters*	MS finished 8/01	Grad Student	Babbitt	Physics	MSU
Randy Reibel	continuing	Grad Student	Babbitt	Physics	MSU
Ijaz Zafarullah	transferred 5/01	Grad Student	Babbitt	Physics	MSU
John Campbell	continuing	Grad student	Knoesen	EE	Davis
Liu Ming Wu	new 2/00-	Grad student	Knoesen	EE	Davis
Sam Weaver	left Feb 2000	Prof. Res. Asst.	Wagner	OCS	CU
Leslie Czaia	continuing	Prof. Res. Asst.	Anderson	JILA	CU
Buz Smith	consultant	Financial Admin.		OCS	CU

2.2.1 Students Graduated from the MURI program

1. Jim Vian, November 2000, CU, ECE, PhD, Popovic. Dr. Jim Vian, graduate student, graduated in January 2001, supported since beginning of project. Thesis title: "Optically Controlled Transmit/Receive Lens Arrays for Space-Time Adaptive Processing". Currently with the MIT Lincoln Laboratories.
2. Valeria Damiao, November 2000, CU, ECE, PhD, Anderson
3. Paulo Silviera, March 2001, CU, ECE, PhD, Wagner
4. Ken Anderson , May 2001, CU, ECE, PhD, Wagner

This coming year several more MURI students are expected to graduate including for example Edeline Fotheringham and Greg Kriehn.

2.3 Meetings

The Boulder team meets weekly to exchange information, make presentations, as well as to discuss technical and management details. The entire MURI team gathers once or twice a year for intellectual exchange, discussions, and review regarding scientific progress during the year. One of these meetings is primarily an internal MURI meeting, and the other is a formal review for programmatic purposes. Our third annual review was held in Boulder on October 12 2000 conjunction with the UCLA MURI review on October 13. Plans for the 4th annual review to be held in Washington DC on Nov 30, 2001 were put on hold when the Program Manager, Dr. Steve Pappert of SPAWAR, took a leave from the government.

2.3.1 Third Annual review

Our 3rd annual review was held October 12, 2000 in Boulder in conjunction with the fourth annual UCLA MURI review held on the following day. It was attended by the 6 MURI PIs, all of the CU MURI students, and about 20 industrial advisors and government reviewers. The view graphs from this meeting are available on the web at our MURI home page http://optics.colorado.edu/MURI/3rdannmeet_0.html .

2.3.2 3rd Annual review schedule

RF Photonics Systems 3rd Annual MURI review, Oct 12, 2000

Time	Name	Organization	Title
— Continental Breakfast —			
8:30 - 8:35	Kelvin Wagner	CU	Welcome
8:35 - 8:45	Bill Miceli	ONR	DoD MURI Program Goals
8:45 - 9:15	Kelvin Wagner	CU	RF Photonic Systems Program Overview
9:15 - 9:30*	Guest speaker 1		
9:30 - 9:45	Jim Vian	CU	Optically controlled T/R antenna
9:45 -10:00	Zoya Popovic	CU	Quasi-optical arrays
10:00 -10:15	Dana Anderson	CU	Dynamic Holography for RF photonics
10:15 -10:30	E. Fotheringham	CU	miniature auto-tuning filter
10:30 -10:45*	Tom Mader	LightLogic	
10:45 -11:00	Feedback on Morning Session		
11:00 -11:15	— Coffee Break —		
11:15 -12:15	Lab Tour 1 JILA Labs (Anderson) Quasi-optics lab (Popovic) BEAMTAP and photon echo labs (Wagner) CU Photon Echo lab (Babbitt/Wagner)		
12:15 - 1:00	— Buffet Lunch Break —		
1:00 - 1:30	Greg Kriehn	CU	BEAMTAP
1:30 - 1:45*	Jaap Bregman	NFRA	SKA
1:45 - 2:00	Lloyd Griffiths	GMU	Issues in STAP
2:00 - 2:15	Paulo Silviera	CU	Optical LMS Array Processing
2:15 - 2:30*	Azad Siahmakoun	RHIT	WOMBAT
2:30 - 2:45	R. Babbitt	MSU	Coherent Transients
2:45 - 3:00	K. Merkel	MSU	Coherent Transient True Time Delay
3:00 - 3:15	— Coffee Break —		
3:15 - 3:30*	Nicolas Breuil	Thomson	
3:30 - 3:45	Andre Knobles	UC-Davis	High Speed Polymeric Modulators
3:45 - 4:00	John Campbell	UC-Davis	Modulators for Photonic Array Antennas
4:00 - 4:30	Feedback on Afternoon Session		
4:30 - 5:00	Advisory Board meeting		
4:30 - 6:00	Lab tours and posters in the labs JILA Labs (Anderson) Quasi-optics lab (Popovic) BEAMTAP and photon echo labs (Wagner) CU Photon Echo lab (Babbitt/Wagner)		
6:30 -	Joint CU/UCLA MURI Banquet at Regal Harvest House		

* indicates guest speakers

2.3.3 3rd Annual review attendees

Name	Organization	Contact Info
Dana Anderson	University of Colorado	dana@colorado.edu
Ken Anderson	University of Colorado	kanderso@cafe.colorado.edu
Wm. Randall Babbitt	Montana State University	babbitt@physics.montana.edu
Norman P. Bernstein	Air Force Research Laboratory	norman.bernstein@afrl.af.mil
Jaap D. Bregman	ASTRON	bregman@astron.nl
Nicholas Breuil	Thomson-CSF Detaxis	nicholas.breuil@dextaxis.thomson-csf.com
John Brock	TRW	john.brock@trw.com
George Brost	Air Force Research Laboratory	brostg@rl.af.mil
John Campbell	University of California, Davis	camp@ece.ucdavis.edu
Scott Christensen	University of Colorado	christes@colorado.edu
Charles Cox	MIT	ccox@photronicsinc.com
Alan E. Craig	Montana State University	craig@spectrum.montana.edu
Valeria Damiao	University of Colorado	damiao@spot.Colorado.EDU
Michael Forman	University of Colorado	michael.forman@colorado.edu
Edeline Fotheringham	University of Colorado	fotherin@jila1.Colorado.EDU
Roland A. Gilbert	Sanders	roland.a.gilbert@lmco.com
Lloyd Griffiths	George Mason University	griffiths@gmu.edu
Peter Guilfoyle	OptiComp Corporation	peterg@opticomp.com
Barbara Harris-Holdrege	UCLA	holdrege@ea.ucla.edu
Leo Hollberg	NIST	
Julie Huffman	Lockheed Martin Astronautics	julie.huffman@lmco.com
Saif Islam	UCLA	
Prof. Andre Knoesen	University of California, Davis	knoesen@ece.ucdavis.edu
Gregory Kriehn	University of Colorado	Gregory.Kriehn@colorado.edu
Larry K. Lam	Lockheed Martin Space Systems	Larry.Lam@lmco.com
Scott Lindel	Lockheed Martin	scott.d.lindell@lmco.com
Tom Mader	Light Logic	mader@lightlogic.com
Sagi Mathai	UCLA Electrical Engineering Dept.	sagi@icsl.ucla.edu
Kris Merkel	Montana State University Spectrum Lab	merkel@spectrum.montana.edu
Adit Narasimha	UCLA	
James E Nichter	Air Force Research Laboratory	james.nichter@rl.af.mil
Srdjan Pajic	University of Colorado	Srdjan.Pajic@Colorado.EDU
Stephen A. Pappert	U.S. Navy SPAWAR Systems Center	spappert@spawar.navy.mil
Gour Shyam Pati	University of Colorado	gspati@cafe.colorado.edu
Darko Popovic	University of Colorado	darko.popovic@colorado.edu
Zoya Popovic	University of Colorado	zoya.popovic@colorado.edu
Stephen L. Rankin	NRO	srankin@erols.com
Randy Reibel	Montana State University	reibel@physics.montana.edu
Stefania Romisch	University of Colorado	romisch@boulder.colorado.edu
Robert Rupp	Lockheed Martin	robert.j.rupp@lmco.com
Friso Schlottau	University of Colorado	friso.schlottau@colorado.edu
Bill Schneider	National Reconnaissance Office	schneidb@erols.com
Joseph Shamir	EE Dept. Technion	jsh@ee.technion.ac.il
Azad Siahmakoun	Rose Hulman Institute of Technology	azad.siahmakoun@rose-hulman.edu
Werner E. Sievers	The MITRE Corporation	wsievers@mitre.org
Paulo Silveira	University of Colorado	paulo@colorado.edu
William H. Steier	USC	steier@mizar.usc.edu
Rachael Tearle	University of Colorado	rachael@cafe.colorado.edu
Dean Thelen	Technology Service Corp	dthelen@tsc.com
Terry M. Turpin	Essex Corporation	turpin@essexcorp.com
Jim Vian	University of Colorado	vian@colorado.edu
Kelvin Wagner	University of Colorado	kelvin@cafe.colorado.edu
Eli Yablonovitch	UCLA	ely@ee.ucla.edu
Diego R. Yankelevich	University of California, Davis	yankelev@ece.ucdavis.edu
Weimin Zhou	Army Research Laboratory	wzhou@arl.army.mil

2.3.4 3rd year MURI team Interactions

1. Aug 11-14, 2000: Lloyd Griffiths visits Boulder for discussions with Wagner, Popović, Vian, Kriehn, and Silveira.
2. Aug 4-Oct 20, 2001: Joseph Shamir from Technion in Israel visits with the CU MURI team and collaborates with Wagner on analyzing the BEAMTAP processor using operator algebra.
3. Oct 12 2000, Entire MURI team visits Boulder for the Annual review.
4. Oct 26 2000, Kelvin Wagner visits Sanders for discussions of Signal Processing applications of high speed SLMS.
5. November 2-3 2000, W.R. Babbitt and Randy Reibel visit Boulder for discussions with Wagner group on photon echo based RF processing and Popovich group for technology transfer on broadband Vivaldi array elements.
6. Dec 4-5, 2000: Lloyd Griffiths visits Boulder for discussions with Wagner, Popović, Vian, Kriehn, and Silveira.
7. Dec 19-20, 2000, Kelvin Wagner visits Sanders for an all-day long colloquium/tutorial on advanced applications of optical techniques to signal processing and control of large RF antenna arrays.
8. Jan 8, 2001 Kelvin Wagner visits Prof. Knoesen and students at the University of California Davis.
9. Feb 9, 2001 Jim Harvey from ARL visits UC Boulder for discussions with Z. Popovic and K. Wagner.
10. Feb 19, 2001 Lloyd Griffiths visits Boulder for discussions with Wagner, Popović, Schlottau, Kriehn, and Silveira.
11. Feb 19, 2001 Jim Harvey from ARL visits UC Boulder for discussions with Z. Popovic and K. Wagner.
12. March 2, 2001: Kelvin Wagner visits Rockwell Science Center for discussion on collaboration about optical BEAMTAP.
13. March 8, 2001 Charles Garvin of CTI visits Prof. Wagner at UC Boulder.

14. April 26-28, 2001, Kelvin Wagner visits MSU for discussions with W.R. Babbitt, K. Merkel, R. Cone, A. Rebane, K. Repasky, and students about OCT applications in RF signal processing.
15. May 12-19 Ivan Logere from CNRS lab Aime Cotton in Orsay, France visits CU for experiments and collaboration with Prof Wagner and Ken Anderson on optical scanners for RF signal processing.
16. May 29- June 1, 2001: Prof. Babbit visits CU for Ken Anderson's PhD defense and discussion on collaborations for future proposals.
17. June 1-July 2, 2001 Kelvin Wagner and Ken Anderson visit CNRS lab Aime Cotton in Orsay, France to work with Jean-Louis Legouet on OCT spectrum analyzers for wideband RF applications.
18. June 11, 2001: Kelvin Wagner visits NFRA in Dwingeloo the Netherlands for discussions about the applications of RF photonics for radio astronomical applications of array processing.
19. July 10-11 Ian McMichael from Rockwell Scientific, and Sid Theis (consultant) visit CU for detailed briefing on the modifications to BEAMTAP necessary for radar applications in preparation for a joint proposal.
20. July 16-17, 2001: Jaap Bregman from the NFRA in the Netherlands visits CU for collaborations on coherent photonics applied to radio astronomy based large array processing.
21. September 4-30, 2001: Yasuhiro Awatsuji visits Prof Wagner for collaborations in coherent multiwavelength optical processing.
22. Aug 13-Oct 5, 2001: Prof Joseph Shamir of Technion visits to work on BEAMTAP rigorous operator analysis paper.
23. Oct 19, 2001: Bill Reed from AT&T visits for discussion of the applications of OCT to fiber dispersion compensation.
24. Oct 23, 2001: GE photonics group visits CU for potential collaborations.
25. Oct 24, 2001: Kelvin Wagner attends the Rose-Hulman WOMBAT center review as a member of the advisory board.
26. November 11-21, 2001: Prof. Voloshinov from Moscow State University visits Prof. Wagner at CU Boulder to develop specialized acousto-optic devices.

27. Nov 29-30, 2001: Prof. Wagner visits Prof. Babbitt and Spectrum Labs at MSU.
28. Mark Neifeld of the University of Arizona visited with W. R. Babbitt and Spectrum Lab on several occasions to discuss information capacity, signal fidelity, and delay resolution issues in optical coherent transient devices.
29. The Workshop on Applications of Spectral Hole Burning 2001 was held in Jackson WY, July, 2001, as part of the PQE (Physics of Quantum Electronics) meeting.
30. W. R. Babbitt and his group have worked closely on MURI related research with the researchers in the groups of Rufus Cone, Alex Rebane, and John Carlsten of MSU Physics and MSU Spectrum Lab, including Alan E. Craig, Pete Selin, Tiejun Chang, Zack Cole, Alex Dimitrov. Kris Merkel and Kevin Repasky have been jointly funded by Spectrum Lab and the MURI.
31. Frequent visits from Prof. Harris group members to UC Davis.

2.4 Additional Collaborations and Related Research

The MURI has enabled a wide variety of collaborations among the PIs as well as with other groups. In this section some notable collaborations are discussed and outgrowths from the MURI into new areas are mentioned.

1. Prof. Babbitt assumed the role of the director of Spectrum Labs at Montana State University, which involves dozens of researchers at MSU and elsewhere investigating the applications of Optical Coherent Transient and spectral hole burning technology for memory and signal processing applications.
2. Prof. Babbitt led a team with Prof. Wagner to apply for a DARPA Analog Optical Signal Processing (AOSP) program utilizing Optical Coherent Transients for wideband signal processing, waveform generation, and array processing. The team also included Prof. Rufus Cone, Dr. Alan Craig, and Dr. Kris Merkel, all of MSU, Dr. Randy Equal of Scientific Materials, and Terry Turpin of Essex. Although the proposal was not selected, numerous extremely novel and powerful applications of OCT technology were invented and refined.
3. Prof. Wagner worked with Prof. Popovic and Dr. Mark Rosker and Dr. Ian McMichael of Rockwell Sciences on a DARPA AOSP proposal for the further development of BEAMTAP. Specifically, a fieldable prototype was to be designed and developed for application in jam resistant GPS arrays, time-delay detectors using III-V CCD technology appropriate for BEAMTAP time delays were to be fabricated, and the BEAMTAP

architecture was modified with a front end beamsteering system allowing squint-free broadband operation in radar and surveillance scenarios. Although this proposal was not successful with DARPA, extremely useful collaboratios with industry were developed.

4. Prof. Wagner also led a team with Drs. Al Samuel, Silvio Cardero, and Harry Scmidt from Raytheon in Tucson, to propose the use of 3-dimensional signal processing in the volume of photorefractive crystals for array processing, in order to calculate range-doppler-angle surfaces. This system was to be designed and built at the University of Colorado and tested by Raytheon with real array data in scenarios appropriate for their missile applications.
5. Prof. Wagner also collaborated with Lockheed Martin Corporation on the application of photorefractive phased array processing for large array applications.
6. Prof. Popović collaborated with Prof. Anderson on the demonstration of a 2-channel optical processor for a quasi-optical (QO) receiving array. A complete system was engineered and characterized, starting from the microwave 10-GHz active antenna front end, to the photodetector and RF demodulator circuits. The system is able to adaptively separate a strong jammer from a signal over shared bandwidth. This could not have been accomplished without multidisciplinary experience in microwave engineering, optics, and electronics. The graduate students involved in the project are now competent in both optics and RF engineering, and the first demonstration of a complete system is now practically completed.
7. Prof. Popović collaborated with Prof. Griffiths on adaptive algorithms for lens array antennas. They have applied an LMS adaptive algorithm to a lens antenna array and compared it to a standard 2-D antenna array in terms of noise and adaptation (learning) speed. They are currently working on a paper that summarizes the results and points to the advantages of quasi-optical arrays for adaptive front ends.
8. Profs. Babbitt and Wagner worked together on a DEPSCOR project that investigated applications of photon echo processing to radar systems. This additional interaction greatly benefited the MURI program since it allowed Prof. Wagner to undertake photon echo experiments not supported by the MURI, as well as direct Prof. Babbitt's work beyond true-time-delay towards fully adaptive processing. Recent results include a preliminary demonstration of true-time-delay array beam steering using novel acoustooptic steering techniques in combination with chirped photon echoes (patent pending). [DEPSCOR]

9. Prof. Knoesen collaborated with Prof. Larry Dalton of the University of Southern California to incorporate the new nonlinear polymeric materials developed by Prof. Larry Dalton into modulator devices.
10. Prof. Knoesen collaborated with Prof. Shiao-Min Tseng of the National Tsing Hua University of Taiwan to obtain long interaction length half-couplers used in in-line modulators.
11. Prof. Knoesen collaborated with Intelligent Fiber Optic Systems Inc., Sunnyvale CA. to extend inline fiber devices to tunable in-line filters.
12. Prof. Knoesen collaborated with Prof. James S. Harris of Stanford University to extend inline fiber concepts to in-line GaAs/AlGaAs modulators, filters, detectors, and emitters.

2.4.1 Other related grants

1. "NSF ITR investigating ultrafast non linear optics switching," \$499,000, 2000-2003, PI Kelvin Wagner with Co-PI Frank Wise at Cornell.
2. "Real-time Multibeam Imaging and High-Resolution Spectral Analysis for Large, Wide-band Antenna Arrays", Prof. Wagner, \$350K from the NRO DII, 2/1/2001-10/31/2001.
3. "Quasi-optics," ARO MURI in Quasi-Optical Power Combining, Co-PI: Zoya Popović, with Caltech, UCSB and U of Hawaii.
4. "Low-power electronics for wireless," NSF, \$1.5 million, Co-PI: Zoya Popović, with Varanasi, Maksimovic, Brown.
5. "Adaptive optical processing for arrays in wireless base stations," NSF, \$250K, PIs: Zoya Popović with Dana Anderson. Profs. Popović and Anderson received a NSF grant under the wireless communications initiative to demonstrate how the optical processor developed under this MURI can be applied to wireless channels with interference.
6. "Diversity in wireless systems," NSF wireless program, \$800K, Co-PI: Zoya Popović, Scharf, Varanasi, with U of Wisconsin.
7. "Low-power electronics," ARO MURI, Co-PI: Zoya Popović with U of Michigan.
8. "High performance correlators based on spectral hole burning technology", NASA, PI: Alan Craig, Co-investigators: W. R. Babbitt, J. L. Carlsten, and R. L. Cone, \$2M/year, 4/99-4/04.

9. "Advanced Coherent Transient Systems and Devices," Air Force Office of Scientific Research, PI: W. R. Babbitt, \$457,844 (plus \$9,749 cost-share), 3/98- 2/01.
10. "Wide-Band Optical True-Time-Delay and Adaptive Beamforming," Army Research Office PI: W. R. Babbitt, \$299,199 (plus \$149,899 cost-share) 5/98- 4/01
11. "Optically-controlled RF switch for polarization-diversity wireless communication receiver," NSF wireless program, PIs Zoya Popović, Mahesh Varanasi, Louis Scharf.
12. "MURI in atom optics," PI Dana Anderson.
13. "Low-index polymer structures integrated in in-line fiber devices", UC Micro in collaboration with intelligent fiber optic systems, \$38,080, 1999-2000, PI Andre Knoesen.
14. "Tunable add-drop in-line fiber multiplexer devices for fiber optic systems", UC Core in collaboration with Intelligent Fiber Optic Systems, \$183,083, 1999-2001, PIs Andre Knoesen and Diego Yankelvich.

2.5 Awards and Honors for the PIs and students

1. Zoya Popović and Dana Anderson both received the prestigious Humboldt Award for Senior US Scientists from the German Alexander von Humboldt Stiftung. Zoya was the only engineer to get this award this year, and the youngest. The award supported a 6-month stay in Germany, and the ceremonial part included a visit with the German President Herr Johannes Rau in his palace in Berlin.
2. Zoya Popovic received the ASEE Terman Award, given by Hewlett Packard for simultaneously maintaining a strong research group and developing undergraduate teaching and a textbook before age 40. Specifically, she has authored *Introductory Electromagnetics*, a textbook and student workbook for ECE juniors, published in 2000 by Prentice Hall.
3. Zoya Popovic became a Fellow of the IEEE.
4. Zoya Popovic received the Outstanding Speaker Award at the ONR Workshop on Challenges for Multifunctional Digital Transmit Arrays, Marco Island, Nov. 2001.
5. Prof. Popović gave an invited talk at MWP 2000 on optically controlled Quasi-optical antennas.

J. Vian, Z.Popović, "Optical Control of Microwave Circuits and Antennas," *Invited Talk, IEEE MWP Topical Meeting*, Oxford, UK, September 2000.

6. Friso Schlottau was awarded the best poster award at the MWP 2001 conference. Kelvin H. Wagner, Greg Kriehn, and Friso Schlottau, Wideband All-optical BEAM-TAP, IEEE Microwave Photonics meeting, Long Beach, Oct 2001 (moved to Jan 2002).
7. Randy Babbitt, Program subcommittee member, Dynamic Holography, Wavemixing, Photorefractives, and Storage, Conference on Lasers and Electro-Optics, Baltimore, Maryland, May 6-11, 2001.
8. Randy Babbitt, Chair of program subcommittee, Holography, Wavemixing, Photorefractives, and Storage, Conference on Lasers and Electro-Optics 2002.
9. Randy Babbitt, Co-organizer, Spectral Holeburning, Single Molecules, and Related Spectroscopies 2003, Bozeman, MT, July 2003.

2.6 MURI Publications

2.6.1 Papers published in 2001 (since 8/15/00)

1. M.Z. Tian, R. Reibel, and W. R. Babbitt, Demonstration of optical coherent transient true-time delay at 4 Gbits/s Optics Letters, 26 (15): 1143-1145, Aug 1 2001 .
2. M. Tian, J. Zhao, Z. Cole, R. Reibel, and W. R. Babbitt, Dynamics of Broadband Accumulated Spectral Gratings in Tm³⁺: YAG, JOSA B 18, 673-8 (2001).
3. C. Sjaarda Cornish, W. R. Babbitt, and L. Tsang, Demonstration of highly efficient photon echoes," Optics Letters 25, 1276-8 (2000). (Related work funded by AFOSR)
4. K. D. Merkel, R. D. Peters, P. B. Sellin, K. S. Repasky and W. R. Babbitt, Accumulated programming of a complex spectral grating, Optics Letters, 25 (22): 1627-1629 Nov 15 2000.
5. R. Reibel, Z. Barber, M. Tian and W. R. Babbitt, Temporally overlapped linear frequency chirped programming for true-time delay amplification," submitted to Opt. Lett.
6. Paulo E. X. Silveira, G. S. Pati and Kelvin H. Wagner, Optical FIR Neural Networks, accepted for publication Applied Optics, 20002
7. Paulo E. X. Silveira, G. S. Pati and Kelvin H. Wagner, Experimental demonstration of an optoelectronic sonar adaptive array, to be submitted to Applied Optics, December 2001.
8. D.Z. Anderson, V. Damaio, D. Popović, Z. Popović, S. Romanish, and A. Sullivan, Optical Carrier Suppression by two-beam coupling in a photorefractive medium,
9. D.Z. Anderson, V. Damaio, E. Fotheringham, D. Popović, Z. Popović, S. Romanish, and A. Sullivan, Optically Smart Active Antenna Array,

10. D.Z. Anderson, V. Damiao, E. Fotheringham, "Photorefractive two-beam coupling modules", Applied Optics.
11. Damiao VB, Manuzak DL, Bickel WS, et al. Two-beam coupling modules for photorefractive optical circuits Applied Optics, 40 (20): 3365-3370 JUL 10 2001
12. Damiao VB, Fotheringham E, Shkunov V, et al. Photorefractive BaTiO₃ spheres and spherical disks Optics Letters, 26 (9): 611-613 MAY 1 2001
13. Anderson D, Damiao V, Popovic D, et al. -70 dB optical carrier suppression by two-beam coupling in photorefractive media, Applied Physics B, 72, pp. 743-748, 2001.
14. E. Fotheringham, S. Romisch, P. Smith, D. Popovic, D. Anderson, Z. Popovic, A lens antenna array with adaptive optical processing, Submitted to the special issue of IEEE Trans. on Antennas and Propagation on Wireless Communications: (July 2001)
15. T J. Vian, Z. Popović, A transmit/receive active antenna with fast low-power optical switching, *IEEE Trans. on Microwave Theory and Techniques Vol 48, No. 12*, pp 2686-2691, Dec. 2000
16. LM Wu , A Knoesen Absolute absorption measurements of polymer films for optical waveguide applications by photothermal deflection spectroscopy J Polymer science pol phys, 39 (22): 2717-2726 NOV 15 2001
17. E Mao, D.R. Yankelevich, C.-C Lin, et al. Narrow-band light emission in semiconductor-fibre asymmetric waveguide coupler Electronics Letters, 36 (16): 1378-1379 AUG 3 2000
18. C. Arft, D.R. Yankelevich, A. Knoesen, E. Mao, J. S. Harris, "In-Line Fiber Evanescent Field Electro-optic Modulators," Journal of Nonlinear Optical Physics and Materials, Vol. 9, No. 1, 2000, p. 79-94.
19. E. Mao, D.R. Yankelevich, C.-C. Lin, O. Solgaard, A. Knoesen, J.S. HarrisJr., "Narrow-band light emission in semiconductor-fibre asymmetric waveguide coupler", Electronics Letters, vol.36, No.16, IEE, 2000, p. 1378-9.

2.6.2 Conference Presentations during 2001 (since 8/15/00)

1. Gregory Kriehn, Paulo E. X. Silveira, G. S. Pati, Friso Schlottau and Kelvin H. Wagner, "BEAMTAP RF-photonic adaptive-array processing", Interactions between Microwaves and Optics summer school, Autrans France, August 2000. [MURI]
2. Gregory Kriehn, G. S. Pati, Paulo E. X. Silveira, Friso Schlottau, Kelvin H. Wagner, Daniel Dolfi and J. P. Huignard, "Demonstration of optical beam forming using BEAM-TAP", Invited Talk, IEE Microwave Photonics MWP-2000, Oxford UK, September 2000. [MURI]

3. G. Kriehn, F. Schlottau, G. S. Pati, and K. Wagner, "Demonstration of RF Photonic Beam Forming using the BEAMTAP Algorithm," OSA Topical Meeting on *Optical Computing*, January 2001.
4. G. Kriehn and K. Wagner, "Experimental Adaptive Beam Forming with Polarization Read-Write Multiplexing using BEAMTAP," The International Topical Meeting on Microwave Photonics MWP 2001, January, 2002.
5. F. Schlottau and K. Wagner, "RF Photonics for Simultaneous Multiple TTD Beam-forming for 2-D Antenna Arrays," The International Topical Meeting on Microwave Photonics MWP 2001, January 2002.
6. K. Wagner, Greg Kriehn, Friso Schlottau, Wideband All-optical BEAMTAP, The International Topical Meeting on Microwave Photonics MWP 2001, January 2002.
7. Ken E. Anderson and Kelvin H. Wagner, Demonstration of Chromatic Dispersion Compensation Using Spectral Holography, Persistent Spectral Hole Burning 2001, Taiwan, 2001.
8. G. Kriehn, F. Schlottau, and K. Wagner, "Optically-Implemented 2-D Beam Steering and Jammer Nulling using BEAMTAP," submitted to ICO Topical Meeting on *Optics in Computing*, SPIE, April 2002.
9. Kelvin H. Wagner, Friso Schlottau, and Jaap Bregman, Array Imaging Using Spatial-Spectral Holography, submitted to ICO Topical Meeting on *Optics in Computing*, SPIE, April 2002.
10. J. Vian, Z. Popović, "Optical Control of Microwave Circuits and Antennas," *Invited Talk, IEEE MWP Topical Meeting*, Oxford, UK, September 2000.
11. T J. Vian, Z. Popović, Smart lens antenna arrays, *2001 IEEE International Microwave Symposium Digest*, pp.129-132, Phoenix, Arizona, May 2001.
12. J.A. Hagerty, Z. Popović, Passive Millimeter-Wave Ranging using Discrete Lenses with Wave-Front Coding, *2001 European Microwave Conference Digest*, pp.421-424, London, Sept. 2001.
13. T J. Peeters Weem, Z. Popovic, A method for determining noise coupling in a phased array antenna, *2001 IEEE International Microwave Symposium Digest*, pp.271-274, Phoenix, Arizona, May 2001.
14. Z. Barber, R. Reibel, and W. R. Babbitt, "Applications of Binary Phase Shift Keying for Inhomogeneously Broadened Materials" Optical Science and Laser Technology Conference, Bozeman, Montana, August 14-16, 2000, poster.
15. K. Merkel, P. B Sellin, R. D. Peters, K. S. Repasky and W. R. Babbitt, "Accumulated Complex Spectral Gratings Using a Frequency Stabilized Laser," Optical Science and Laser Technology Conference, Bozeman, Montana, August 14-16, 2000.

16. M. Tian, R. Reibel, and W. R. Babbitt, "GHz Band True Time Delay and Auto-Correlation Via Accumulated Picosecond Photon Echo Process" Optical Science and Laser Technology Conference, Bozeman, Montana, August 14-16, 2000.
17. M. Tian, R. Reibel, and W.R. Babbitt, "Broadband true-time-delay with optical coherent transients," in Conference on Lasers and Electro-Optics, Technical Digest (Optical Society of America, Washington DC, 2001), May 2001, Baltimore, MD.
18. N. L. Seldomridge, R. Krishna Mohan, W. R. Babbitt and K. D. Merkel, "Steady-state accumulated complex spectral gratings for correlation signal processing" in Conference on Lasers and Electro-Optics, Technical Digest (Optical Society of America, Washington DC, 2001), May 2001, Baltimore, MD. (Related work funded by NASA and MURI)
19. R. Reibel, Z. Barber, M. Tian, W. R. Babbitt, "Temporally Overlapped Linear Frequency Chirp Programming for True Time Delay Applications," poster, Holeburning, Single Molecules, and Related Spectroscopies, November 18-23, 2001, Taipei, Taiwan.
20. M. Tian, R. Reibel, Z. Barber, W. R. Babbitt, "Broadband true-time delay in Tm:YAG," poster, Holeburning, Single Molecules, and Related Spectroscopies, November 18-23, 2001, Taipei, Taiwan.
21. M. Tian, R. Reibel, Wm. R. Babbitt, " Demonstration of broadband true-time delay with optical coherent transient," MWP'2001, January 2002, Long beach, CA.
22. W. R. Babbitt, "Optical Coherent Transient Signal Correlators: Science and Applications", 2001 Physics of Quantum Electronics Conference, Snowbird, UT , January 2001.
23. M. Tian, Z. Barber, T. Chang, R. R. Reibel, and W. R. Babbitt F (F Invited Speaker), "The Effects of Optical Nutation on Stimulated Photon Echoes," Holeburning, Single Molecules, and Related Spectroscopies, November 18-23, 2001, Taipei, Taiwan. (Related work funded by AFOSR)
24. Z. Barber, R. Reibel, M. Tian, W. R. Babbitt, "Application of Phase Modulated Optical Signals to Inhomogeneously Broadened Materials," poster, American Physical Society Annual Meeting, March 11, 2001, Seattle, WA.
25. R. Reibel, Z. Barber and W. R. Babbitt, "Amplification of High Bandwidth Phase Modulated Signals at 793 nm," American Physical Society Annual Meeting, March 2001, Seattle, WA.
26. M. Tian, R. Reibel, and Wm. R. Babbitt, "Multi-gigahertz true-time-delay with optical coherent transient," American Physical Society Annual Meeting, March 2001, Seattle, WA.
27. Joe Fischer, Zeb Barber, Randy, Reibel, Mingzhen Tian, and Randy Babbitt, "Linear Phase Chirp Programming for OCT's," Optec2001, (Bozeman, MT, August, 2001)

2.6.3 Patents and Applications

1. Joint Invention of Montana State University and Univ. of Colorado “Method and Aparatus for variable time delay optical coherent transient signal processing” International Application No. PCT/US00/24813.

2.7 Classes taught by PIs relating to MURI research

Dr. Wagner and Dr. Anderson jointly taught a graduate-level Advanced Optics Lab in Fall of 2001 developed for interdisciplinary students with interests in Chemistry, Physics, and Electrical Engineering. Several of the MURI graduate students were involved either as TAs or in taking the class.

Last year Prof. Popović taught a new special topics graduate course *RF/optical techniques*, that covered some common methods and components used at both RF and optical frequencies (wavelengths). The objective of the course was to present two different views of the same electromagnetic technique, phenomenon, or circuit component. Examples of methods that were compared include: Fourier optics and antenna analysis, Gaussian beams at optical and millimeter waves, diffraction theory, and basic field theorems. Examples of components that are compared include: polarizers, lenses, waveguides, directional couplers, retroreflectors, phase conjugators, and soliton transmission structures. The course concluded with a conference where students presented projects they worked on during the last month of the course. The presentations were judged by industry members, and Best Paper Award was given. A digest of this mini conference was published for assessment purposes (available upon request).

Zoya Popović taught a class in rf-optical techniques at the Technical University in Munich during her sabbatical. A part of the class was shared with Prof. Andreas Cangellaris from the University of Illinois at Urbana-Champaign. It was taken by around 15 graduate students.

1. Wagner, CU ECEN 5696, Fourier Optics, Fall 2000, graduate.
2. Wagner and Anderson, CU ECEN 5606, Advanced Optics Lab , Fall 2001, graduate.
3. Popović, CU ECEN 5004, RF/optical techniques, Spring 1999, graduate.
4. Popović, CU ECEN , Transmission/Antenna Lab, Fall 2001, graduate.
5. Babbitt, MSU Physics 222, Honors General and Modern Physics, Spring 2001, undergraduate.
6. Babbitt, MSU Physics 500, Optical Signal Processing Seminar Spring 2001, graduate.

7. Babbitt, MSU Physics 500, Optical Signal Processing Seminar Fall 2001, graduate.
8. Babbitt, MSU Physics 500-14, Optical Coherent Transient Seminar Spring 2001, graduate.
9. Babbitt, MSU Physics 500-14, Optical Coherent Transient Seminar Fall 2001, graduate.
10. Babbitt, MSU Physics 353, Holography-Laser Photography, Spring 2001, undergraduate.
11. Knoesen, UC Davis EEC236, Nonlinear Optical Applications, Fall 2001, graduate.

3 Continued Experimental BEAMTAP Progress

Principal Investigator: Kelvin Wagner, University of Colorado, Dept of ECE

This year in BEAMTAP, we have investigated methods by which the read-write isolation could be improved upon in order to achieve successful jammer nulling. A new polarization-angle read-write multiplexing technique has been developed in order to stabilize the isolation, and experimental results have been obtained with the new system. The results show stable read-write isolation in excess of 45 dB, which will allow for up to 45 dB of jammer nulling when the feedback loop is closed. The new system is based upon using the parallel tangents, equal curvature condition¹ in a uniaxial photorefractive crystal.

3.1 Read-Write Multiplexing

Although previous architectures using read-write multiplexing have already been investigated, and an experimental system using an SBN photorefractive crystal in a symmetrical beam geometry has already been implemented, the isolation achieved (40 dB) was only stable over a short duration of time (second to half a minute time scales). We believe this is due to the anisotropy of the crystal rotating as a function of time as a result of large space charge fields generated within the crystal when using high intensity beams. The fields generated induce local stresses and strains within the crystal lattice—which give rise to the photorefractive effect—but if strong enough, could also affect the global properties of the material. This is problematic for read-write multiplexing schemes, such as the one involving SBN, described in detail in last year's report, which require that pure polarization eigenstates be launched into the crystal as the individual reading and writing beams. If the eigenaxes of the crystal rotate under the globally induced stresses and strains, then the pure horizontal and vertical polarizations initially launched into the crystal no longer project into single eigenstates; instead, they project into both ordinary and extraordinary polarizations under the rotated coordinate frame. This causes the reading and writing beams to mix polarizations so that the writing beam now contains an extraordinary component, which used to be purely \hat{o} -polarized, that will write a new grating with the read beam. Light will diffract off this new grating, and a component of the write beam will now leak through into the read beam. Furthermore, because the extraordinary polarization will be efficiently diffracted, a large portion of this beam can be detected at the output, thereby limiting the isolation and available feedback gain to enable efficient jammer nulling.

In order to solve this problem, this year we investigated a read-write multiplexing scheme which did not just use polarization to encode the reading and writing beams. Instead, the beams were encoded by both polarization and angle, so that an additional degree of freedom was introduced to maintain the orthogonality of the two beams. We used a 45°

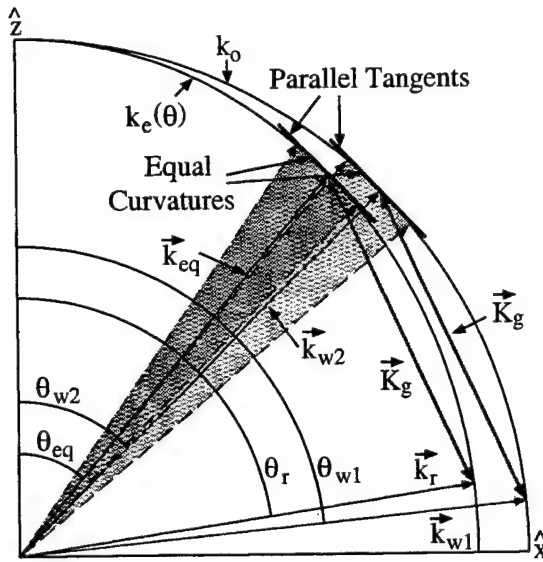


Figure 1: Geometry which describes the parallel tangents, equal curvature condition. Two ordinary polarized beams, \vec{k}_{w1} and \vec{k}_{w2} with angles θ_{w1} and θ_{w2} , respectively, write a grating \vec{K}_g in the photorefractive crystal. The grating is read out by an extraordinary polarized beam \vec{k}_r at an angle θ_r , producing a diffracted beam \vec{k}_{eq} at an angle θ_{eq} . Both the writing beam \vec{k}_{w2} and the diffracted beam \vec{k}_{eq} can subtend a large angular bandwidth while still maintaining excellent Bragg matching.

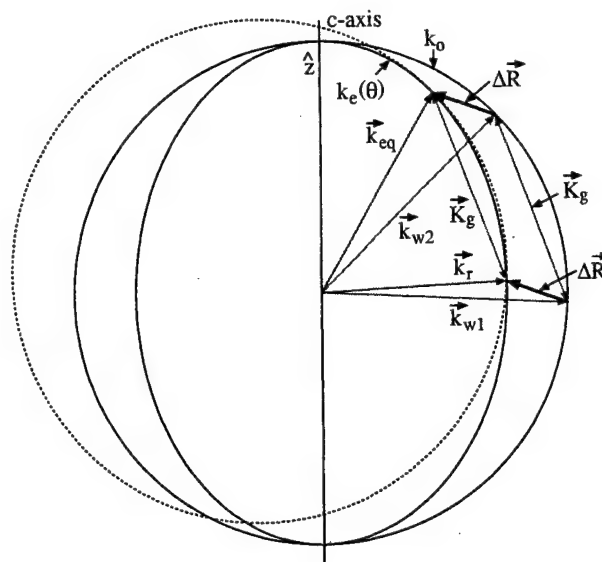


Figure 2: Derivation by which the angles of the 4 beams are found using the parallel tangents, equal curvature condition. The ordinary \vec{k} -circle is translated by $\Delta \vec{R}$ to the parallel tangents, equal curvature angle on the ellipse, and a second intersection between the translated circle and ellipse determines the angle of the extraordinary read beam θ_r . Translating from the read beam and parallel tangents, equal curvature angle by $-\Delta \vec{R}$ determines the two writing beam angles, θ_{w1} and θ_{w2} , respectively.

cut BaTiO₃ crystal using the parallel tangents, equicurvature condition¹ to maximize the angular aperture that could be processed by our system. This method first matches the tangents and curvatures of the ordinary and extraordinary k -surfaces so that there is a large angular aperture where excellent Bragg matching can occur between the reading and writing beams. This is shown in Fig. 1. The geometry is such that the k -vector \vec{K}_g of the grating written between the two ordinary beams with k -vectors \vec{k}_{w1} and \vec{k}_{w2} at angles θ_{w1} and θ_{w2} , respectively, will be Bragg matched to the extraordinary polarized reading beam when read out with a k -vector \vec{k}_r at an angle θ_r . The diffracted output angle θ_{eq} with a k -vector \vec{k}_{eq} is chosen so that both the tangents to the ordinary and extraordinary surfaces, as well as their curvatures, are matched at θ_{w2} and θ_{eq} . This means that both the first and second order Bragg matching conditions are satisfied at these angles, so that if one of the writing beams contains a large angular spectrum and multiple grating \vec{K}_g vectors are recorded within the material, the entire angular spectrum can still be Bragg matched and read out using the

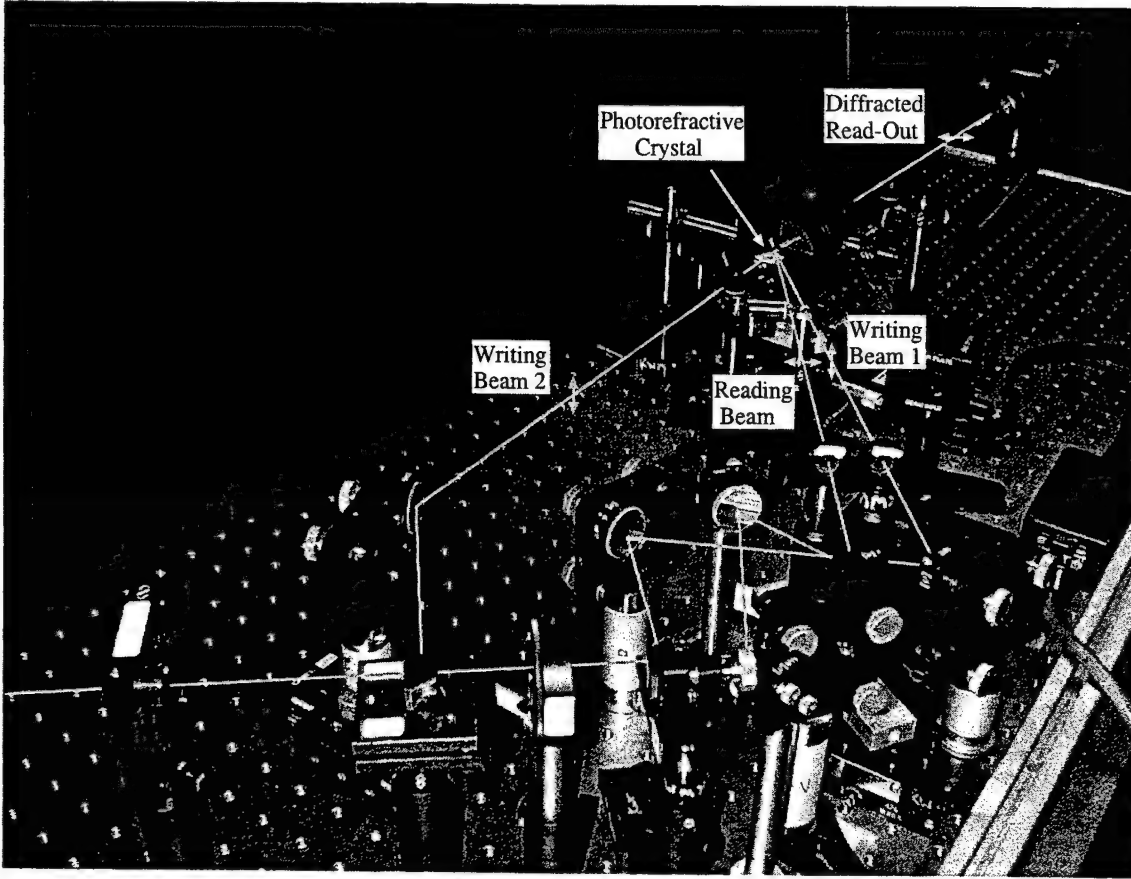


Figure 3: Experimental setup using the parallel tangents, equal curvature geometry. Two ordinary write beams are used to write a grating in the photorefractive crystal, one of which contains a wide angular aperture. The extraordinary polarized beam efficiently reads out the hologram, reconstructing the wide angular aperture recorded in the BaTiO₃ crystal.

reading beam \vec{k}_r .

Figure 2 shows the method by which the angles for the parallel tangents, equal curvature condition are chosen. The ordinary k -circle is first translated by a vector $\Delta\vec{R}$ to the parallel tangents, equal curvature angle, which is given by¹

$$\cos(2\theta_{eq}) = \frac{n_o^{10/3} - n_o^{2/3}n_e^{8/3} - n_e^{10/3}}{n_o^{10/3} + n_o^{2/3}n_e^{8/3} + n_e^{10/3}}, \quad (1)$$

so that the two surfaces are brought into coincidence. Then, a second intersection between the circle and ellipse is looked for, which will determine the angle of the extraordinary polarized read beam θ_r . However, at the exact parallel tangents, equal curvature condition, there is only one additional intersection point, which occurs at an angle greater than 180°. Since this is an inconvenient geometry to work with, the symmetry of the system can be broken by deviating away slightly from the exact parallel tangents, equal curvature condition by a degree or two. This, then, produces a second intersection point at an angle close to

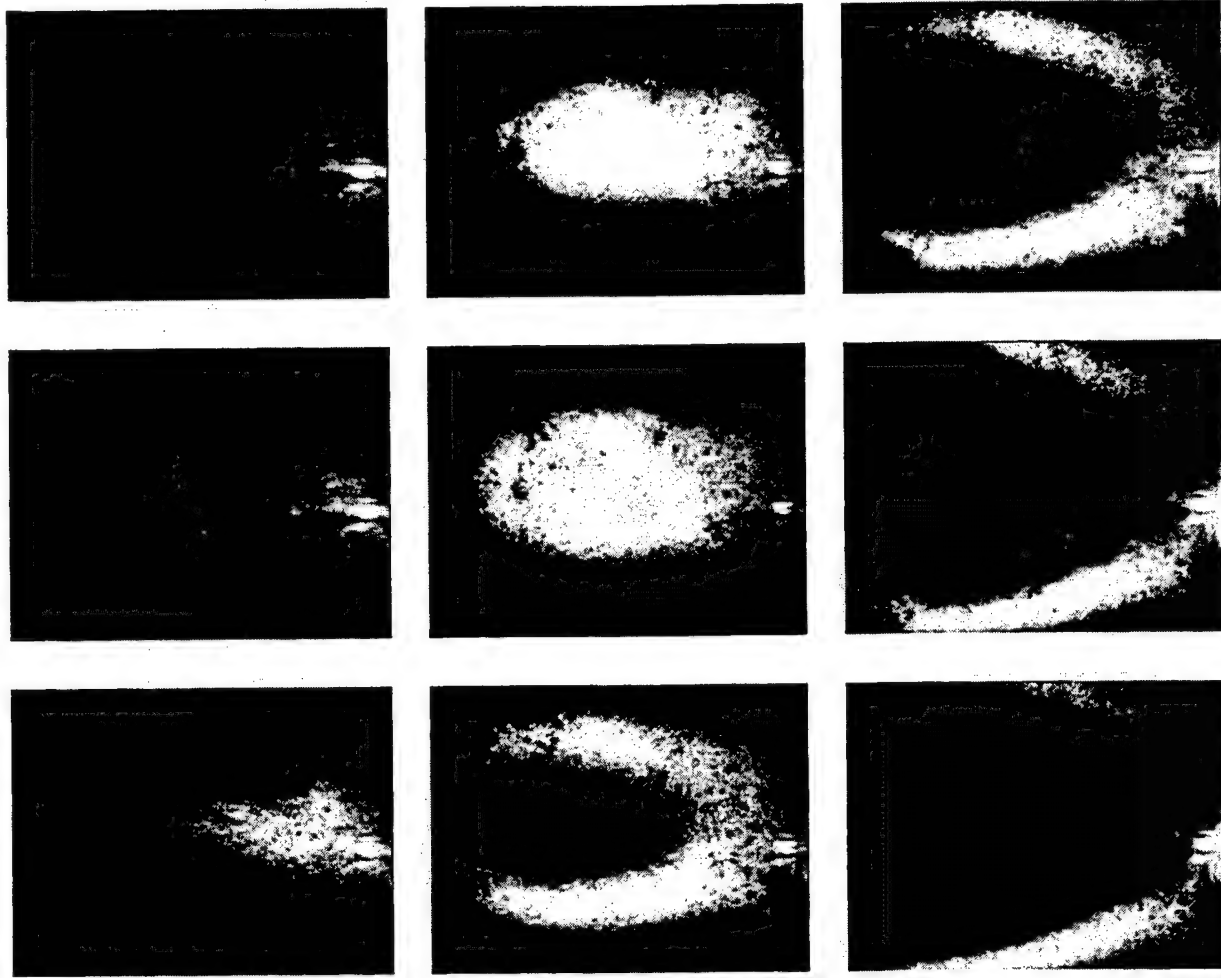


Figure 4: Images showing the diffracted output of a beam using the parallel tangents, equal curvature condition over a large angular bandwidth. Each picture shows the diffracted output as the read beam is deviated away from the optimum angle by 0.05° increments. The top, left-most picture shows the output at $\theta_r - 0.20^\circ$, with the progression shown down each of the 3 columns. The middle picture in the central column shows the optimum diffracted angular bandwidth, which occurs at θ_r .

θ_{eq} . Finally, the circle is translated by back by $-\Delta\vec{R}$, and the points where $\vec{k}_r - \Delta\vec{R}$ and $\vec{k}_{eq} - \Delta\vec{R}$ touch the ordinary k -circle determine the \vec{k} -vectors (and hence, the angles) of the two write beams, \vec{k}_{w1} and \vec{k}_{w2} , respectively.

Figure 3 shows the experimental setup of a system used to demonstrate the concept of the parallel tangents, equal curvature condition. Two highly polarized (≈ 40 dB isolation) ordinary beams are input into the crystal at angles θ_{w1} and θ_{w2} , with the θ_{w2} beam focused into the crystal with a lens with an effective numerical aperture (due to space constraints) of $NA = 0.5$ to test the Bragg matched angular aperture readout bandwidth. The third beam, which is extraordinarily polarized (≈ 45 dB isolation), is input into the crystal at an

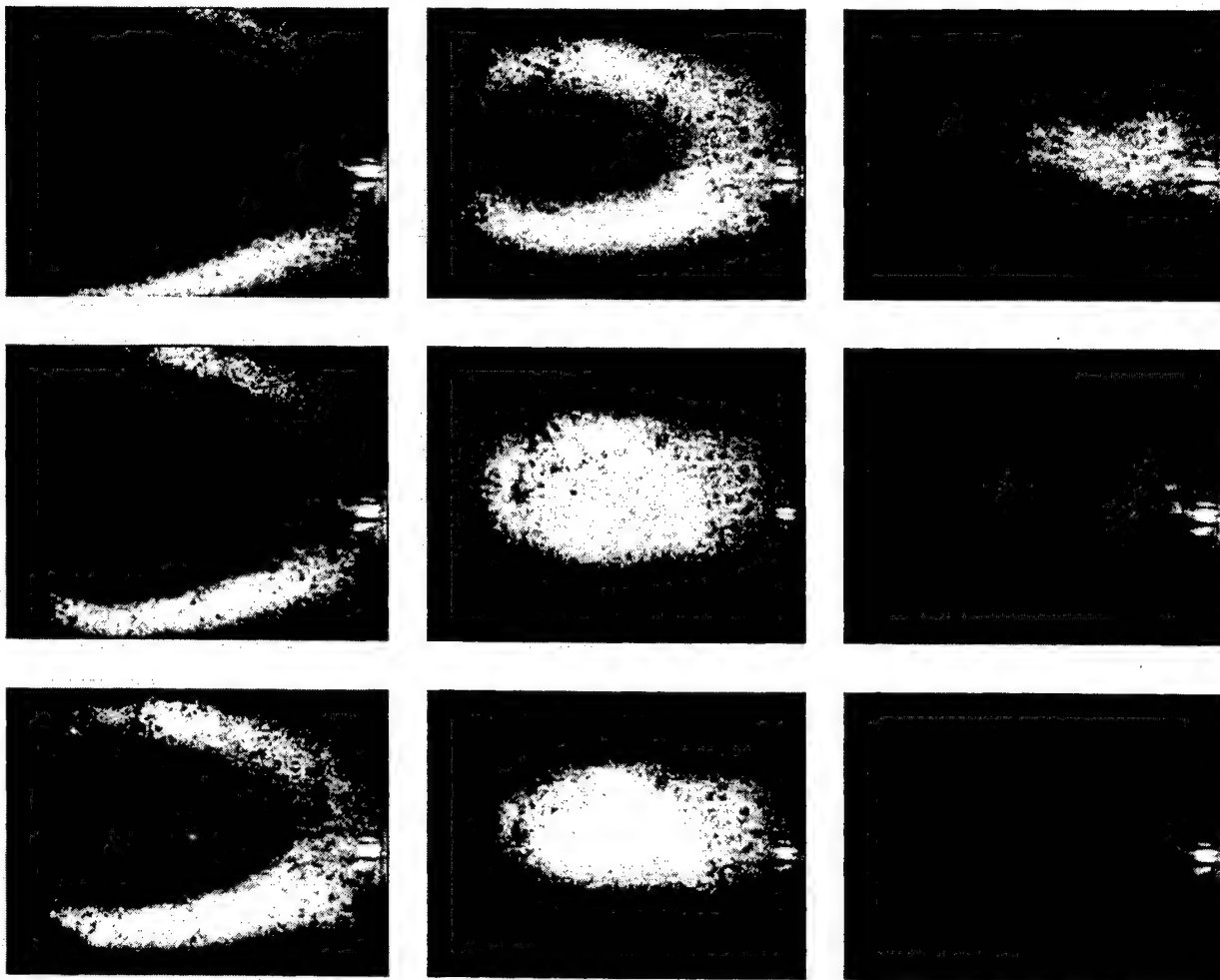


Figure 5: Images showing the diffracted output of a beam using the parallel tangents, equal curvature condition over a large angular bandwidth. Each picture shows the diffracted output as the write beam is deviated away from the optimum angle by 0.05° increments. The top, left-most picture shows the output at $\theta_{w1} - 0.20^\circ$, with the progression shown down each of the 3 columns. The middle picture in the central column shows the optimum diffracted angular bandwidth, which occurs at θ_{w1} .

angle θ_r . This read out beam diffracts off the grating within the photorefractive crystal, is passed through a horizontal polarizer to filter out the writing beams, and imaged onto a CCD camera. A 4f telescope was placed in the first writing beam and in the reading beam, between the final mirror in each arm and the crystal, so that each of the angles could be deviated away from their optimum values in order to characterize the system while still maintaining good beam overlap within the crystal.

Figure 4 shows images of light that diffracts off the hologram and is captured by the CCD camera when the read beam is rotated about the optimum readout angle θ_r by 0.05° increments. Similarly, Fig. 5 shows images of the output when the plane wave writing beam

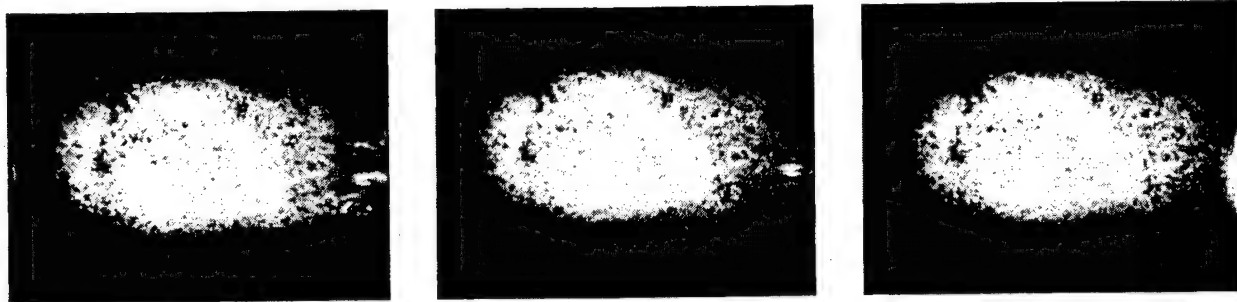


Figure 6: Images showing the optimum angular bandwidth as both the writing and reading beams are deviated about their optimum angles. Changes in the writing beam angle are compensated for by changing the read beam angle to ensure Bragg matching over the entire angular aperture. The left-most picture shows the output when the writing beam is deviated by -1.0° , the left-most picture by $+1.0^\circ$. The center picture shows the output when the writing and reading beam angles are at θ_{w1} and θ_r , respectively.

is deviated away from θ_{w1} , again by 0.05° increments. In both sets of pictures, the top, left-most picture shows the output at an angle $\theta_{opt} - 0.20^\circ$; the bottom, right-most picture shows the output at an angle $\theta_{opt} + 0.20^\circ$; and the incremental 0.05° changes can be seen in the progression of images along each of the three columns. Notice that the middle pictures in the central columns show the optimum diffracted angular bandwidth, spanning about 20.2° . This angular bandwidth is actually larger than the bandwidth in the Bragg degenerate direction, as can be seen in the figures. This is because the curvature of the k-sphere and the ellipsoid of revolution changes more quickly in the Bragg degenerate direction than in the plane of the parallel tangents, equal curvature condition.

Finally, Fig. 6 shows the diffracted readout when the writing beam is deviated by $\pm 1.0^\circ$, and the read beam is adjusted to compensate for the change in the Bragg angle to maximize the diffracted angular bandwidth. The left picture shows the output at -1.0° , the center picture at 0.0° , and the right picture at $+1.0^\circ$. Notice that the full bandwidth is still read out as the change in the write beam angle is compensated for by the change in the read beam angle. Data was taken out to $\pm 1.6^\circ$, with no change in the diffracted output bandwidth. Further results were limited by beam clipping which occurred within the two telescopic systems due to the small lens apertures required to image the beams into the crystal at their respective angles, which are separated only by about 4° .

3.2 Beam Forming with Polarization-Angle Read-Write Multiplexing

Once the polarization-angle, read-write multiplexing system was characterized using the parallel tangents, equal curvature condition, an experimental open-loop version of the optical

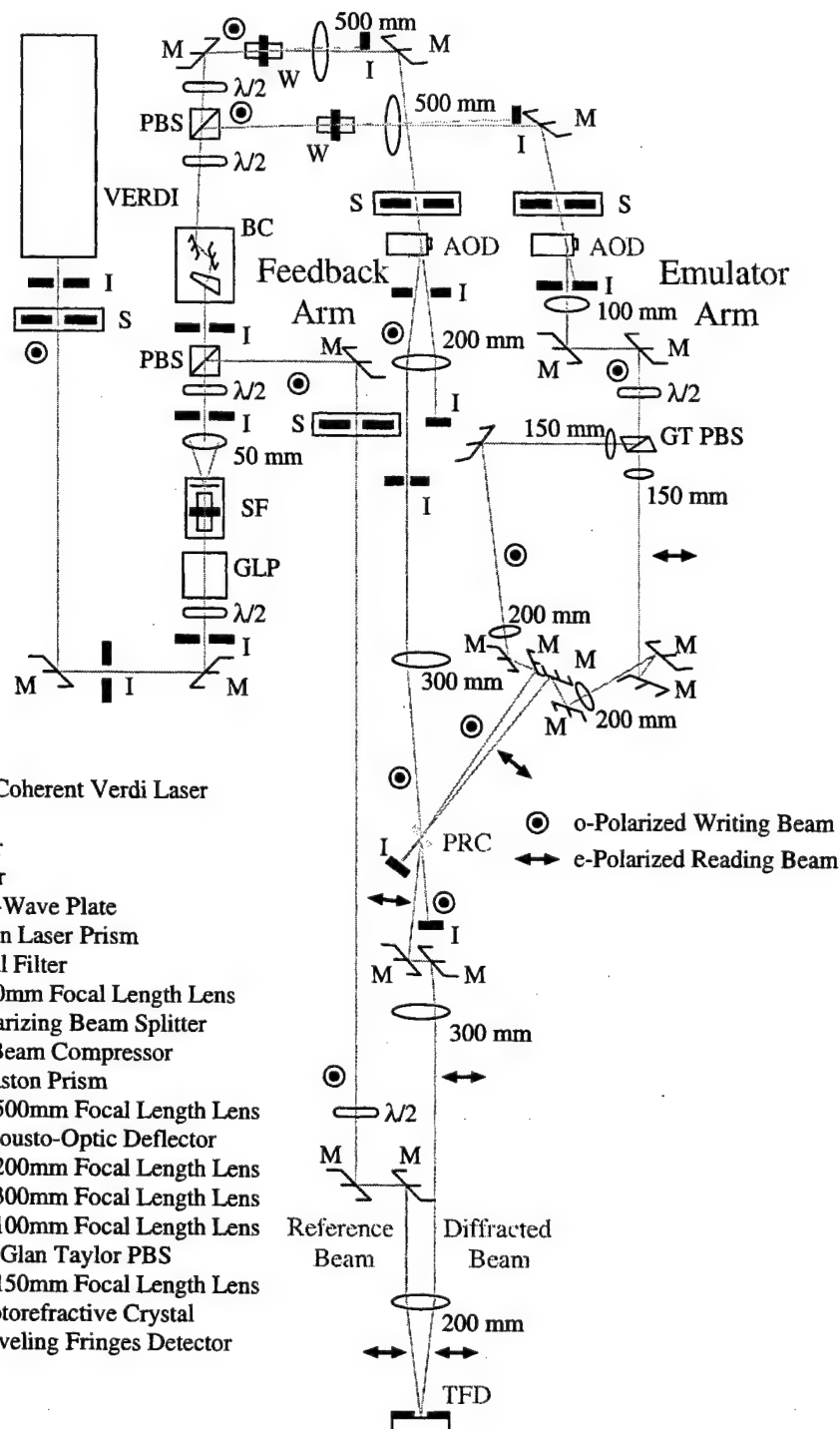


Figure 7: Detailed layout of the experimental polarization-angle read-write multiplexing architecture for isolation of the \hat{o} -polarized writing beams from the \hat{e} -polarized reading beam.

BEAMTAP processor was built. Figure 7 shows the experimental implementation of the system, including the polarization-angle, read-write multiplexing system used to isolate the

writing beams from the reading beam within the photorefractive crystal. The vertically polarized light from a Coherent 5 W Verdi laser is initially passed through a half-wave plate and Glan laser prism to act as a variable attenuator before being spatially filtered and collimated by a 50 mm focal length lens. The beam is then split into 2 beams via an additional wave plate and polarizing beam splitter. One beam serves as a clean reference beam for detection at the traveling fringes detector (TFD), and the other beam is passed through a 3:1 beam compressor so that, when split by an additional wave plate and polarizing beam splitter and Fourier transformed into the acousto-optic devices (AODs) using 500 mm focal length lenses, it produces two $225 \mu\text{m} \times 75 \mu\text{m}$ spots in the AODs (the transducers of the deflectors are $75 \mu\text{m}$ tall). Each AOD serves as the entrance into either the feedback arm, or the emulator arm of the processor. Light which enters the emulator arm diffracts off the acoustic gratings of the AOD, which emulates an array of signals from an antenna array. The first diffracted order is allowed to pass through an iris while the DC beam is blocked, with the diffracted light then being collimated and split into two orthogonally polarized beams by a Glan Thompson polarizing beam splitter—each with excess of 40 dB polarization isolation. The \hat{o} - and \hat{e} -polarized beams are then focused and imaged (using a single 2f lens system) into the photorefractive crystal (PRC) using 150 mm and 200 mm focal length lenses, respectively. Finally, as the two spots are imaged into the crystal, the \hat{o} - and \hat{e} -polarized beams are rotated to the write beam angle θ_{w2} and the parallel tangents, equal curvature angle θ_{eq} using two pairs of mirrors. The wide angular bandwidth writing angle and the parallel tangents, equal curvature angle is used for these two beams because the signals arriving from the antenna array may span a large angular bandwidth.

Back in the feedback arm of the processor, the lateral $225 \mu\text{m}$ spot size in the feedback AOD creates a tap-delay line with a total delay of 54 ns. Light which diffracts off this delay line is focused into the crystal, and since the beam is \hat{o} -polarized, it writes a cross-correlation hologram with the \hat{o} -polarized beam from the emulator arm of the processor. In addition, the angle by which this light is focused into the crystal is set to the first write beam angle θ_{w1} , so that the \hat{e} -polarized beam from the emulator is Bragg matched by the parallel tangents, equal curvature condition across the entire angular bandwidth of the emulated antenna array. The \hat{e} -polarized reading beam thus reads out the weight matrix formed by the cross-correlation between the emulated array of signals with the desired signal from the feedback arm of the processor. The \hat{e} -polarized light that scatters off this grating diffracts out of the crystal at the read beam angle θ_r . This is shown in Fig. 8. Figure 8a shows the overlap of the two ordinary polarized write beams and the extraordinary polarized parallel tangents, equal curvature beam in the photorefractive crystal. Figure 8b shows the only the parallel tangents, equal curvature beam, and the light is seen to be clearly diffracting off the hologram to the read beam angle θ_r .

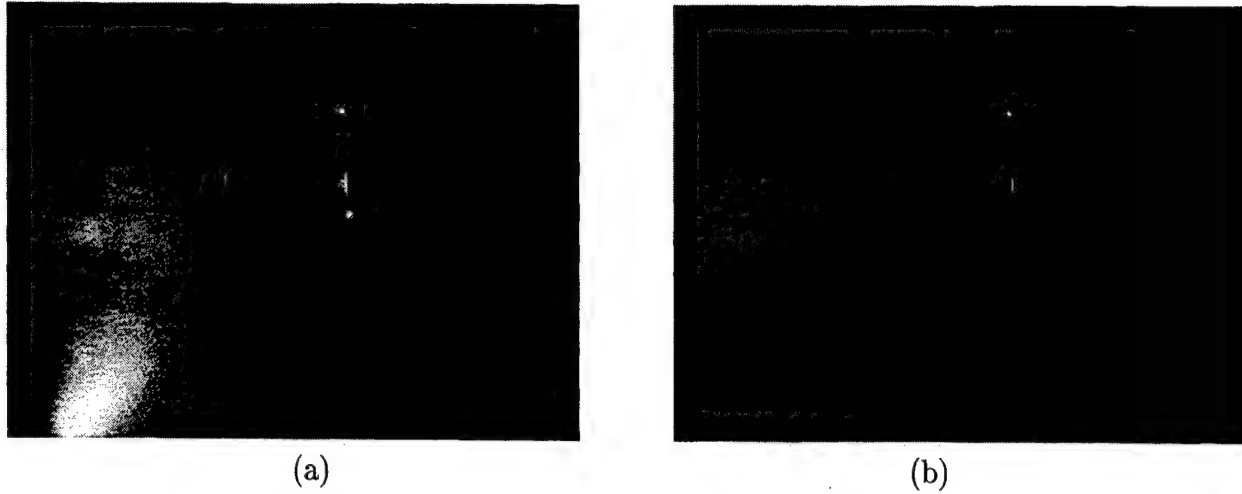


Figure 8: (a) The overlap of the two ordinary polarized write beams and the extraordinary polarized parallel tangents, equal curvature beam in the photorefractive crystal. (b) Only the parallel tangents, equal curvature beam, which is used to read out the hologram in the crystal, is shown here. Notice that the beam is clearly diffracted into the read beam angle θ_r .

With respect to Fig. 7, this diffracted beam is then adjusted to the writing beam angle θ_{w1} by a pair of mirrors so that the angle will be properly aligned for coherent, interferometric detection on the TFD with the clean reference beam. Likewise, the clean reference beam is adjusted to the feedback AOD DC reference beam angle by an additional set of mirrors and rotated by a half wave plate so that it is \hat{e} -polarized; and the feedback AOD DC reference beam, as well as the original write beam \vec{k}_{w1} are blocked by irises so that they will not be detected. The clean reference beam and the diffracted read beam are then focused onto the TFD, where they interfere to produce a set of moving fringes. Because the velocity of the photogenerated carriers are resonantly matched to the velocity of the interference pattern, the detected output contains the coherent addition of each of the emulated antenna array elements provided by the emulator arm of the BEAMTAP processor.

Figure 9a shows the detected beam-formed output for a single 1 GHz tone using the polarization-angle read-write multiplexing scheme. The detected power shown is the \hat{e} -polarized read beam, since the reading and writing beams were angularly separated from each other, and both writing beams were blocked by irises after the photorefractive crystal. When light from the reading beam was blocked in the emulator arm of the processor, the signal detected at the output of the TFD was minimized—this is because the writing beam was isolated by both polarization and angle from the reading beam. Figure 9b shows that the writing beam has been isolated from the reading beam by 45 dB. Furthermore, this isolation remains fixed with time due to the additional degree of orthogonality introduced into the system by angularly separating the two beams. Finally, note that the RF feedthrough in

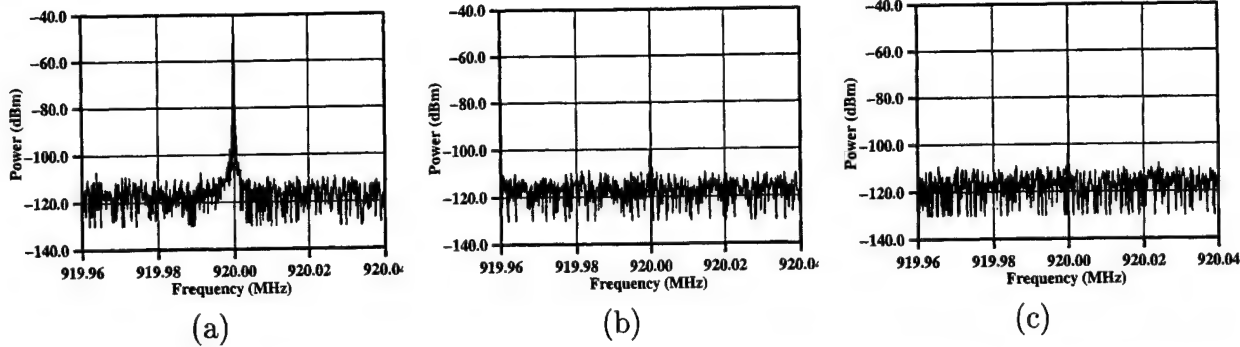


Figure 9: (a) Beam forming of a single 1 GHz tone using polarization-angle read-write multiplexing. The detected power is that of the \hat{e} -polarized read beam. (b) The detected power of the leakage of the writing beam when the reading beam is turned off. The isolation remains fixed with time, and is on the order of 45 dB. (c) The RF feedthrough in the system is of the same order of magnitude of the leakage of the writing beam. Note that the isolation of the writing beam is within 3 dB of the RF feedthrough.

the system, as shown in Fig. 9c, is within 3 dB of the leakage from the writing beam, demonstrating that a substantial amount of isolation has been achieved.

3.3 2-D True-Time-Delay Beam Steering

While investigating the BEAMTAP system, a beam-steering processor for user-defined direction pointing was developed. This processor can be used as a stand-alone device, or may be used to generate the desire signal for the BEAMTAP processor, thus allowing the user to point a beam in a given direction, while jammers outside of the main beam will be effectively nulled. Here, the stand-alone unit, consisting of mostly an antenna array, non-mechanical image rotator (for converting the 2-D into a 1-D beam steering problem) and 1-D true time-delay (TTD) processor is described.

3.3.1 2-D True-Time-Delay Beam Steering System

The front end processor which converts the 2-D antenna beamsteering problem to a 1-D TTD beamsteering problem is shown in Fig. 10. For a densely sampled 2-D planar array, far field signals can arrive at elevation angles ranging from say -80° to $+80^\circ$ and at arbitrary azimuth angles. Therefore, the array elements must be appropriately time delayed and summed to produce a squint-free, beam-steered output (*i.e.* the angular receptivity pattern should be independent of frequency and point in the direction of interest). Since all of the time delays along lines perpendicular to the beam-steered direction are equivalent, the antenna signals from all the array elements with identical delays can be summed first, and

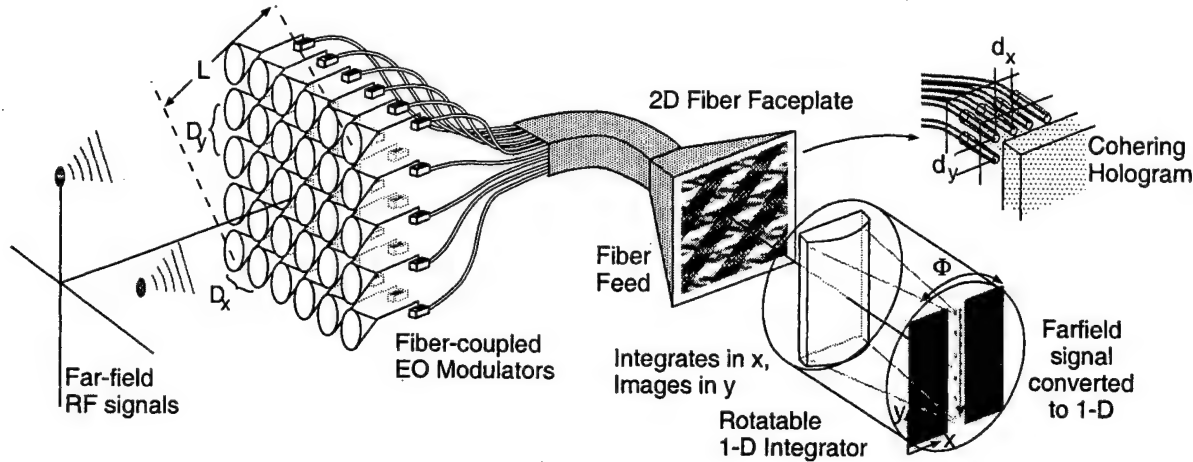


Figure 10: 2-D RF antenna array modulating an array of fibers using electrooptic (EO) modulators which are coherently fed (preserving the array topology and carrier phase) to a fiber face plate. This launches the optical signals into a rotatable 1-D optical integrator, which collects all the signals from a given azimuth onto an slit. This effectively changes the 2-D array processing problem to a 1-D array problem. The slit can be processed with a 1-D array processor, as shown in Fig. 11.

then processed in the same way the signals from a 1-D array would be. For an equi-spaced 2-D array, the signal $s(t)$ arriving from a broadband, far-field source with direction cosines $(\alpha, \beta) = (\cos \theta_x, \cos \theta_y)$ and corresponding azimuth and elevation angles $\phi = \tan^{-1} \frac{\beta}{\alpha}$ and $\theta = \cos^{-1} \sqrt{\alpha^2 + \beta^2}$ will produce an output from the mn th antenna element that will be proportional to $r_{mn}(t) = s(t - [nD_x\alpha + mD_y\beta]/c)$ where the antenna spacing is D_x and D_y . Hence, lines where the term $nD_x\alpha + mD_y\beta$ is constant are lines of equal time delay. This suggests a processing strategy of first rotating the array of signals by the azimuth angle $-\phi$ and then summing along x .² The resulting 1-D array of signals can then be processed using a 1-D true-time-delay summing network.

Our approach to accomplish this 2-D receive mode beam steering operation is to modulate the broadband RF signals received by each antenna element onto an array of optical fibers using electro-optic (EO) modulators, and then utilize a topology preserving fiber feed (with spacing d_x and d_y) to launch the modulated signals into a rotatable system that integrates the signals in x' and images them in y' , as shown in Fig. 10. This can be represented as

$$\begin{aligned} s_r(y, t) &= \int \mathcal{R}_{-\phi} \left\{ \sum_{m,n} r_{nm}(t) \delta(x - nd_x, y - md_y) \right\} dx \\ &\approx s \left(t - y \frac{\sin \theta}{c} \frac{d}{D} \right) \mathcal{P}_{-\phi}\{A_{XY}(y)\}, \end{aligned} \quad (2)$$

where $\mathcal{R}_{-\phi}$ is the 2-D rotation operation and $\mathcal{P}_{-\phi}A_{XY}$ is the projection operator orthogonal to ϕ of the antenna aperture A_{XY} as a function of y , which for a circular aperture is just a half circle function for all ϕ . Even though the approach shown in Fig. 10 is a very direct way

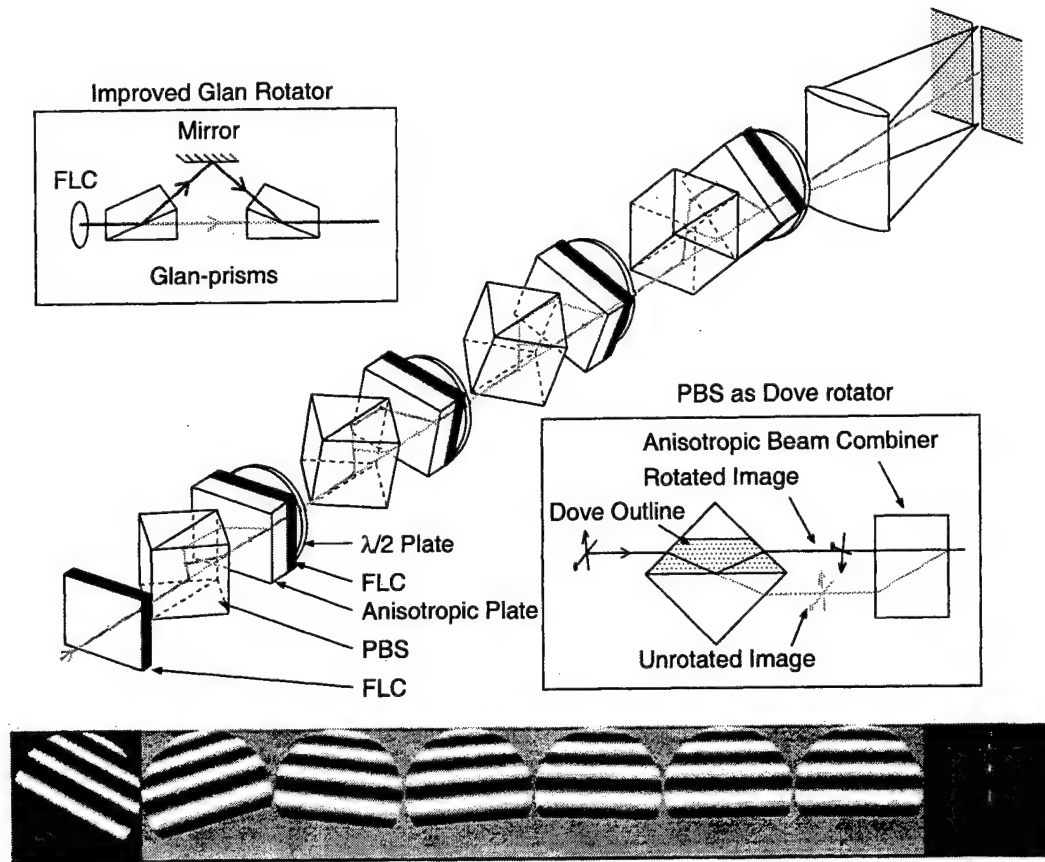


Figure 11: Multi-stage image rotation system based on binary sequence of rotated polarizing beamsplitters (PBS), Ferroelectric Liquid Crystal (FLC) polarization switches, and anisotropic beam combiners. The simulated operation of such a rotator sequence showing the output image of each stage of the rotators illustrated. For the example azimuth angle of 28.5° , rotators 2, 4, 6 are on using the FLC switches, and the others remain off. The 1-D summed output at the back focal plane of the cylindrical lens is shown on the right after the final stage rotates the desired signal to align with the integration axis.

of achieving the desired operations (integration in x' and imaging in y' onto a narrow slit), the mechanical nature of the rotation prohibits fast switching to arbitrary angles of arrival, and runs the risk of the failure of the mechanical parts. This makes an electro-optic method of image rotation desirable.

3.3.2 Electrooptic Image Rotation

Our novel electro-optic image rotator, shown in Fig. 11, consists of fixed polarization switchable rotators in a binary sequence of rotation angles (eg. 90, 45, 22.5, 11.25, 5.625). The similarity between the cross section of a Dove prism and a polarizing beamsplitter (PBS) provides the inspiration for such a design, since when a PBS is rotated around its split face

to an angle γ , the polarization which reflects off the split face will be rotated by 2γ , while the orthogonal polarization which transmits will not be rotated. Thus, by controlling the polarization through a series of rotated PBS's using single-pixel Ferroelectric Liquid Crystal (FLC) waveplates, we can select the rotation angle very rapidly (10-100 μ sec is typical). The beams from the different ports must be recombined, which can be accomplished using anisotropic walkoff in an off-axis crystal slab, as illustrated in the multistage system in Fig. 11. Note that these PBS operate at an unusual incidence angle, and would require special coatings for acceptable polarization isolation. Although the system can tolerate some PBS leakage, a multistage dilated array of Glan prism-polarizer deflectors will have orders of magnitude better polarization isolation, and eliminate the need for special PBS or anisotropic walkoff plates. Once the image has been rotated, a cylindrical lens takes the 1-D Fourier transform of the image, and projects it onto a slit. The slit acts as a spatial filter which removes those signals which still have a periodic structure in the x' dimension, and effectively passes all signals from the same azimuth ϕ . These signals move at a phase velocity $v = \frac{c}{\sin \theta} \frac{d}{D}$, which is scaled from the velocity at the antenna by the ratio of the fiber spacing (typically $d_y = 250 \mu\text{m}$) to the array element spacing ($D_y \approx 1 \text{ cm}$ for a 15 GHz array). Thus, an end-fire signal produces a signal velocity of $v_{\text{ef}} = \pm c \frac{d_x}{D_x}$, while a bore-sight signal produces an infinite phase velocity (*i.e.* no time delays of the signals across the aperture).

3.3.3 1-D True-Time-Delay Processing

For the selected azimuthal slice, parallel multi-beam formation can be accomplished by imaging the output of the azimuth integrated slit onto an array of traveling fringes detectors (TFDs) with individually-tuned carrier velocities covering the range of velocities necessary to compensate the signal velocities from all elevations (propagating in both directions), as shown in Fig. 3.3.3. The TFD operates as a scrolling integrator, like a time-delay-and-integrate charge coupled device (TDI CCD), except at multiple GHz.^{3–5} In this device, optical inputs produce photoelectrons which drift across the device aperture and are added to by subsequent inputs. Inputs on one side of the device accumulate delays as large as 10 ns, while inputs on the other side experience almost no delay. Optical signals produced from a specific desired RF elevation propagate synchronously with the drift velocity of the TFD and are coherently accumulated to produce a large, wide-band, squint-free response, whereas other elevations which produce different velocities of the image transmitted by the slit wash out and produce no response. Since such TFD systems can only cover a small range of velocities (say a factor of 2) and do not range over positive, zero, and negative inverse-velocities, we include a fiber prism with a total delay difference of $3L/c = 3\sqrt{2ND}/c$, which

transforms the azimuth integrated signals passing through the slit to

$$\begin{aligned} s_d(x, t) &= s_r \left(x, t - \frac{x}{d\sqrt{2N}} \frac{3L}{c} \right) \\ &= \left(t - \frac{x}{c} [\sin \theta + 3] \frac{D}{d} \right) \mathcal{P}_{-\phi} A_{XY}(x). \end{aligned} \quad (3)$$

This gives the signals only a variation of a factor of 2 of delay (and velocity) across the aperture, and removes the difficulties at bore sight associated with zero delay (infinite phase velocity) operation of a TFD.

Wavelength tuned fiber delay lines are another attractive approach to implementing the required time delays. A dispersive-fiber prism in which each fiber has a constant length, but with the fibers split between a normal fiber and a highly dispersive fiber with a junction linearly proportional to fiber number allows the delay ramp to be controlled by the wavelength of the incident light,⁶ as illustrated in Fig 3.3.3. In fact, several wavelengths can be used at once, and each will simultaneously be time delayed by the appropriate delay ramp to steer a beam to a different elevation, and the appropriately delayed signals can be summed and separated by a lens and grating. Therefore, by illuminating the antenna array modulators by a comb of wavelengths, rotating the multi-wavelength image to a desired azimuth, 1-D integration using a cylindrical lens through a slit, coupling into the dispersive fiber prism, integrating the output with a lens, and separating the optical spectral components with a grating onto an array of detectors, all elevation beams at the selected azimuth are formed.⁷

Full N^2 multibeam steering can be accomplished by combining wavelength multiplexing and TFD velocity tuned arrays. Passive wavelength control of the cascaded image rotator can be used instead of active polarization control, by using beam splitters with specially designed wavelength selective thin film coatings with a binary reflectivity spectrum (eg 00001111, 00110011, 01010101 for 8 wavelengths in a 3 BS image rotator system). A single tunable laser can be used to rapidly (sub microsecond tuning has been demonstrated) select the path through the rotated BS sequence and choose an azimuth rotation angle, and the array of velocity tuned TFDs will produce the desired array of TTD all-elevation beams. Alternatively, a comb of wavelengths illuminating the array of EO modulators will be rotated to all azimuth angles in parallel by the wavelength selective BS cascade, and passing through the integrator slit, and separated by wavelength onto a 1-D array of TFDs biased by a common control voltage will produce all azimuth beams in parallel at a selectable elevation (determined by the carrier velocity in the TFDs determined by the bias voltage). Combining these approaches, using a multi-wavelength laser to illuminate the array of EO modulators, coupling the fiber array output through the wavelength selective BS image rotators, integrating through the slit, and separating the wavelengths with a grating onto a 2-D array of velocity tuned TFD detectors allows all elevation and azimuth beams to be formed in parallel. This

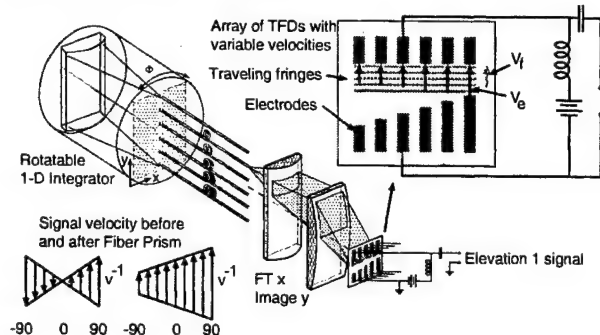


Figure 12: TTD processor that uses a fiber prism to impose a delay across the 1-D signal to allow processing with unidirectional TFD array. Increasing angles of arrival velocity-matched with different TFDs.

allows all of these signals to be accumulated continuously to increase the detection sensitivity of a surveillance array to its ultimate limit, without the decreased integration time required by scanning systems.

3.4 Progress Summary

Table 4 provides a description of the completed progress during year three. Silicon detectors using semiconductor CMOS technology were developed and fabricated, but because there is a large parameter space to explore, and high frequency RF devices using semiconductor technology are difficult to fabricate, they are still being investigated. New GaAs devices optimized for hole transport and collection have also been designed, but not fabricated. Therefore, since we have tried to optimize the true-time-delay capabilities vs. efficiency, we will continue to research this topic during Year 5.

Because the mult-signal emulator is no longer being used within the current BEAMTAP system, compensating for the lateral shift between the read/write beams is no longer necessary. However, it is still possible to probe the system angular response by rotating the crystal while probing the hologram with a weak read beam. This will be done currently. In addition, we have fully optimized the read-write multiplexing scheme over the full bandwidth by employing a new polarization-angle read-write multiplexing scheme using the parallel tangents, equal curvature condition using a 45° cut piece of BaTiO₃. Now that the system response has been optimized over the full bandwidth, the feedback loop will now be closed in order to provide the jammer nulling capabilities of the BEAMTAP processor.

Unfortunately, investigation of the all-optical BEAMTAP system has again been hampered this year by a slow commercial response time to the orders we have placed for the 1.06 μm AODs and EOMs. The EOMs have been characterized, but we have not yet re-

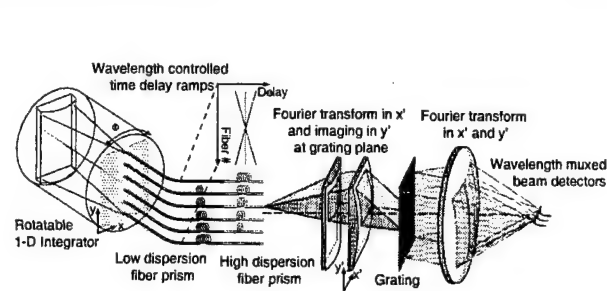


Figure 13: TTD processor that uses a fiber prism to impose a delay across the 1-D signal to allow processing with unidirectional TFD array. Increasing angles of arrival velocity-matched with different TFDs.

ceived the AODs. Since the operation of the all-optical BEAMTAP system hinges upon the performance characteristics of these devices, progress in this particular area has been slow.

However, significant progress has continued in additional areas which were not originally proposed in our original fourth year plans, including additional work on the polarization-angle read-write multiplexing system by correcting the theory for the parallel tangents equal curvature condition, fully characterizing the experimental multiplexing system, folding the system into BEAMTAP, imaging the diffraction off the holographic grating in the crystal, and performing narrowband beam forming. In addition, a true-time-delay beam steering architecture has been developed, simulations performed, and initial experimental work completed in order to demonstrate the feasibility of the electro-optic image rotation system. Furthermore, the P-Vector BEAMTAP algorithm has been derived, the optical architecture has been developed, and the dependency of the feedback gains has been analyzed.

3.5 Plans for Year 5

Table 5 outline the plans for year five. Specifics include, in order to demonstrate the full BEAMTAP system, characterizing the polarization-angle read-write multiplexing system over the full bandwidth, closing the feedback loop for adaptive jammer nulling. We will also analyze the closed-loop performance of BEAMTAP, and characterize the adaptive null depth, jammer nulling dynamics, signal-to-noise ratio, and spur-free-dynamic range. In addition to this, we will also continue to work on additional algorithms and development of BEAMTAP. The P-Vector BEAMTAP system will continue to be explored, and the phase-cohering system will be tested. Finally, we will perform a final system evalution to optimize the current BEAMTAP system.

Table 4: Year 4 Progress

Year 4 Plans	Completed	In Progress
Further Explore TFD Technology		
Optimize time-delay capabilities vs. efficiency	×	×
Fabricate and test silicon based devices		×
Multi-Signal Emulator		
Compensate for lateral shift between read/write beams	—	—
Probe system angular response		×
Demonstrate BEAMTAP System		
Optimize read/write multiplexing over full bandwidth	×	×
Close feedback loop for jammer nulling		—
Investigate All-Optical BEAMTAP System		
Demonstrate fiber TDLs and coherent fan-in	—	—
Explore 1.06 μm star couplers vs. side tapped arrays	—	—
Characterize 1.06 μm AODs	—	—
<hr/>		
Additional Year 4 Progress	Completed	In Progress
Polarization-Angle Read-Write Multiplexing		
Parallel tangents equal curvature theory corrected	×	
Read-write multiplexing system fully characterized	×	
Read-write multiplexing incorporated into BEAMTAP	×	
Imaging of holographic diffraction performed	×	
Narrowband beam forming performed with multiplexing	×	
2-D True-Time-Delay Beam Steering System		
Front-end beam-forming system developed	×	
Electro-optic image rotation system simulated	×	
First image rotation stage tested	×	
1-D True-time-delay processing system simulated	×	
P-Vector BEAMTAP		
P-Vector BEAMTAP algorithm derived	×	
System architecture formulated	×	
Feedback gains analyzed	×	
Traveling Fringes Detector		
Hole-resonant contact device designed	×	

Table 5: Plans for Year 5

Year 5 Plans	
Demonstrate BEAMTAP System	Characterize read/write multiplexing over full bandwidth Close feedback loop for jammer nulling
Analyze Closed-Loop Performance	Analyze adaptive null depth Characterize jammer nuling dynamics Measure signal-to-noise ratio Test spur-free dyanmic range
Algorithms and BEMTAP Development	Continue to explore P-Vector BEAMTAP Test phase-cohering system Evaluate final system design

4 Optical Coherent Transient True-Time Delay

Principal Investigator: Wm. Randall Babbitt, Montana State University, Physics

The main goal of this part of the MURI effort is to explore the use of optical coherent transient (OCT) technologies in true-time-delay (TTD) processing systems. As stated in last year's report, our plans for years 4 and 5 are to 1) Demonstrate OCT TTD in the 10 GHz range, 2) Carry out phase and delay resolution measurements up to 10 GHz, 3) Measure bandwidth, delay range, and output fidelity up to 10 GHz, 4) Steer a two-element antenna with OCT TTD, 5) develop injection locking for amplification of high bandwidth signals, 6) Build and use a 4-bit multi-path delay line for high bandwidth measurements, and 7) design and analyze various OCT TTD based system and evaluate their performance. The progress in these areas is detail in the following sections. We have decided to limit our demonstration to up to 3GHz due to current limitations on the production and detection of signals greater than 3 GHz, not due to any limitations of the OCT materials. To achieve multi-GHz signals for input to the OCT TTD device, we have used the 4-bit multi-path delay line, but also developed injection locking techniques that work up to 3 GHz. We used the 4-bit delay to make delay range and jitter measurements on 3 GHz bandwidth (detection limited) signals and to observe signal fidelity. Delay range and bandwidth have been improved by the introduction of a new technique: temporally overlapped frequency chirped pulse programming. This technique and demonstrations are detailed below. An alternative to using chirped laser sources is also explored: linear phase chirps. The transmit and receive antennas for the two-element steering demonstration have been fabricated and are in the process of being tested. In year 5, we will continue along our current path to demonstrate OCT TTD up to 3GHz bandwidth and to evaluate the system performance of OCT TTD based systems.

4.1 Demonstration of Optical Coherent Transient True-Time Delay at 4 Gbit/s

We have improved on our demonstration of the broadband TTD capabilities of OCT materials and have faithful TTD at bandwidths of more than 3 GHz (detection limited). Figure 14 shows the schematics of the setup used in the demonstration. A Ti: Sapphire laser with a regenerative amplifier and an external etalon provided the 30 ps Fourier-transform limited pulses at a 1 kHz repetition rate to accumulate and maintain a TTD grating in the Tm:YAG crystal. An adjustable delay line set the separation between the programming pulses on beams 1 and 2 to nominally 9.7 ns and thus, the programmed TTD. The probe signal was a 6-bit binary sequence (101101) made of a train of 30 ps laser pulses at the

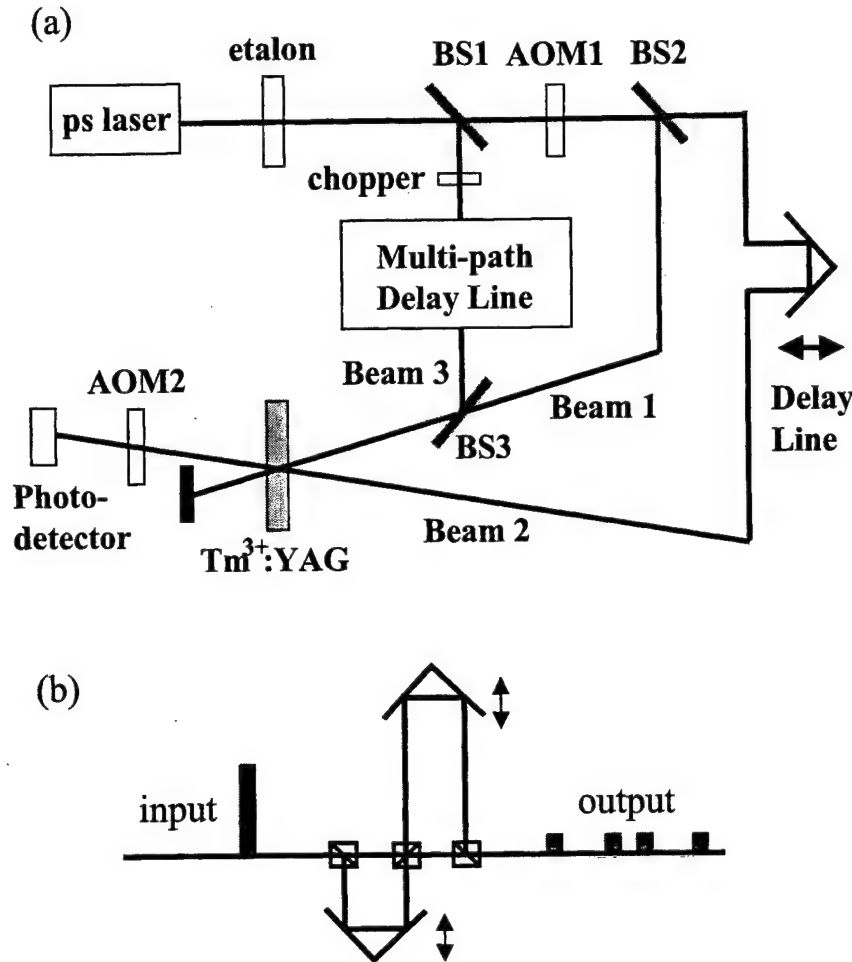


Figure 14: (a) Experimental setup schematics. BS: Beam splitter, AOM: Acousto-optical modulator. (b) Multi-path delay line for input data sequence generation.

data rate of 4 Gbit/s to mimic an optical carrier and rf signals. It was created by a multi-path delay line (Fig. 14b) on beam 3 and is shown in the upper trace of Figure 15. The delayed coherent transient response signal generated in the crystal was recorded with a 3 GHz oscilloscope, which set the limit on our demonstration bandwidth. The delayed output signal (echo) is shown in the lower trace of Figure 15 and also in Figure 16 for various settings of the delay. The output shows good fidelity up to the 3 GHz bandwidth limit of our oscilloscope. The delayed output is expected to have a bandwidth of 17 GHz at the same bit rate as the input. The multi-path delay line could thus have generated a data sequence at bit rates up to 10 Gbit/s, had we not been limited by our oscilloscope bandwidth.

To demonstrate the accuracy and resolution of the delay, the timing of the programming pulse pair was tuned by varying the free-space path difference with the micrometer in the delay line. The length was varied over 54 mm in one direction from the nominal position.

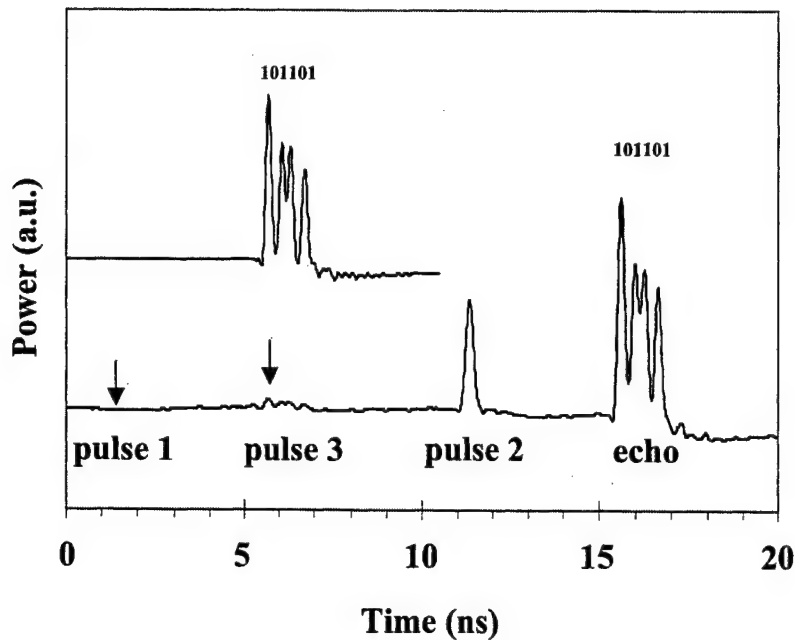


Figure 15: Upper trace: Input data sequence representing 101101 at 4 Gbit/s. Lower trace: output of delayed data sequence (echo) from the crystal, including scattered light from beam 1, input data (pulse 3) and the leakage of beam 2 from AOM 1. All curves were averaged over 50 shots measured with 12 GHz photodetector and recorded with 3 GHz oscilloscope.

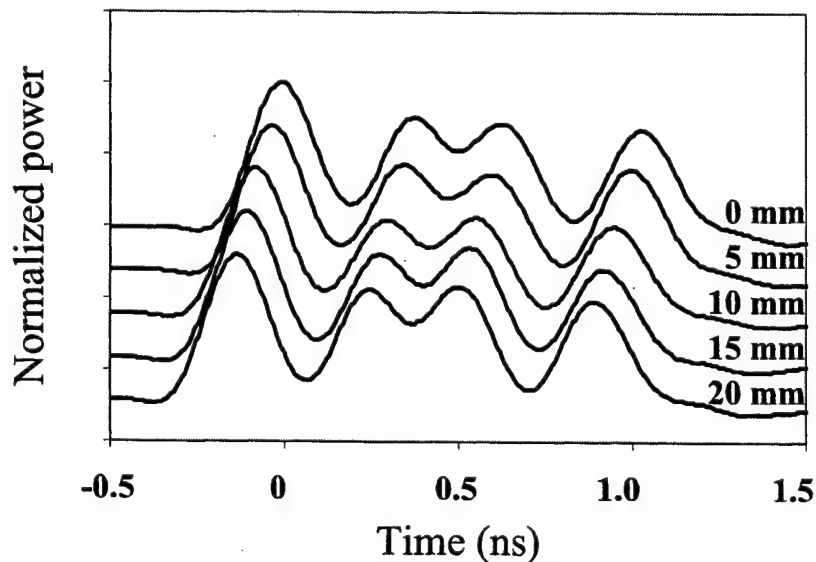


Figure 16: Delayed data sequence averaged over 50 signal shots and normalized at various lengths of delay line with respect to the nominal position at 2.91 meters (9.7ns).

The delay accuracy at each point was measured using the average of 50 single shot captures of the output signal. Figure 16 shows the output at various delays with respect to the

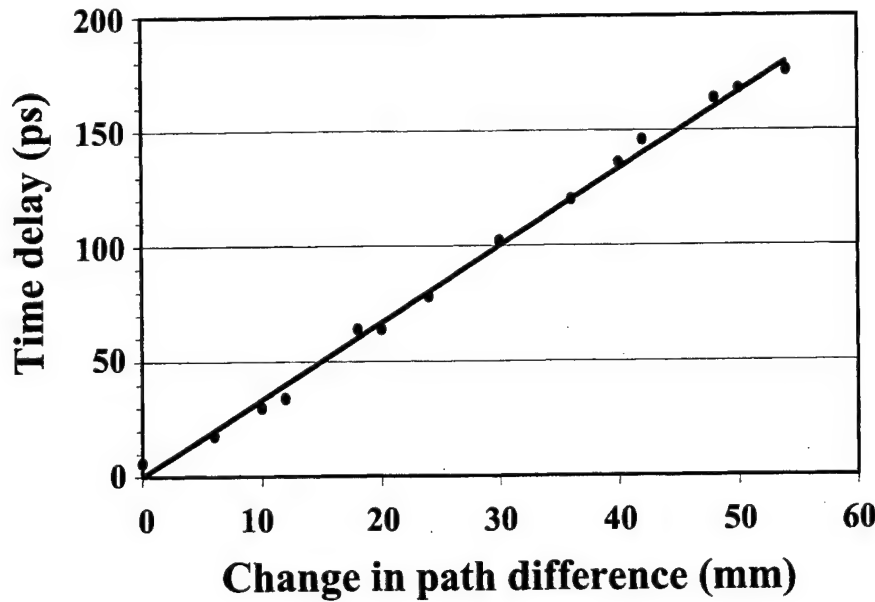


Figure 17: Measured delays (dots) and expected delays (solid line) versus introduced path differences.

nominal case with the first bit centered at 0 ns. Figure 17 gives the measured delays (dots) versus introduced path differences. The fine tuned delays were measured with a computer program calculating the time shifts of the signal traces at various positions with respect to the trace at nominal position using the least rms fit. The predicted delay is plotted as the solid line. The standard deviation of difference between the measured and calculated delays is 1 picosecond. To determine the delay jitter on a single-shot output, the delays of 50 single-shot outputs were measured at one position (30 mm). A delay jitter of 7ps rms was obtained. The timing jitter of the input sequence was also measured with 50 signal shots to be 7 ps rms. Thus, the delay jitter measurement of 7ps is measurement limited. The measurement accuracy of 1 ps delay resolution (determined by the average of 50 shots) is thus also limited by the timing jitter.

This demonstration shows one can perform TTD on multi-gigahertz bandwidth signals using OCT techniques. The delayed output retains good signal fidelity with excellent delay accuracy and resolution. The bandwidth was measurement limited to 3 GHz, while the expected performance exceeds 10 GHz.

4.2 Amplification of High Bandwidth Phase Modulation Using Injection Locking

Achieving efficient programming at high bandwidths and creating high bandwidth data probes require high bandwidth amplification techniques. We have experimentally demon-

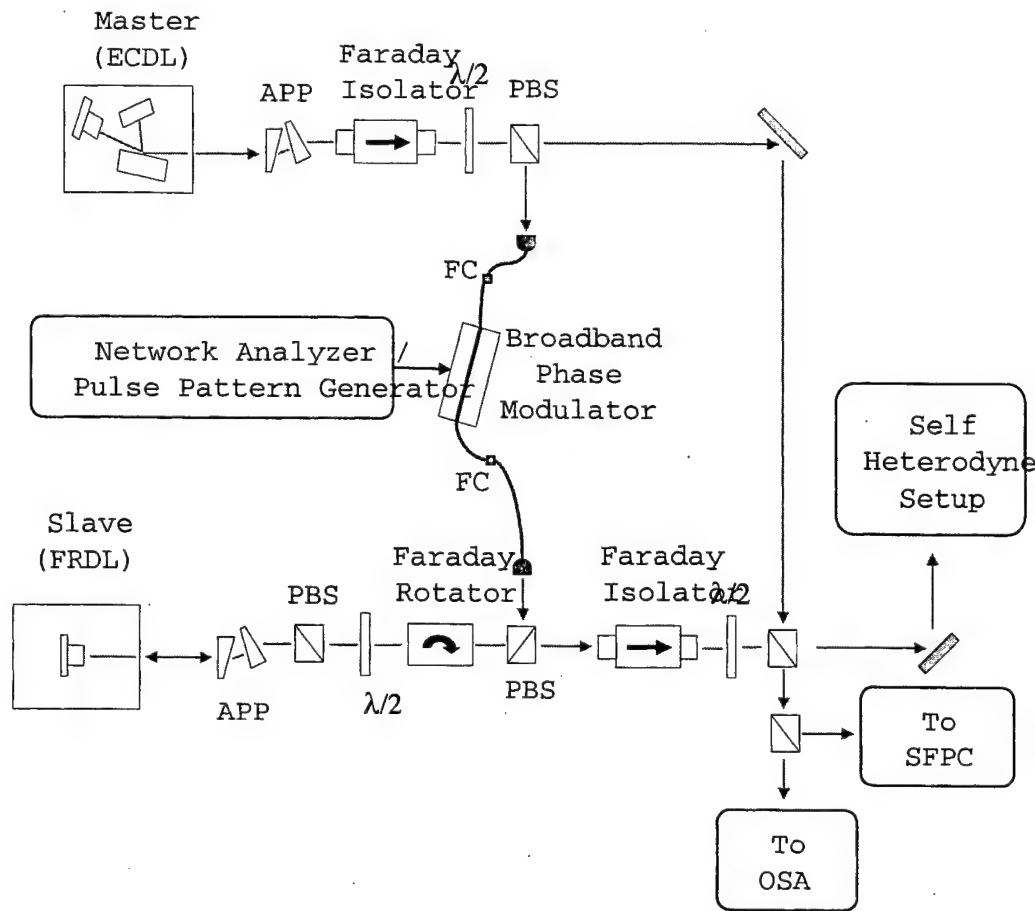


Figure 18: Optical injection locking setup using a fiber coupled integrated optics phase modulator. See text for discussion.

strated amplification of high bandwidth phase modulated outputs from integrated optics modulators at 793 nm by using an injection locking technique. Current off the shelf integrated optic modulators, driven at high frequencies (1 – 10GHz), are power limited at 793 nm (the $^3\text{H}_6 - ^3\text{H}_4$ transition in Tm^{3+} , a likely candidate for an OCT TTD device) due to possible photorefractive damage of the LiNbO_3 waveguides. Typical optical input powers for these devices at this wavelength are between 2-10 mW with optical output powers ranging from 100-800 μw . This power level is inadequate for practical operation of the desired applications of spatial-spectral holography.

In order to amplify optical signals from the modulators we used an injection-locking scheme with an anti-reflection (AR) coated semiconductor diode laser operating at 793 nm as the slave. The set-up is simple and is ideally suited to compact packaging. Similar studies have been conducted with signals up to 2 GHz at 1.3 μm .⁸ Figure 18 shows the injection

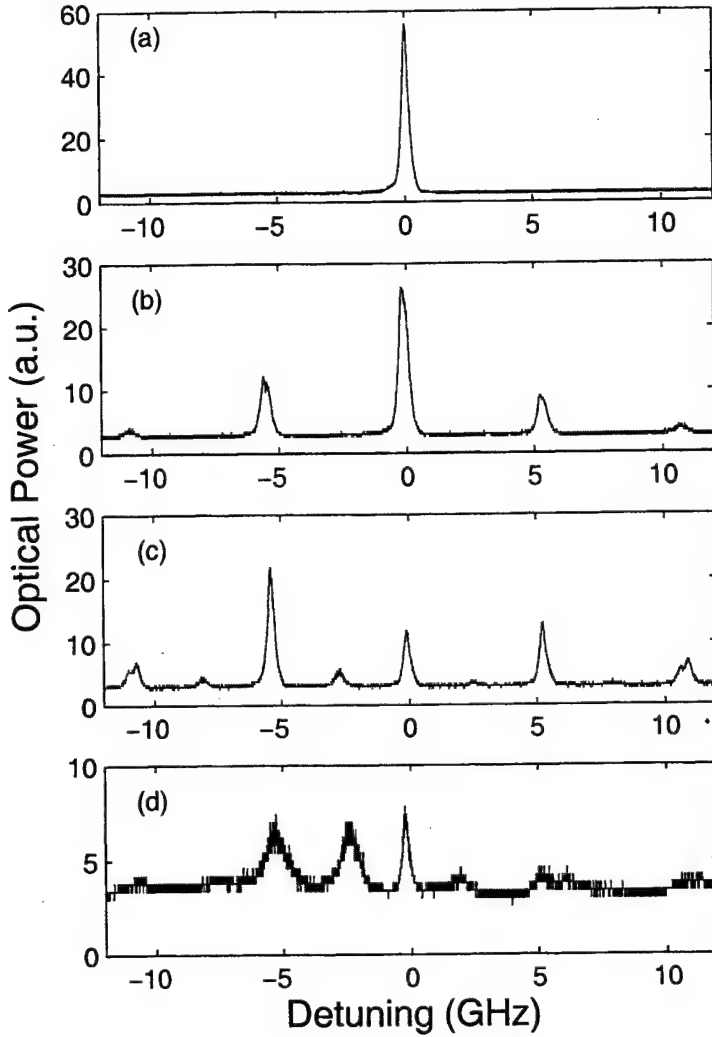


Figure 19: Optical spectrum of the different regions on the period doubling route to chaos showing (a) Stable locking, (b) undamped relaxation oscillations, (c) period doubled relaxation oscillations , and (d) the chaotic region.

locking setup typically used for these high bandwidth studies. In our experiment, the master laser is a homemade external cavity diode laser operating in the Littman configuration. After traveling through an optical isolator, the master is coupled into a single mode polarization maintaining fiber. The fiber is connected to an integrated optic phase modulator. The output from the modulator is then sent into the output port of another isolator and injected into the slave laser. Because of the AR coating on the slave diode, locking of the slave laser to the master laser is relatively easy needing very low powers ($\sim 50 \mu\text{W}$) and giving large locking bandwidths. The locked output retains the master laser's properties with over 40 dB of sidemode suppression.

The standard period doubling route to chaos was observed by locking the slave laser

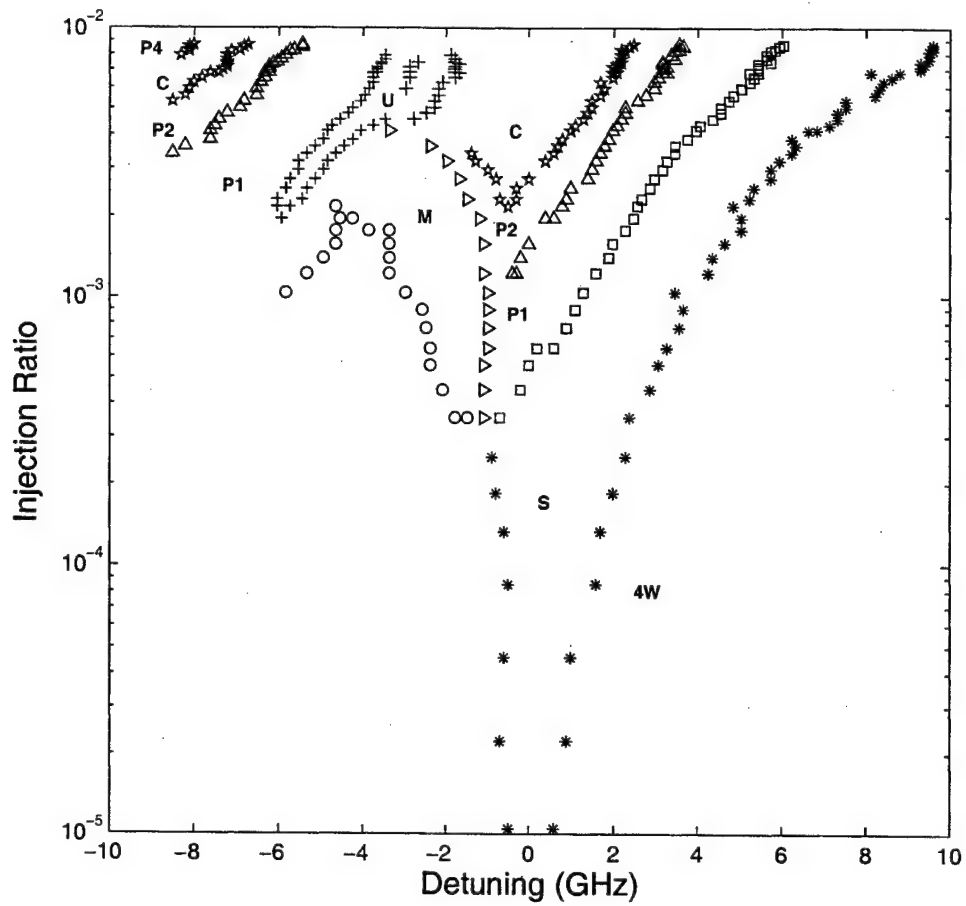


Figure 20: Observed regions of injection locking versus the detuning and the injection ratio. The symbols represent boundaries between different regions. The various regions are stable locking (S), undamped relaxation oscillations (P1), period doubled relaxation oscillations (P2), chaotic regions (C), four wave mixing (4W), multi-longitudinal mixing (M), period four relaxation oscillations (P4), and an interference region of chaos and relaxation oscillations (U).

with low injected powers and then increasing the injected power.⁹ To our knowledge this has not been observed before using an AR coated diode as a slave laser. There are four main regions as the injected power is increased and these are shown in Figure 19 for a slave output of $P_{out} = 88$ mW. The four regions shown in Figure 19 are (a) stable locking with $P_{in} = 9 \mu\text{W}$, (b) undamped relaxation oscillations shown with $P_{in} = 70 \mu\text{W}$, (c) period doubled relaxation oscillations shown with $P_{in} = 132 \mu\text{W}$, and (d) finally the chaotic region shown with $P_{in} = 352 \mu\text{W}$. The relaxation oscillations of the slave laser, measured using a heterodyne technique¹⁰, were $\nu_{RO} = 5.6$ GHz at $P_{out} = 88$ mW, in good agreement with $\nu_{RO} = 5.5$ GHz obtained from Figure 19(b).

Figure 20 is a map of the different injection locking regions and shows good agreement

with features found using non-AR coated diodes and DFB lasers.^{11,12} This map was produced by increasing the injected power level from $P_{in} = 0.8 \mu\text{W}$ to $P_{in} = 792 \mu\text{W}$ and stepping the master frequency, ν_M , from -10 GHz to +10 GHz with respect to the slave laser's nearest facet mode frequency, ν_S . The detuning parameter has been defined as $\Delta\nu = \nu_S - \nu_M$. The injection ratio is defined as the input power directly in front of the slave laser cavity divided by the output power from the slave without inclusion of cavity coupling factors. The defined regions on the map are stable locking (S), undamped relaxation oscillations (P1), period doubled relaxation oscillations (P2), chaotic regions (C), four wave mixing (4W), multi-longitudinal mixing (M), period four relaxation oscillations (P4), and an interference region of chaos and relaxation oscillations (U). The different markers on the map delineate the approximate boundaries between regions.

We wanted to use the injection locking to amplify phase-modulated signals from an integrated optics phase modulator. We found good reproduction of cw phase modulated signals out to 3.5 GHz with amplifications of approximately 23dB. These results were promising and led us to attempt doing some broadband operation. To explore the slave laser's ability to faithfully reproduce a digital signal, we used a pulse pattern generator to produce a set of test binary data sequences. The output of this pulse pattern generator went to a high bandwidth amplifier that produced digital signals of approximately 7 V_{pp}. This amplified signal was then used to drive the phase modulator to V_π and encode data sequences onto the optical carrier as π phase shifts (BPSK). Three test data rates were chosen, 1 Gbit/s, 2 Gbit/s and 3 Gbit/s. The upper limit on the data rate was 3 Gbit/s because of the 3 GHz bandwidth limit of the digitizing oscilloscope used to capture the outputs. The data sequences were delay-self-heterodyned using an interferometer with one arm having an optical path delay of 1 bit. We padded the beginning of the data sequence with 1's for ease in decoding of the data later. A peizo electric transducer was used to move a mirror within the interferometer, which changed the phase of the light in the padded region to make it destructively interfere. A simulated representation the first 16 bits of the 256 bit digital input sequence to the modulator is shown in the top portion of Figure 21. The middle portion in Figure 21 shows the data with a simulated single bit delay introduced by the delay line. The expected delay-self-heterodyned intensity modulated output is depicted in the bottom portion of figure 21.

For the experiment, the input power, P_{in}, just outside of the slave laser was P_{in} = 400 μW. The delay-self-heterodyned output from the injection locked slave is shown in figure 22 for (a) 1 Gbit/s, (b) 2 Gbit/s, and (c) 3 Gbit/s. The output power for these sequences was P_{out} = 88 mW. It can be seen in these plots that the injection locking follows the expected output quite well for each bit rate. Over the 256 bit test sequences employed, no logic errors were observed. The eye diagrams for each data rate are shown next to each of the example

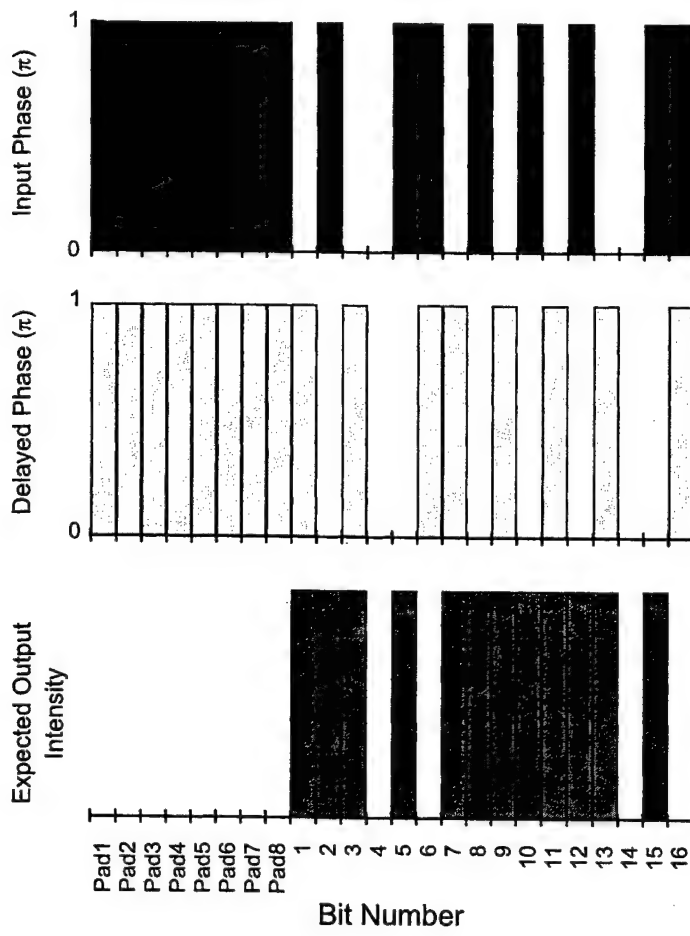


Figure 21: Digital input to the integrated optics phase modulator (top), the delayed signal (middle), and the expected delayed self heterodyned output (bottom). The start of the sequence is padded with ones for later decoding.

signals in figure 22. The modulator (without injection locking) was found to respond better at the higher data rates than at the slower rates due to the square wave nature of the BPSK and the low bandwidth limitations of the phase modulator. This helps to explain the widening of the eye diagrams for the higher data rates in the injection locked signals. Also, no phase locked loops were in place to help correct for slight phase drifts. These phase drifts would also have a stronger influence on signal fidelity at slower data rates.

In summary, we have experimentally demonstrated injection locking of integrated optical phase modulators using both CW and broadband signals. Input signals of $400 \mu\text{W}$ were amplified using an AR coated single mode diode laser as the slave. Small signal gains of up to

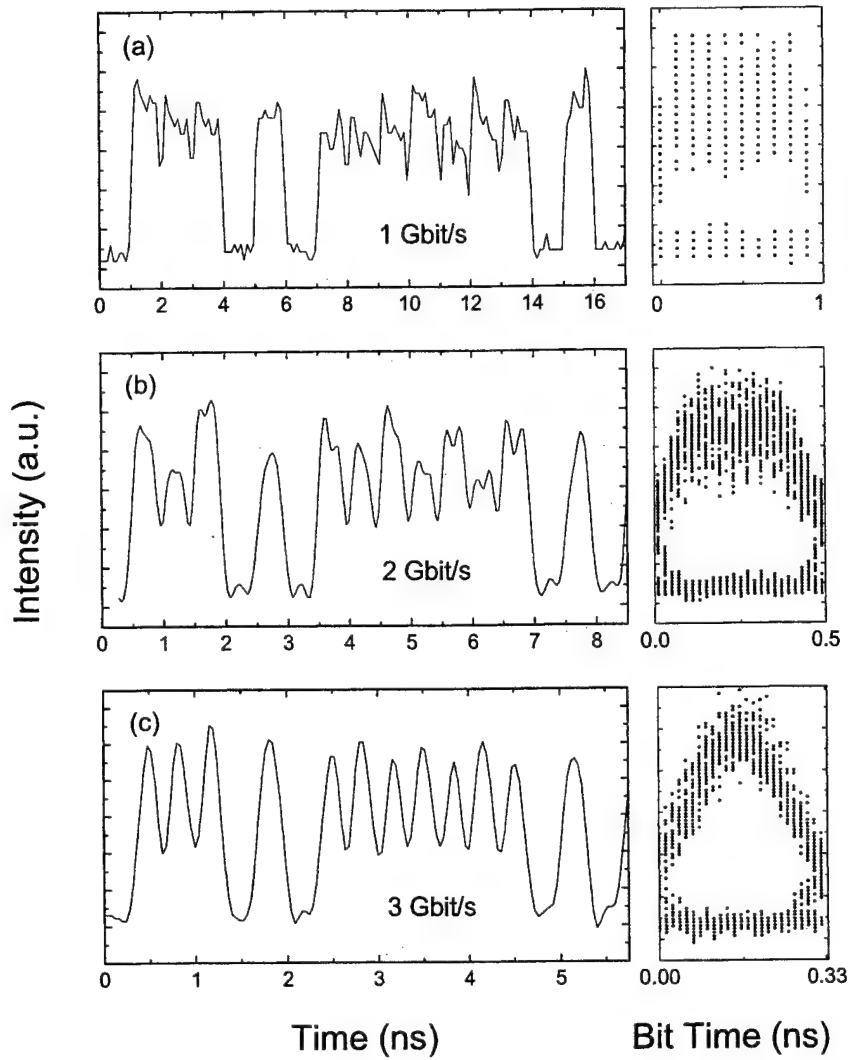


Figure 22: Bits 1 through 15 of the delayed-self-heterodyne injection locked outputs of BPSK data at (a) 1 Gbit/s, (b) 2 Gbit/s, and (c) 3 Gbit/s. Note that these outputs match the expected output shown in figure 8. To the right of the data sequence is the eye diagram for 256 bits.

23 dB were found with good signal fidelity up to 3 GHz for CW and BPSK modulated signals. There were also no logic errors observable in the delayed-self-heterodyne measurements of BPSK signals up to the measurement limits of 3 GHz. This reliable amplification technique will be useful in applications such as high bandwidth spatial-spectral holography which need

higher powers for wide bandwidth experiments.

4.3 Temporally Overlapped Linear Frequency Chirps and Programming Methodology

Through the duration of this MURI grant, we have studied several multi-gigahertz programming schemes for programming broadband TTD gratings. This year we proposed and demonstrated a new approach: accumulated programming with two temporally overlapped, frequency offset, linear frequency chirps (TOLFC's). Among the needs of a TTD system, are the materials abilities to handle the dynamics for continuously programmed continuous processing, the spectral filtering effects for amplitude and phase-modulated (AM and PM) RF signals, the delay range, delay resolution and bandwidth limitations. In order to meet the demands for high bandwidth programming laser sources and amplification schemes had to be developed. This required designing of a chirped external cavity diode laser (CECDL) with the capability of linear frequency chirps of more than 2 GHz within $1\mu\text{s}$ as well as development of a broadband injection locking amplifier. Construction and design of this CECDL was done with support from the Army Research Office DEPSCOR grant #DAAG55 – 98 – 1 – 0244 and the injection locking amplifier is discussed in a following section. Among some of the other problems that needed attention were the frequency stability of laser sources for accumulated programming of TTD gratings. This required that we study and design frequency stabilization systems for a cw Ti:Sapphire laser as well as for diode lasers so that the accumulated programming could be studied effectively. As was reported in the last report, this stabilization was carried out and characterized for a Ti:Sapphire system. This laser in conjunction with the TOLFC programming method detailed below, has led to experimental results showing the dynamics of accumulated gratings. Through understanding and simulating these dynamics we are better able to predict and construct a TTD system.

4.3.1 Low Bandwidth TOLFC Programming

We developed a novel TTD technique that will be used as the backbone for an OCT TTD system. This technique utilizes several exciting properties of linear frequency chirps, including the ability to program with temporally overlapped optical beams. The logical progression of this technique includes original work done in our lab on linear frequency chirps (LFCP's) by Dr. Kris Merkel at low bandwidths.¹³ This was the first demonstration of programming TTD gratings with chirps. The benefits of this programming technique include lower programming powers, picosecond timing resolutions, and the ability to use frequency tuning to directly control the delay of the signal. Figure 23 (a) shows how one can use LFCP's to program a spectral grating. The problem associated with producing two

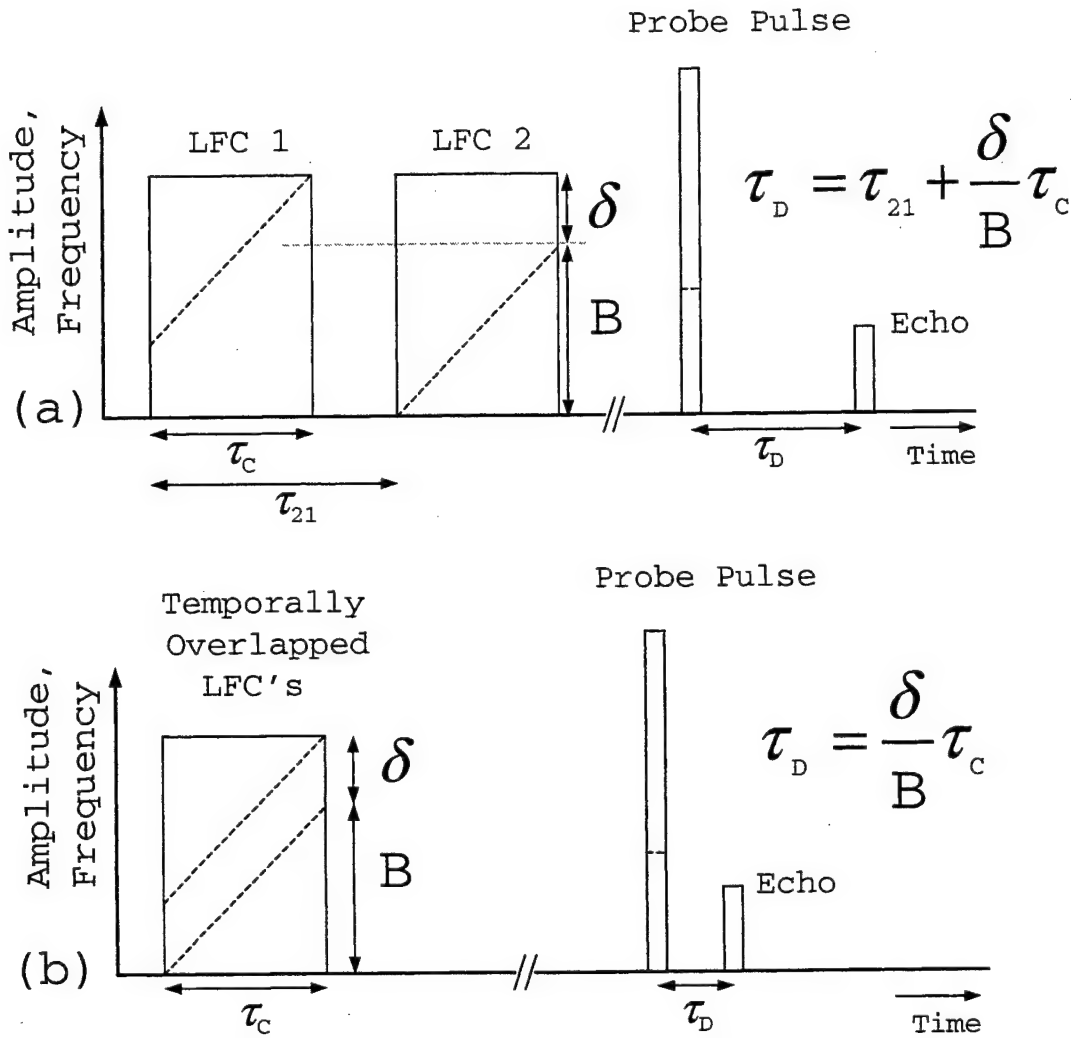


Figure 23: Input sequences and expected echo for (a) Two LFC's separated by a delay τ_{21} (b) Two temporally overlapped LFC's. Solid lines represent amplitude and dashed lines represent frequency.

identical optical chirps let us to expand upon this technique by removing the time delay from the LFCP's, which allows a single LFCP to be used to create the two TOLFC's shown in Figure 23(b). In this method, the frequency offset then directly controls the time delay of the output echo signal.¹⁴ Benefits of this approach include, 1) the ability to program with chirped pulses of duration longer than the coherence time of the crystal, which alleviates the strict requirements on the chirp rate of the laser source, 2) reduced architecture and a relaxation of the laser stability requirements for accumulation of spectral gratings, and 3) controlling the broadband spectral structure with narrow band acousto-optic modulators

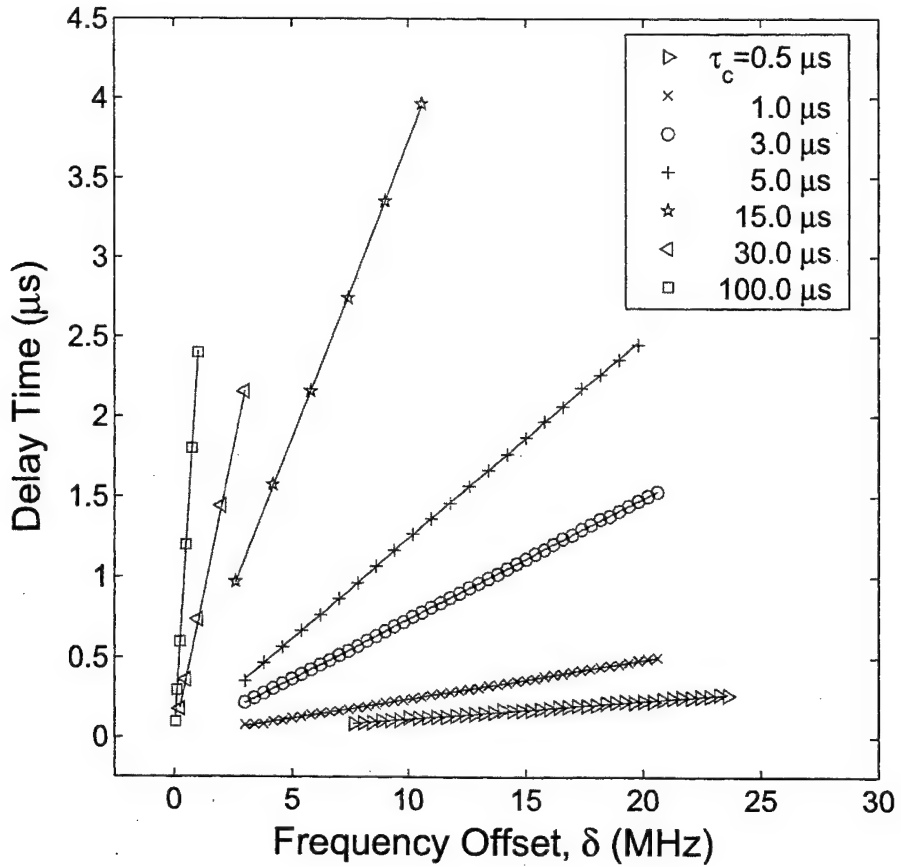


Figure 24: Measured echo delays vs. frequency offset for several different τ_C 's with solid lines calculated from the expected delay time. The lines for $\tau_C = 30$ and $100 \mu s$ demonstrate the reduced chirp rate requirements.

that provide the necessary frequency offsets.

Using a linear frequency chirped laser source enables us to access a broad bandwidth with relatively low optical powers to program efficient OCT TTD gratings. The 50 mW output from a diode laser was focused to a $70 \mu m$ diameter spot and produced sufficient processing efficiency with a single programming sequence at a chirp rate of $1\text{GHz}/10\mu s$.¹⁵ This technique was used to produce efficient TTD gratings and Figure 24 shows the time delays of associated echoes versus the frequency offset, δ . The ability of this technique of programming the medium beyond the $15\mu s$ coherence time is shown for the 30 and $100\mu s$ chirp lengths. This allows broader bandwidths to be efficiently written into the medium without the need for extremely fast chirp rates and promises to be the technique of choice for extremely wide bandwidth gratings. All of these features combine to make this approach a promising one for a practical adaptive beamforming system. Thus, the research effort at MSU has been focused on developing this technology.

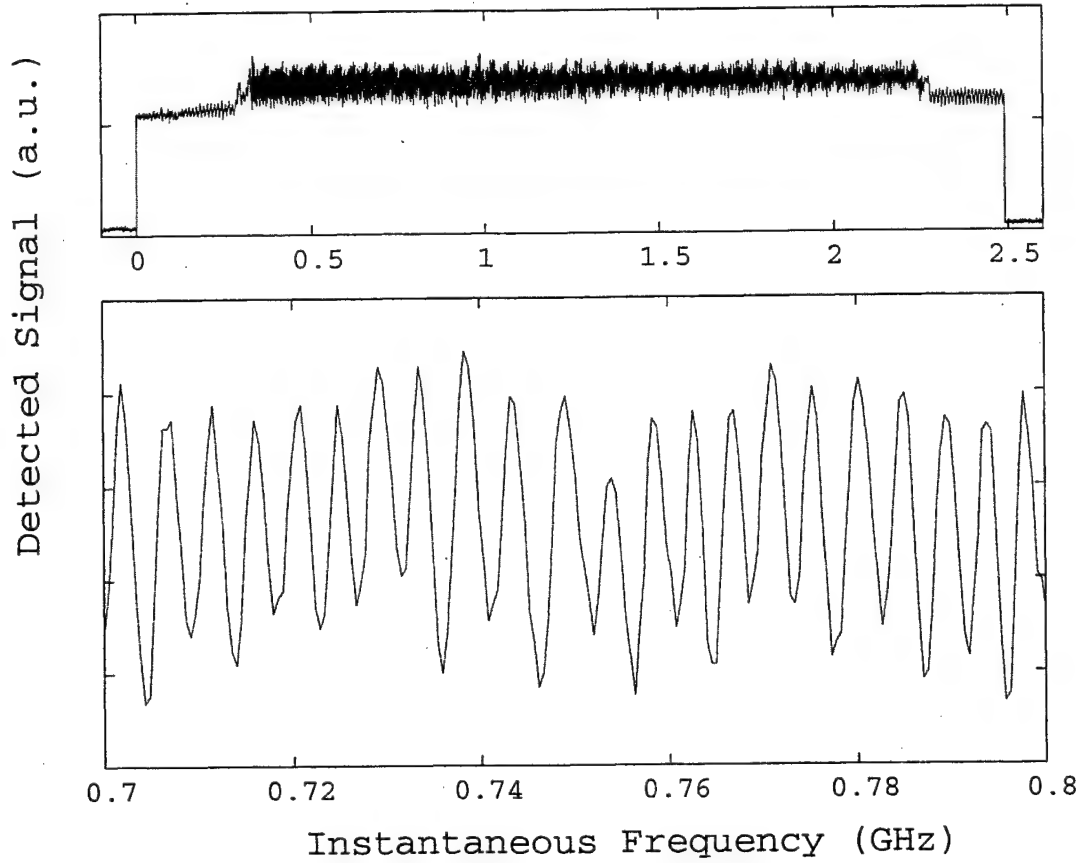


Figure 25: (a) A chirped scan over a 2 GHz TTD grating. This grating was created using the TOLFC method described in the text. (b) A zoom of a section of the grating showing the frequency spacing of the TTD grating.

4.3.2 High Bandwidth TOLFC Programming

In order to fully realize any OCT TTD system, we needed a direct method to program high bandwidth gratings. We followed the approach we demonstrated at low bandwidths using the TOLFC method, described in a previous section. The TOLFC TTD programming was first demonstrated with the CECDL with 450MHz of chirp bandwidth. Echoes were observed by scattering a 50ns pulse off of the TTD gratings created by the chirps. The delay was tuned from $0.1\mu s$ to $0.7\mu s$ by frequency offset. This frequency offset was done with a low bandwidth 125MHz AOM and the echo delay shows good linearity with the frequency offset as expected by the theory. A further enhancement of programming bandwidth to 1.2 GHz was then demonstrated. This conclusively demonstrated that the chirped laser could produce efficient high bandwidth gratings for TTD applications and was the first

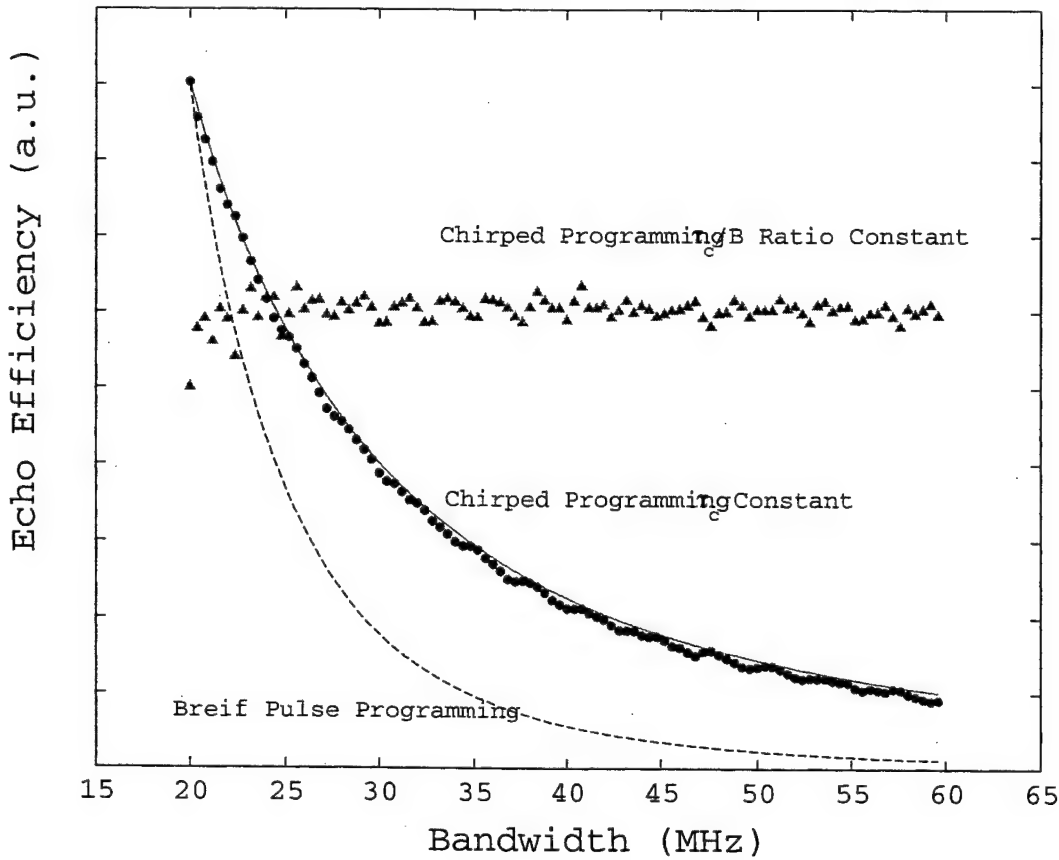


Figure 26: Data points showing simulated peak echo height versus bandwidth for a constant programming power. The solid lines are analytic solutions.

successful demonstration of broadband true-time delay gratings using a CECDL. In more recent experiments, we scanned over the TTD grating created with a slower chirp from the CECDL. This allowed a direct view of the programmed spectral grating and is shown in figure 25. Here we see that the laser can indeed chirp and create gratings with bandwidths up to 2 GHz.

4.3.3 Grating Efficiencies of TOLFC programming

The efficiency of the OCT programming used is important. We have performed simulations and experiment which directly shows the grating efficiencies for the TOLFC method and compares it with theory. In the linear regime, the echo signal in the frequency domain, $E_e(\omega)$, can be found from the relation

$$E_e(\omega) \cong E_1^*(\omega) E_2(\omega) E_3(\omega) \quad . \quad (4)$$

Here $E_1(\omega)$ and $E_2(\omega)$ are the programming pulses and $E_3(\omega)$ is the probe pulse. If the frequency chirps have an amplitude in the time domain of E_C and $E_1^*(\omega)E_1(\omega)$ is assumed flat over the bandwidth, B , and zero outside of B , that is $|E_1(\omega)| = |E_2(\omega)| = E_o$ on the interval $2\pi B$ of the LFCP, then it can be shown that the following relation holds

$$E_o = E_C \sqrt{\frac{\tau_C}{B}} \quad . \quad (5)$$

If the grating efficiency, η , is defined as

$$\eta = \frac{I_e(\omega)}{I_3(\omega)} \propto \left(\frac{E_e(\omega)}{E_3(\omega)} \right)^2. \quad (6)$$

Here I_e is the intensity of the echo pulse and I_3 is the intensity of the probe pulse. It can then be shown that the grating efficiency can be rewritten as

$$\eta \propto E_C^4 \left(\frac{\tau_C}{B} \right)^2 \quad (7)$$

Thus, the grating efficiency falls off as the inverse square of the bandwidth. This is a tremendous benefit compared to other programming methods such as brief pulses whose efficiencies fall as the inverse fourth power of the bandwidth. In addition, the LFCP efficiency is proportional to the square of the chirp duration. Thus, if we keep the ratio of chirp duration to bandwidth constant (the chirp rate), our grating efficiencies should remain quite high (2-4%) for even extremely large bandwidth gratings. Figure 26 shows different methods of programming for a constant laser power. Here we used a Maxwell-Bloch simulator shown as the data points, as well as fitted analytic curves, the solid lines. The first situation, keeps the chirp duration constant while varying B . A series of 100 simulations were done with programming B 's from 20 MHz in steps of 0.4 MHz to 60 MHz. The probe pulse had a bandwidth of 10 MHz. As can be seen, the echo intensity decreases as a function of the bandwidth as expected. The inverse square analytic solution is also plotted as the solid line. The dashed line is representative of the brief pulse programming method dropping off as $1/B^4$. The second situation is when the ratio of chirp duration to bandwidth is kept constant. In this case there should be roughly no change in echo efficiency. As can be seen from the triangles in figure 26, the simulated echo efficiencies for this situation remain relatively constant.

An experimental verification of these efficiency calculations was done with the broadband chirped laser and shows reasonable agreement to the $1/B^2$ plot. This is shown in figure 27. Here we used a low bandwidth (20 MHz) probe pulse to diffract off of gratings with different bandwidths. The chirp duration $\tau_C = 4\mu s$, and $\delta = 20\text{MHz}$. Here the delay times are all shorter than $0.6 \mu s$ and thus T_2 effects can be ignored. The solid line is a fit to the data using a $1/B^2$ functional dependence.

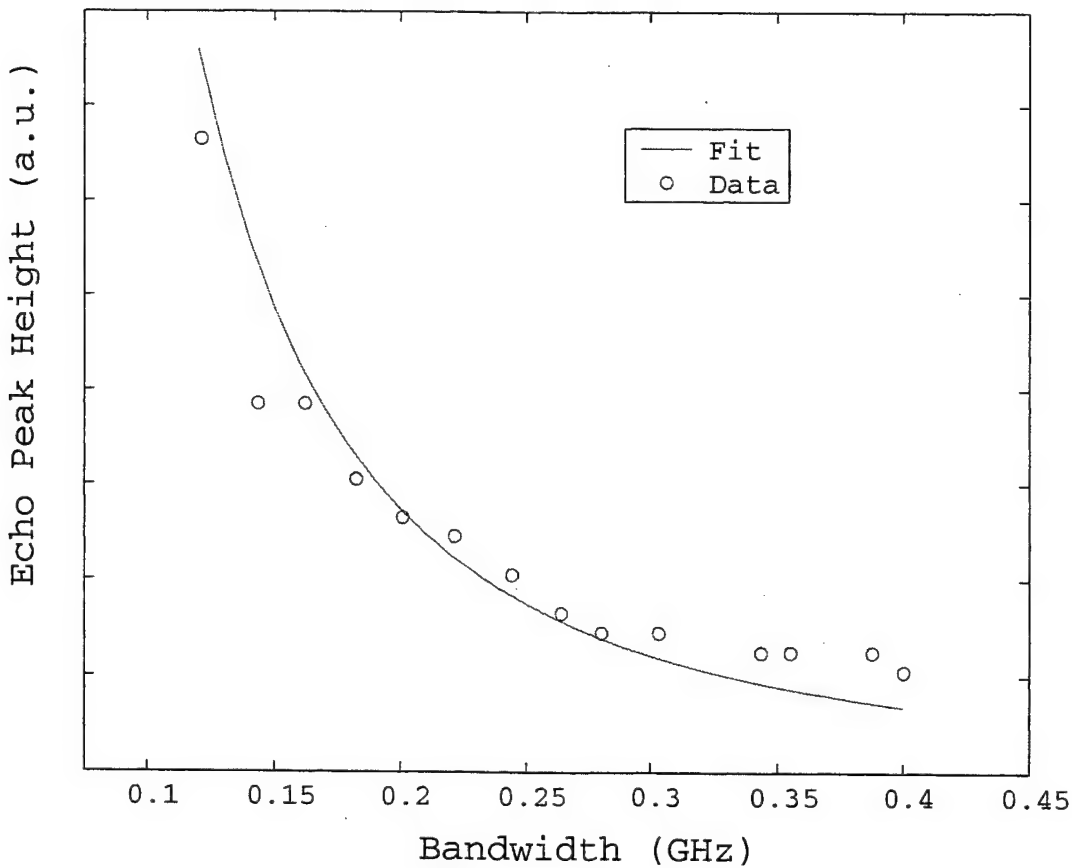


Figure 27: Echo peak heights from different bandwidth gratings. Here the probe was a 20 MHz pulse and the programming power was kept constant. The solid line is a $1/B^2$ fit.

4.3.4 Dynamics of TOLFC Programming Using Accumulation

The nature of the accumulation of TTD grating allows the processing ability being maintained or refreshed, which enables the continuously programmed continuous processing. The dynamics of the accumulation was studied with brief pulse programming on the entire available bandwidth (17 GHz)¹⁶ and on narrow band 40MHz with TOLFC's.¹⁴ The broad band results (discussed in a previous section) shows the echo efficiency at a regular level can be reached and maintained with 30 ps pulses at an intensity significantly lower than the damage threshold of the material.

To demonstrate accumulation using the TOLFC method, we first used the frequency stabilized Ti:Sapphire laser. This laser has been locked using a regenerative transient spectral hole giving a laser jitter of approximately a few tens of kHz.¹⁷ By attenuating the optical power, we chose a series of weak programming strengths that would show the dynamics of the accumulated gratings. The programming pulses are characterized by an individual LFC's Rabi frequency, which were $\Omega = 0.5, 0.6, 0.9, 1.3, 1.7$, and 2.2 MHz for this experiment. To

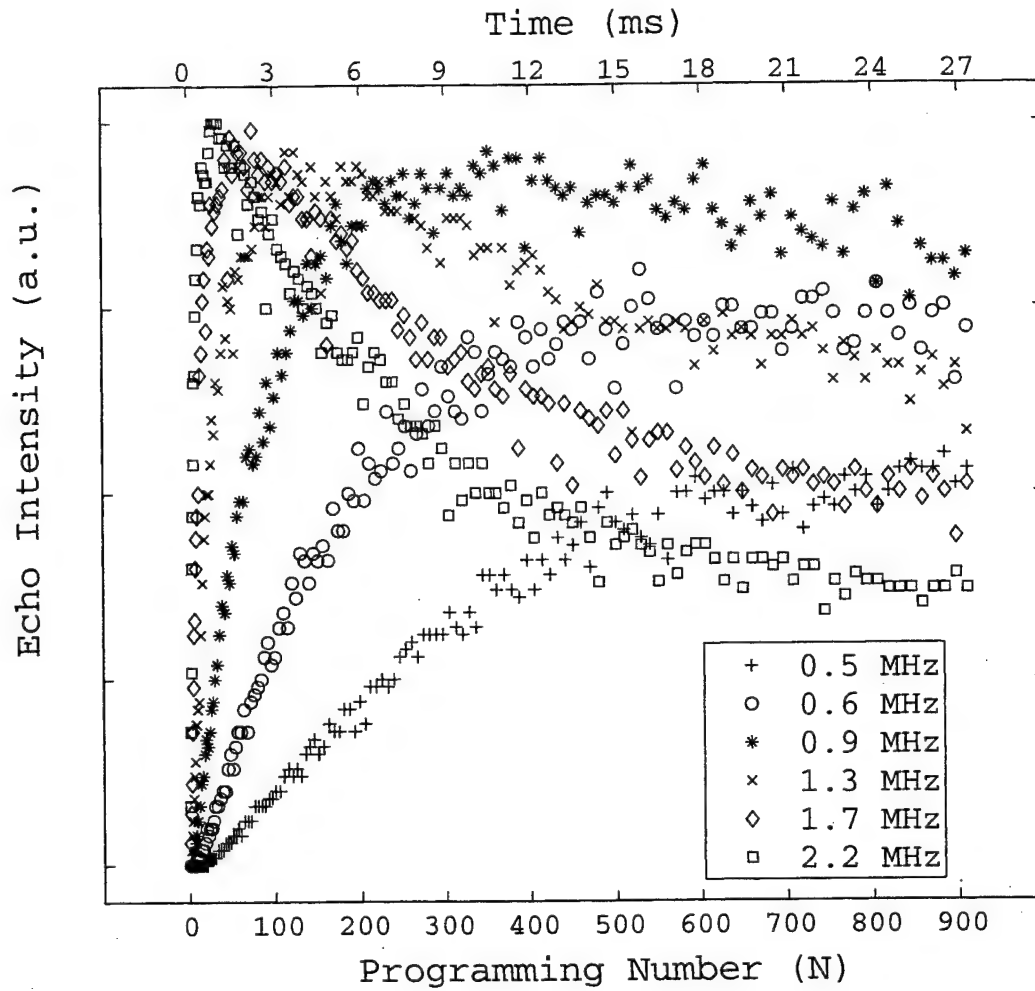


Figure 28: Experimental results for grating accumulation dynamics using TOLFC's. Here the repetition rate of programming pulses is approximately 30KHz. Notice that there is an optimum programming strength of approximately $\Omega = 0.9$ MHz for steady state accumulation.

accumulate the spectral gratings, we repeated programming TOLFC's with a repetition time, τ_r , of 31 μ s, for N times. After the N programming sequences, the grating was probed using a 50 ns brief pulse as in the single shot experiments. Figure 28 details the echo peak power as a function of N for the set of weak programming pulses. Here, $\tau_C = 1 \mu$ s and $\delta=10$ MHz giving a delay time for the echo of $\tau_D = 250$ ns. As can be seen from the figure, the various gratings accumulate quite well. Because of the population relaxation dynamics, the larger programming strengths, $\Omega \gtrsim 1.3$ MHz, are too strong and saturate the medium leading to inefficient gratings. The weaker programming strengths, $\Omega \lesssim 0.6$ MHz, are not strong enough to accumulate an efficient grating before population decay wipes them out. Between these

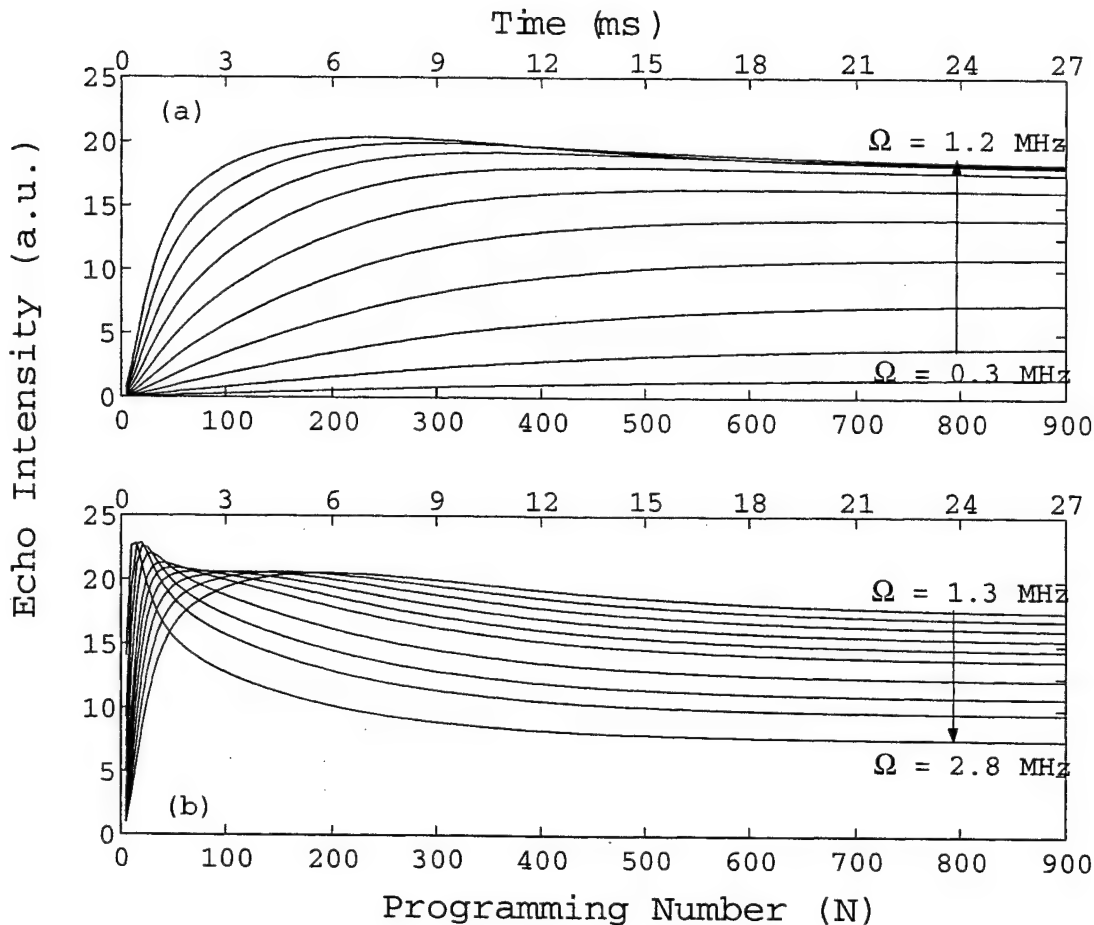


Figure 29: Simulated results for accumulated gratings matching the experimental results shown above and described in the text.

two regimes the best accumulation can be found such as the $\Omega = 0.9 \text{ MHz}$ programming strength. Figure 29 shows an example simulation using the experimental parameters. The simulation program uses an integration routine to simulate the effects of propagation through the medium using the coupled Maxwell-Bloch equations. This simulator has been specifically developed to handle these situations and as can be seen verifies the experimental results.

4.4 Linear Phase Chirp Programming and Methodology

We have recently begun to explore a promising alternative for linear frequency chirp programming (LFCP). This approach is to chirp the phase sidebands around an optical carrier using a broadband integrated optics waveguide modulator, whereas LFCP programming on a broadband requires specialized chirped lasers. A simple linear frequency chirp, as described

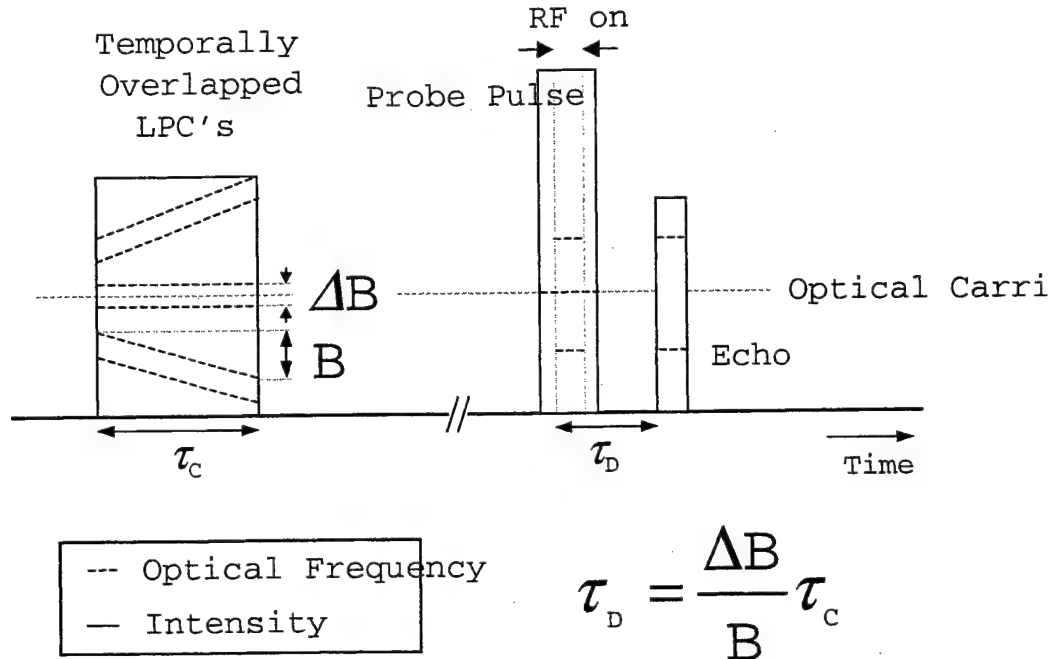


Figure 30: Schematic of a linear phase chirp (LPC) for broadband linear frequency chirp (LFC) without frequency chirped laser.

in the previous sections, is described by,

$$E_{LFC}(t) = E_o(t) \cos(\omega_o t + \frac{1}{2}\alpha t^2). \quad (8)$$

Here the chirp is created using a chirp rate α to drive the linear frequency chirp. To describe the approach of linear phase chirps (LPC's), we first look to cw phase modulation. CW phase modulation is described by the equation,

$$E_{CW}(t) = E_o(t) \cos(\omega_o t + \beta \cos(\omega_m t)). \quad (9)$$

Here β is the modulation parameter and ω_m is the modulation frequency. If we look at the optical spectra of such a signal we will find sidebands at frequencies of $\omega_{SB} = \omega_o \pm \omega_m$. Now, to describe LPC's, all we need to do is chirp the instantaneous modulation frequency ω_m . Thus, a LPC is described by

$$E_{LPC}(t) = E_o(t) \cos\left(\omega_o t + \beta \cos\left(\omega_s t + \frac{\alpha t^2}{2}\right)\right). \quad (10)$$

Here, we have defined a start frequency, ω_s , because this approach requires that we must start with some initial modulation frequency (i.e. we can not start at DC). We also define

β small enough so that second order effects can be ignored. We can use LPC's in much the same way as LFC's are used. Thus, all of the techniques described above can be utilized. For example, the TOLFC method to program a TTD grating has a similar method of temporally overlapped linear phase chirps (TOLPC's), which will also program TTD gratings. Figure 30 shows the pulse sequence of such an experiment. Here the instantaneous frequency of the optical spectra is plotted vertically along with the intensity of the laser. The TOLPC's are frequency shifted using an AOM and give rise to two TTD gratings. The two gratings are symmetric about the carrier and are caused by the fact that phase modulation creates an upper frequency sideband and a lower frequency sideband. If we now probe the gratings using a cw phase modulated pulse, such that ω_m puts sidebands out at the sideband gratings created by the LPC's, a TTD echo can be observed. If the inputs are collinear, the carrier will not be scattered but the sideband will diffract creating a beat frequency of $2\omega_m$. But, the experiment need not be collinear.

A box geometry can also be used, in which case the two spectral sidebands of the echo are spatially separated. Only one sideband is diffracted in the output direction and this sideband can be heterodyned with a carrier to achieve a TTD rf signal. We demonstrated variable TTD tuned by offset frequencies and the results are shown in figure 31. The programmed bandwidth was $B = 300$ MHz, $\omega_s = 2$ GHz, and $\tau_c = 50$ ms. The time delay of the echoes can be seen to increase as the frequency offset δ is increased as expected. In the experiment shown, the cw phase modulation is only on for a portion of the probe pulse.

In figure 32 we show experimental results where we used gratings created by the LPC method to TTD a phase modulated carrier. Here the programmed grating was 1.25 GHz wide. The carrier of the phase modulation was positioned on the lower frequency edge of the grating and only the higher frequency sideband was diffracted along with the carrier. This created a TTD echo with a cw amplitude modulated signal of 1 GHz. Essentially phase modulation is spectrally filtered and gives rise to amplitude modulation. As above, we varied the frequency offset, δ , to give various TTD echoes. The graph shows these various 1 GHz signals that have different TTD depending on the frequency offset. Approximately 430ps separate each subsequent echo.

Figure 33 shows the Fourier transform of one of these signals 1GHz amplitude modulated signals and shows good theoretical agreement. This demonstrates that the signal fidelity is good and that these signals could be used to directly steer a cw rf phased array. Finally, from the Fourier transform of each echo signal we extracted the phase information. One expects to find for any TTD signal a phase shift, ϕ , such that

$$\phi = 2\pi f_m \tau_d. \quad (11)$$

Here f_m is the modulation frequency of the signal and τ_d is the time delay. The phase of the echo signals is plotted as a function of the relative time delay in figure 34 and fit to a

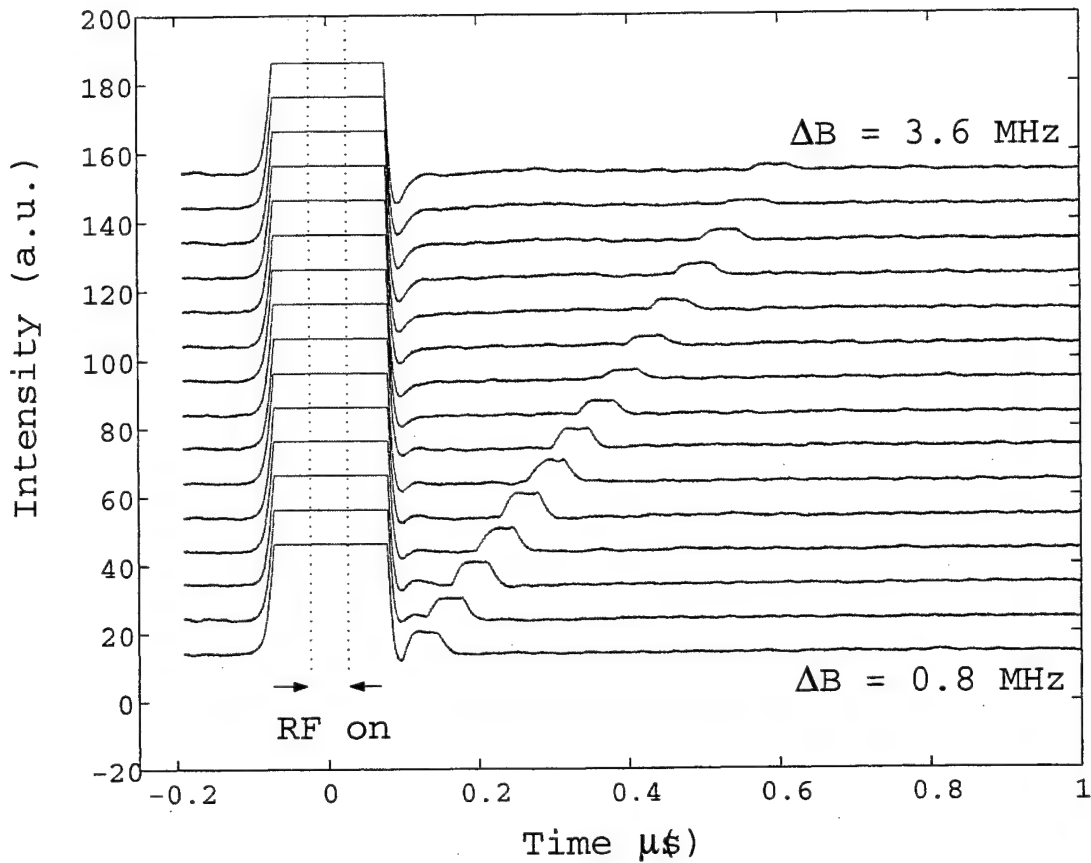


Figure 31: Shows true-time-delayed echoes for various offset frequencies δB . The programming was done with TOLPC's and the probe pulse only has a cw phase modulation in the center of the probe giving rise to the smaller temporal width of the echoes.

line. The slope of this line agrees quite well with the phase equation above giving close to 2π . Along with this the rms deviation from the line is 0.38 radians, which corresponds to a delay resolution of 45 ps.

Phase chirping has several advantages that make it attractive as a possible programming method. Along with the fact that two gratings are created simultaneously, they are separately addressable spatially. Phase chirps always have a frequency stable carrier present and the modulation is done external to the laser. This is extremely important as this means that a stabilized ECDL could be used as the carrier for the LPC's giving them sub-kHz spectral resolution which LFC's from CECDL's can not presently rival. Broadband phase modulators have also become a popular tool of the communications community and are compact, affordable devices.

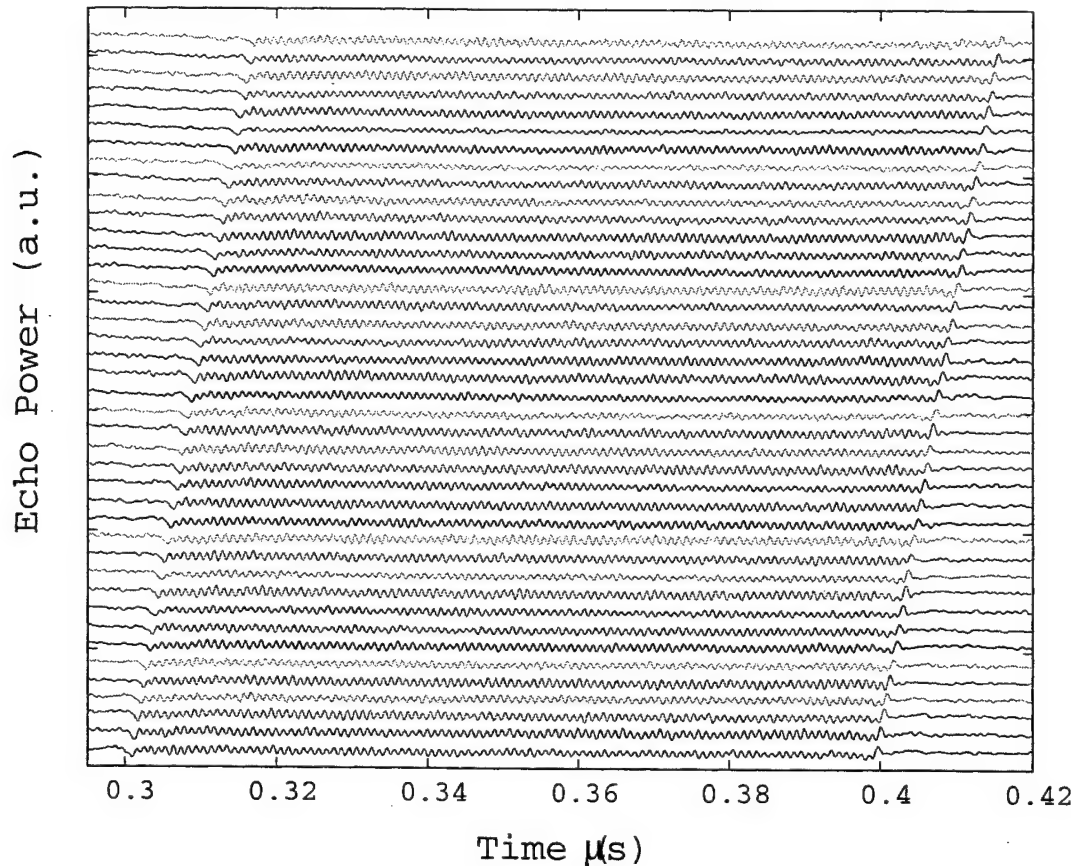


Figure 32: Echoes with a 1 GHz RF amplitude modulation created from diffracting a 1 GHz cw phase modulated signal off of LPC created gratings. Here various TTD's are shown.

4.5 Two-Element Array Steering Demonstration

For pursuing a two element antenna array demonstration, we have begun fabricating and testing an improved design of the Vivaldi antenna. The current design is modeled after a description given by Gazit.¹⁸ With improvements to the stripline feed, these antennas have better bandwidth characteristics and slightly more compatible impedances. These antennas were developed at University of Colorado-Boulder by Zoya Popović group. With bandwidths from 0.5-3.6 GHz these elements are ideally suited for our two-element beam-steering demonstration. By utilizing their design we have fabricated these elements on site and have successfully reproduced their design. Initial testing has been completed showing transmission and reception of rf signals over the bandwidths of the antennas. Measurements of the two-element antenna pattern is being complicated by the lab environment and methods to make cleaner measurements are being explored. Once this is solved, we plan to use these antenna elements in conjunction with the OCT TTD system to achieve a two element

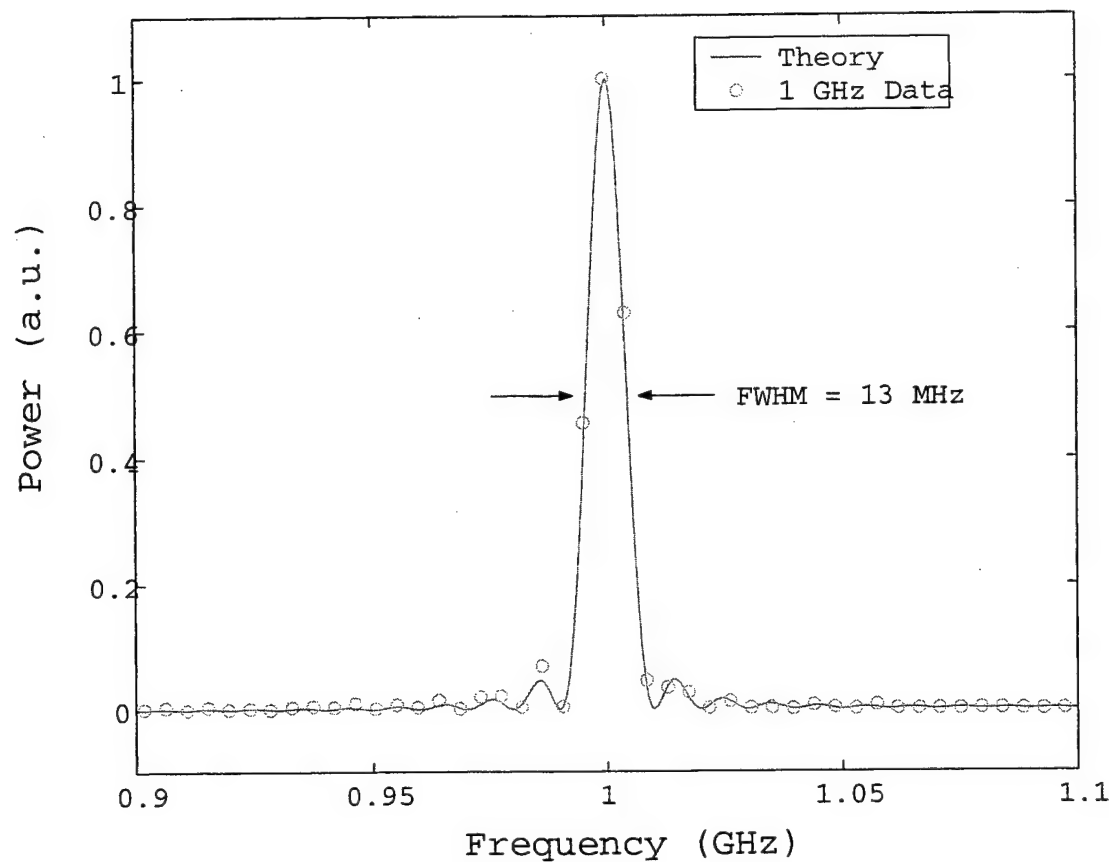


Figure 33: A Fourier transform of a single 1 GHz amplitude modulated echo signal showing the high quality spectral characteristics.

beamsteering demonstration.

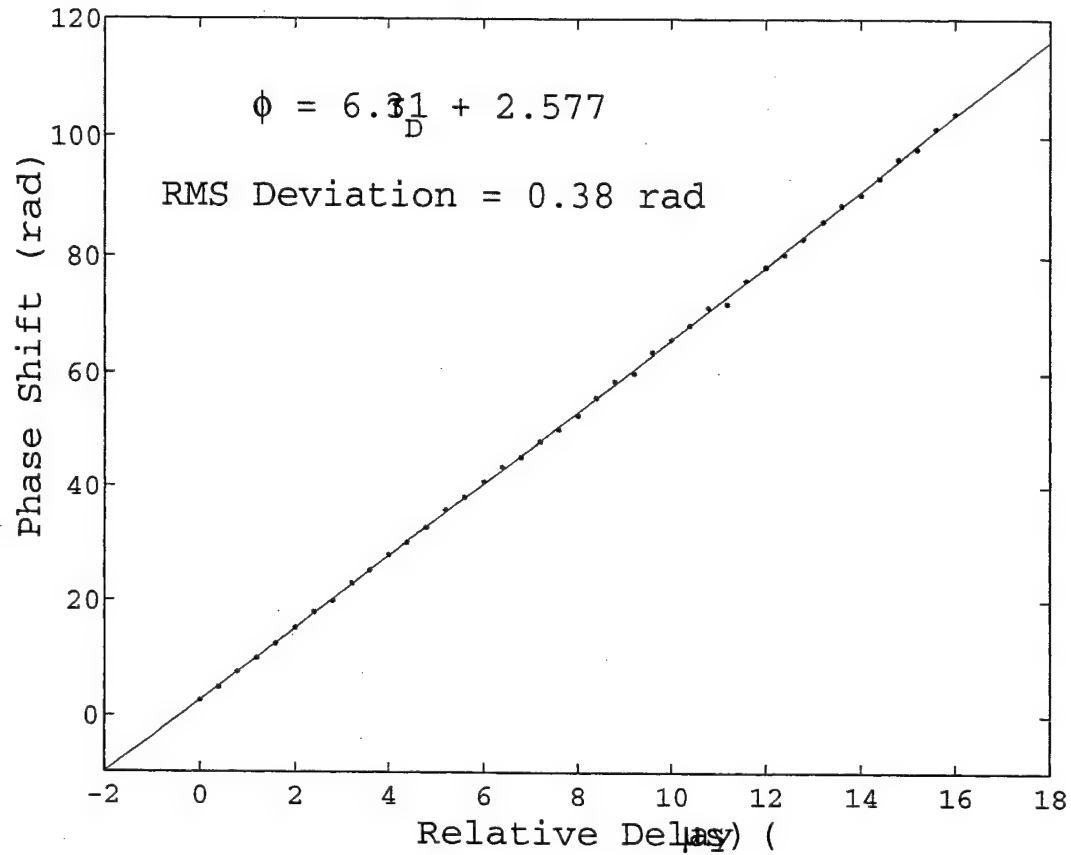


Figure 34: The phase shift plotted as a function of the relative delay. A fit line gives a slope close to the expected 2π and the rms deviation gives a time resolution of 45 ps.

5 Algorithmic Development

Principal Investigator: Lloyd Griffiths, George Mason University, Information Technology

Because previous implementations of BEAMTAP¹⁹ required a desired signal to steer the array, they were limited to communication scenarios and were incapable of preserving Doppler and delay information for radar applications. However, by using the all-optical beam-steering system, as described in Sec. 3.3, to derive the desired steering signal for BEAMTAP, Doppler and delay information is preserved. This allows the modified version of BEAMTAP (which is based upon the P-Vector adaptive algorithm²⁰), to perform adaptive broadband beam steering and jammer nulling for equi-spaced, linear and planar arrays for both radar and surveillance scenarios.

5.1 P-Vector BEAMTAP

In the P-Vector based BEAMTAP algorithm, the desired signal is generated from the beam-steering system, which is shown algorithmically in Fig. 35. (For simplicity, only the 1-D case is considered here.) The signal $s_n(t)$ arriving at each antenna element of a linearly spaced array will be composed of a signals $r_d(t)$ arriving from the farfield desired angle θ_d , delayed at each antenna element by a successive differential time delay $t_d = d \sin \theta_d / c$, where d is the spacing between antenna elements; and a number of jamming signals $j_j(t)$, each with their own differential time delays $t_j = d \sin \theta_j / c$, so that

$$s_n(t) = r_d(t - nt_d) + \sum_j^{\text{jammers}} j_j(t - nt_j). \quad (12)$$

Thus, if we delay the signals from each antenna element by $(N - n)\tau_d$, where τ_d is a variable time delay determined by the desired angle of arrival and chosen to be equal to t_d , then after the beam-steering system the steering (or pointing) signal $d(t)$ can be described by

$$\begin{aligned} d(t) &= g_0 \sum_n s_n[t - (N - n)\tau_d] \\ &= g_0 \cdot \left(N r_d(t - N\tau_d) + \sum_j \sum_n j_j[t - N\tau_d - n(t_j - t_d)] \right), \end{aligned} \quad (13)$$

where g_0 is the amplifier gain for $d(t)$. Notice that the signal components arriving from the desired direction are coherently and synchronously time-delay-and-summed so that they experience the full array gain of the processor while the jamming signals, inappropriately time delayed, will reside in the sidelobes of the main beam.

Next, a feedback signal $f(t) = d(t) - o(t - N\tau_d)$, where $o(t)$ is the adaptive nuller output, is used to adapt a weight matrix to the signals coming from the antenna array $s_n(t)$ —delayed

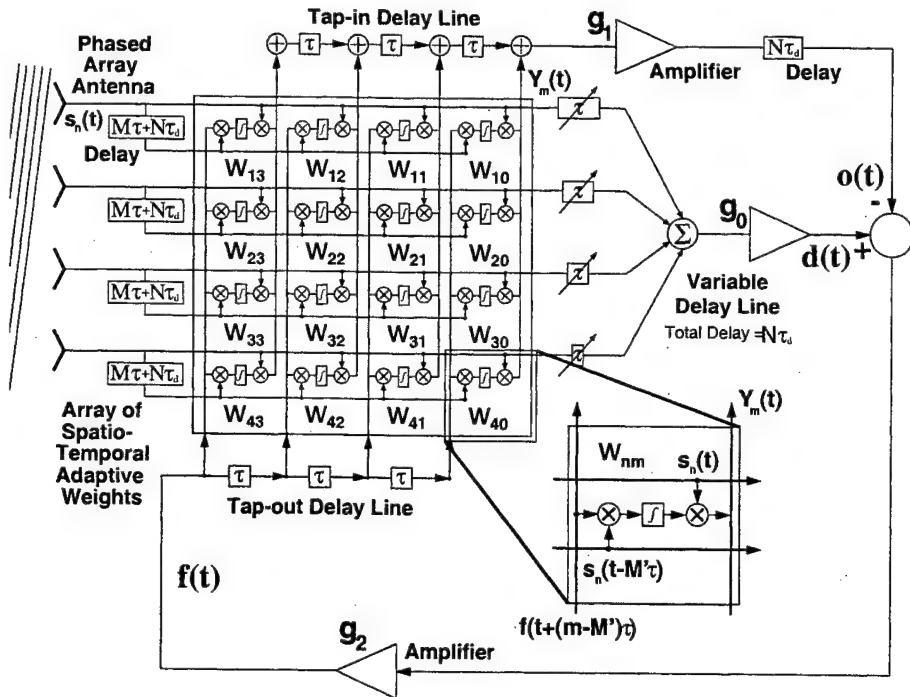


Figure 35: Algorithmic representation of the true-time-delay (TTD) beam-steering system combined with the BEAMTAP adaptive jammer-nulling system.

by a time $M\tau + N\tau_d$ in order to ensure causality—by a cross-correlation. The feedback signal is input into the tapped-delay line, containing M taps, producing adaptive weights described by the time-integrated correlations

$$W_{nm}^*(t') = \int_{-\infty}^{t'} s_n^*(t_1 - M\tau - N\tau_d) f[t_1 - (M - m)\tau] dt_1. \quad (14)$$

When the weight matrix is read out by multiplication with the instantaneous signals from the array $s_n(t)$, fed into the scrolling and accumulating delay line, and amplified by g_1 , the output $o(t)$ becomes

$$\begin{aligned} o(t) &= g_1 \sum_m \int_{t-T}^t \delta[t' - (t - m\tau)] \sum_n s_n(t') W_{nm}^*(t') dt' \\ &= g_1 \sum_n \sum_m s_n(t - m\tau) \int_{-\infty}^{t - M\tau - N\tau_d} s_n^*(t_3 - m\tau) \left[N r_d(t_3) + \sum_j \sum_n j_j [t - n(t_j - t_d)] - o(t_3) \right] dt_3. \end{aligned} \quad (15)$$

This describes a convolution-correlation integral between the signals from the antenna array with the desired pointing signal. Notice that there will be a correlation between the signal of interest $r_d(t)$ in the pointing signal with the signals containing $r_d(t)$ from the antenna array. This is because $s_n(t)$ contains both the signal of interest as well as the jamming signals. However, notice also that the jamming signals which leak through the sidelobes of the main beam in $d(t)$ will also write a grating with $s_n(t)$. This means that the

feedback loop will drive the weights to optimally point a beam toward the direction of any jamming signals as well. If the final output is taken to be the feedback signal $f(t)$, instead of the output signal $o(t)$, at the differencing node the system will try to null out both the signal of interest as well as the jamming signals. The problem of unwanted signal nulling using $f(t)$ for the final output can be avoided, though, by appropriate balancing of the gains around the loop. Because the jamming signals reside on the sidelobes of the steering signal $d(t)$, but are optimally detected in the output signal $o(t)$, the two jammer power levels will be considerably different. However, the signal of interest is optimally beam formed with the full array gain in both ports. Thus, by setting the gains g_0 and g_1 so that very little of the signal of interest is subtracted after the differencing node, there will still be enough jammer power in the output port to fully subtract the jammer signal residing on the sidelobe of $d(t)$. The system adapts so that it will null any broadband jamming signals while still directing a high gain, squint-free beam toward the angle of the signal of interest.

5.2 Optical Implementation of P-Vector BEAMTAP

The optically implemented, multiple beam-steering and jammer-nulling BEAMTAP array-processor system based on the P-vector adaptive-array algorithm is shown in Fig. 36. A single laser is split and illuminates an array of electro-optic modulators (EOMs) that convert the incident RF waveform on each antenna (or each sub-array) into modulated optical signals. The signals are coherently fiber remoted (preserving the array topology), holographically phase cohered to accommodate fiber length errors, and then novelty filtered to remove the excess carrier. Finally, the signals are passed through the BEAMTAP photorefractive crystal into a 2-D TTD beam-steering system to produce a main-beam output. All the time delays along lines perpendicular to the beam-steered direction are equivalent, so the optically-modulated antenna signals can first be summed from all the array elements with identical time delays^{2,21} by using a cylindrical lens to focus the light onto a parallel-aligned on-axis slit; then the squint-free beam is produced by TTD beam steering the linear array of summed signals. This is done by using a fiber prism delay line to impose a linear delay ramp across the entire array of signals so that the velocities from all elevations are traveling in the same direction. Matching the TDI shift velocity with the fringe velocity from each elevation angle by varying the gap spacing of the electrodes then allows each signal to be appropriately delayed-and-summed to give the final squint-free output.

The TTD-formed main-beam output can then be used as the desired signal and be applied to a BEAMTAP based jammer-nulling adaptive-array processor.¹⁹ However, in this case it is likely that jammers may be in the array sidelobes and leak through into the desired signal. The nulling detector output $o(t)$ is therefore subtracted from the TTD main beam $d(t)$ and applied to the acousto-optic deflector (AOD). The interference of the array signals with

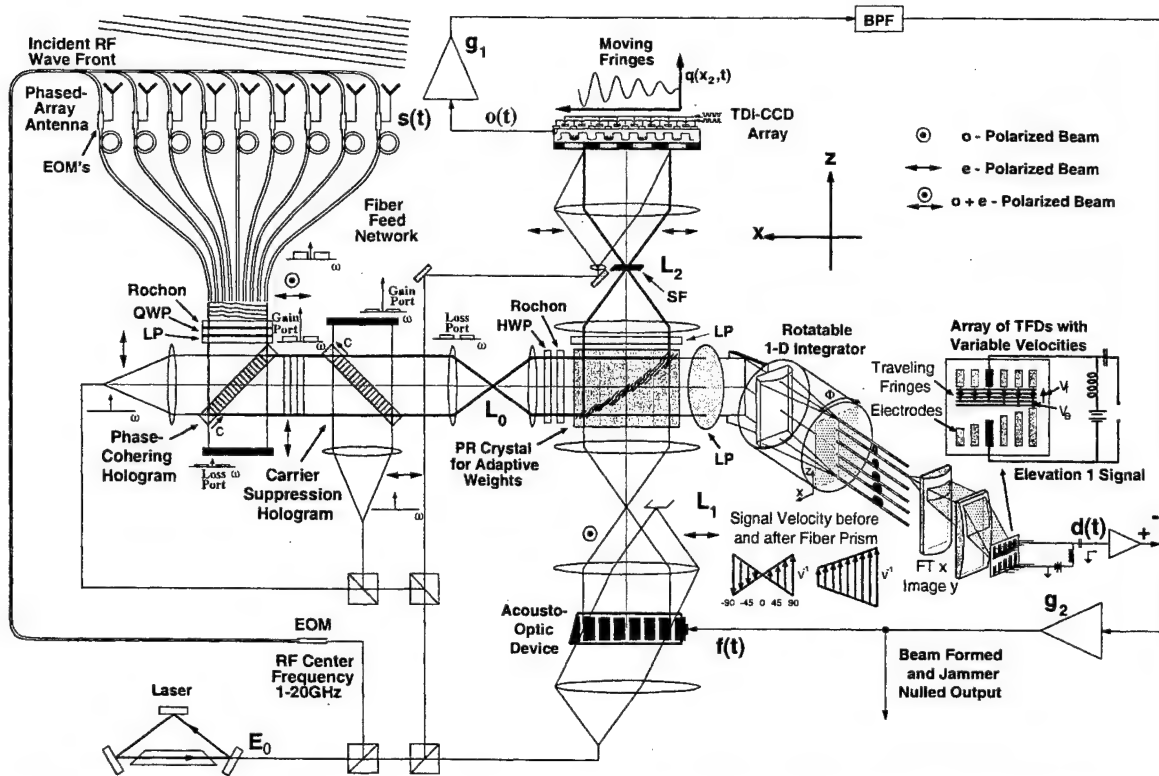


Figure 36: A coherently-modulated, fiber-remoted, 2-D antenna array that is first cohered and carrier suppressed with photorefractive 2-wave mixing, and then beam-steered using image rotation and 1-D integration onto a velocity-matched TFD. Closed-loop feedback to the BEAMTAP photorefractive adaptive weights suppresses any unwanted jammers or interference on the main-beam sidelobes.

the feedback builds up dynamic gratings throughout the crystal volume that are separately Bragg matched to the signal of interest and each jammer seen by the side lobes of the main beam. The main beam and jammers are then diffracted onto the scrolling TDI-CCD detector array, where they interfere with the DC beam to produce velocity-matched moving fringes scrolling synchronously with the TDI-CCD. The coherent summation of these synchronously moving interference fringes de-skews the signals and jammers arriving on different antenna elements at different times so that the difference node is driven toward zero. However, because Gaussian apodizing of the array can produce sidelobes which are -30 dB or lower compared to the power of the main beam, there is a difference between the available jammer power in the beam-steered output port $d(t)$ compared to the BEAMTAP beam-formed output at $o(t)$. This allows the gains g_0 and g_1 to be set so that the jammers on the sidelobes of the main-beam are nulled, but the main-beam signal is not. Thus a jammer-nulled, beam-steered output can be produced.

To provide greater insight into the importance of the gains g_0 and g_1 in order to produce

Table 6: Multiple Beam-Steered Output $d(t)$

Array Processing Sub-System	Signal/Jammer Gain (dB)	Signal Power (dBm)	Jammer Power (dBm)
Antenna Element	—	-90	-30
Array Gain	40/10	-50	-20
Amplification g_0	40/40	-10	20

Table 7: BEAMTAP Output $o(t)$

Array Processing Sub-System	Signal/Jammer Gain (dB)	Signal Power (dBm)	Jammer Power (dBm)
Antenna Element	—	-90	-30
PR Diffraction Eff.	-30/-30	-120	-60
Array Gain	40/40	-80	-20
Amplification g_1	40/40	-40	20

a jammer-nulled, yet strong main-beam output, first consider that the desired main-beam contribution need not necessarily be stronger than the jammer, but instead, that the antenna gains available toward the main beam and jammer on the two arms of the processor are different. A desired signal level may be -90 dBm at each antenna element after pre-amplification and electro-optic conversion, while the jammer power may be on the order of -30 dBm. With an array of 10^4 elements, the main beam forms toward the desired signal using the multiple beam-steering system with 40 dB of gain so that the desired part of the main beam power is now -50 dBm. The jammer power however, will reside on a -30 dB sidelobe of the main beam due to Gaussian apodization of the array, and will thus experience a net gain of only 10 dB so that the jammer power is now at -20 dBm. After detection, both the signal and jammer are amplified by g_0 with 40 dB of gain so that the final output of $d(t)$ is at -10 dBm and 20 dBm respectively, for the signal and jammer powers. This is outlined in Table 6.

Table 7 describes what happens in the BEAMTAP port. Again, the signal and jammer powers are initially at -90 dBm and -30 dBm. If we next consider that the photorefractive diffraction efficiency in an adaptive loop will have a maximum efficiency of 0.1 % (-30 dB), the maximum signal power at the TDI-CCD will be -120 dBm, and for the jammer, -60 dBm. But unlike the multiple-beam steering system, the feedback signal will adapt the weights within the photorefractive so that a main beam is pointed both toward the signal of interest and the jammer. This is because $d(t)$, which partially determines $f(t)$, contains both signal

and jamming components, as seen in Eq. 13. Although the jamming signals are not properly time-delayed, the grating within the crystal will adjust itself so that the jamming signal is coherently combined at the TDI-CCD. **Thus both the signal of interest and the jammer experience the full array gain of 40 dB in the BEAMTAP port.** The signal and jammer powers, after detection, are then -80 dBm and -20 dBm. A gain g_1 of 40 dB sets the final beam beam signal and main beam jammer output at -40 dBm and 20 dBm, respectively. When we try to subtract the desired main-beam output $d(t)$ (which is at -10 dBm since it was formed by the multiple beam-steering system) with the output from the feedback loop $o(t)$ at -40 dBm, the final main beam-formed output drops by 0.1 %. However, the jamming signal in the desired main-beam output $d(t)$ is at 20 dBm, while the jamming signal power in the BEAMTAP output signal port $o(t)$ is at 20 dB as well! Therefore, there is enough available jamming power in the BEAMTAP output signal port $o(t)$ to be adaptively adjusted to the 20 dB level in the desired main-beam signal port $d(t)$ by the photorefractive crystal to subtract the jammer. This way the nearly exact balance the jammer powers in the two arms of the processor will providing excellent jammer nulling. However, because the gain g_1 is too weak to sufficiently amplify the $o(t)$ main-beam signal power from -40 dBm to -10 dBm, not more than 0.1 % of the main beam signal power is ever lost. This means that the apodization of the array to -30 dB down (or perhaps much better) on the sidelobes is extremely important, since it provides a good range of gains g_1 which will allow the suppression of any jammer signals without killing the main beam signal.

6 The optically smart antenna array

Principal Investigator: Dana Anderson JILA, University of Colorado.

6.1 Overview

Our prototype 2-channel system is schematically shown in Figure 37. As a reminder, the front end consists of a 30-element discrete lens antenna array followed by active antenna receivers positioned along the focal arc of the lens. This provides a pre-separation of signals, but the signal isolation is limited by the gain pattern of these small antennas. Each receiver signal is down converted and is imposed on an optical carrier via electro-optic modulators. The modulated optical beams then go through the nonlinear optical circuit consisting of the carrier suppression stage and the auto-tuning filter. The carrier suppression stage precedes the auto-tuning filter and prepares the signals for the latter. The auto-tuning filter uses correlations between its input signals to distinguish between them and select the principal component. The incoming modulated beams contain a common optical carrier, which results in an unwanted correlation between the signals. The purpose of the carrier suppression is to remove this unwanted correlation by removing the common carrier. The filter extracts the principal component from the various signals presented at its input.

Photorefractive nonlinear optics are the “smart” part of the optically smart antenna array: the auto-tuning filter is a photorefractive ring oscillator that extracts the strongest microwave signal received by an antenna array with no foreknowledge of any of the signals. The carrier suppression is achieved by a two-beam coupling interaction within a photorefractive crystal. The importance of the photorefractive coupling in our system explains our theoretical research about general photorefractive two-beam coupling. In this year’s report we also present a systematized theoretical approach to the analysis of the auto-tuning filter. The experimental part of this section accounts for the packaging efforts that succeeded in putting the whole prototype system in a portable briefcase.

6.2 Highlights of progress

Last year we reported on an original operator theory for carrier suppression which resulted in the accomplishment of the best carrier suppression ever reported in the lab (64dB of carrier suppression). This year we extended the operator theory to the more general case of two-beam coupling with complex values of coupling constants. The research has provided an analytical solution to a case that had not been previously solved in the literature.

The processing heart of the smart antenna array system is the autotuning filter, which automatically extracts the strongest principal component of the spatio-temporal signals at

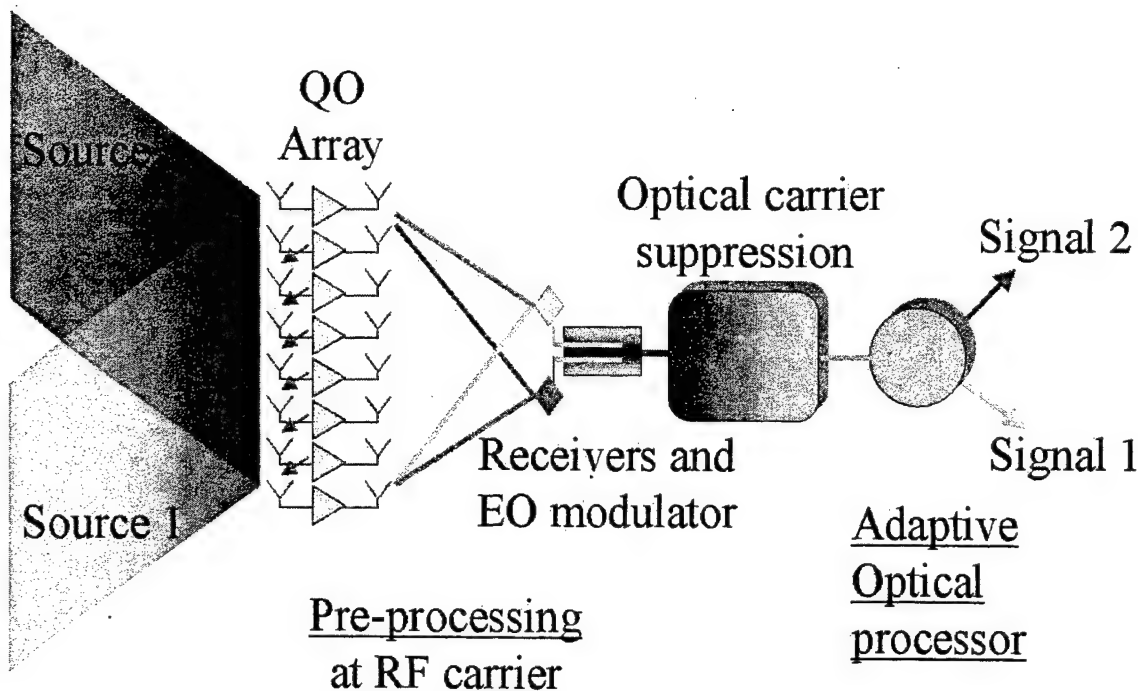


Figure 37: Block diagram of the optically smart antenna array with two sources in the far field. The active receivers are positioned on the focal arc of the discrete lens antenna. The IF signals are then imposed onto the optical beam and processed by the adaptive optical circuit.

its input. While the heuristic principles underlying the autotuning filter's operation have long been appreciated, this past year's theoretical work has led to a more systematic analysis of considerations and tradeoffs for the filter design.

In the previous report we presented the characteristics and performance of the individual components of an optically smart X-band antenna array. The RF and optical subsystems have now been completely packaged in a standard-sized 18x13x6 inches briefcase and tested with two independent sources. The briefcase draws 50W from the wall through a single power cord.

6.3 Operator theory for two-beam coupling

Much of the optical signal processing done in the context of this MURI is accomplished by or in conjunction with photorefractive media. Understanding the nonlinear optical phenomena is key to many of the processing elements such as the carrier suppression system and the autotuning filter, both of which are used in the optically smart active antenna array system. Last year we reported on the progress of a general approach to two-beam coupling in

these media. This "operator" approach provides a great deal of insight into the information-processing characteristics of these media. As pointed out, the spatial evolution of spatially and temporally encoded beams within photorefractive media is generally not analytically solvable and one usually has to resort to numerical calculations to solve a given problem. Special cases of two-beam coupling in photorefractive media are, however, analytically solvable. These special cases are especially valuable for the insight they provide for the more general cases. Using the operator approach we have discovered an analytical solution for an important special case that had not previously been solved. This is the case of two-beam coupling in which the input beams are temporally modulated with almost arbitrary time dependence except in such a way that the photorefractive grating can reach a steady-state. (The more general case in which the beams have spatial components that are independently modulated is not analytically solvable). In particular, we have derived a solution valid for any complex-valued photorefractive coupling constant. While the analytical solution can be written in one line of text, some background is needed to understand the quantities that appear in the solution.

6.3.1 Field vectors

In the operator formulation the optical electric fields are treated in terms of field vectors, vectors whose components are complex-valued scalar quantities that represent the amplitude of the electric field. For the simple two-beam coupling problem considered here, the field vectors have two components: one for each of the two beams incident on the photorefractive medium. The optical fields spatially evolve as they propagate through the medium. The propagation direction is designated here as z . Thus a field vector is written as:

$$\vec{E} = \begin{pmatrix} E_+ \\ E_- \end{pmatrix}, \quad (16)$$

where the "+" and "-" subscripts indicate the beam that will be receiving gain and loss, respectively. We use this +/- notation even when the coupling coefficient is purely imaginary so that there is no energy transfer due to the two-beam coupling interaction. In the latter special case, which port is label plus and which is label minus is arbitrary.

In general the optical fields are time-dependent, in which case we take a Fourier transform to decompose the field vectors into a set of frequency components.

6.3.2 The density matrix

The density matrix is the fundamental dynamical quantity that describes photorefractive two-beam coupling. (Here when we use the term "dynamics" we mean spatial, not temporal,

dynamics). The density matrix is formed from a superposition of outer-products of the field vectors:

$$\rho = \frac{1}{I} \sum_{\omega} \vec{E}_{\omega} \otimes \vec{E}_{\omega}^{\dagger} = \sum_{\omega} \frac{I_{\omega}}{I} \rho_{\omega}, \quad (17)$$

where we have supposed that the Fourier components are a discrete set, otherwise the summation should be replaced by an integral.

It happens that the spatial dynamics of photorefractive two-beam coupling are largely governed by the eigenvalues of the density matrix, more specifically by their difference. So we define the quantity:

$$\Lambda = (\lambda_1 - \lambda_2)/2, \quad (18)$$

where λ_1 is the larger of the two eigenvalues of the density matrix and λ_2 is the smaller one.

6.3.3 The transfer matrix

The evolution of the field vectors through the medium can simply be thought of as a transformation from input to output, or from input to any particular location z . We write:

$$\vec{E}(z) = T(z) \vec{E}(z=0). \quad (19)$$

Given the transfer matrix $T(z)$ we can calculate any other quantity needed, such as the field vectors or density matrix at any location z . Our analytical solution provides exactly this $T(z)$.

6.3.4 The Pauli matrices

The two-beam coupling interaction in this simple two-beam coupling case is described by the two-component field vectors and two-by-two matrices that transform them. An appropriate basis in which to decompose a general two-by-two matrix is provided by the Pauli matrices:

$$\sigma_1 = \begin{pmatrix} 0 & 1 \\ 1 & 0 \end{pmatrix}, \quad \sigma_2 = \begin{pmatrix} 0 & -i \\ i & 0 \end{pmatrix}, \quad \sigma_3 = \begin{pmatrix} 1 & 0 \\ 0 & -1 \end{pmatrix}. \quad (20)$$

These matrices each have the property that their square is equal to the identity matrix. For this reason it is also true that:

$$e^{i\psi\sigma_j} = \cos(\psi) + i \sin(\psi) \sigma_j \quad (21)$$

where the first term on the right-hand side is implicitly multiplied by the unit matrix.

6.3.5 Decomposition of the density matrix

The density matrix can be decomposed as a linear superposition of the unit matrix and the Pauli matrices, that is:

$$\rho = \frac{1}{2} + \sum_{i=1}^3 p_i \sigma_i, \quad (22)$$

where

$$p_i = \frac{1}{2} \text{Tr}\{\rho \sigma_i\}. \quad (23)$$

By the very definition of the density matrix, this first term never changes. When we consider ρ as a vector we may as well only write the three Pauli components and leave the unit component implicit. Therefore we can write:

$$\vec{\rho} = \begin{pmatrix} p_1 \\ p_2 \\ p_3 \end{pmatrix}. \quad (24)$$

A field vector can have complex components and therefore lies in a four-dimensional space, in general. By contrast, the components of the density vector are always real and therefore it lies in a three-dimensional space. We can furthermore rewrite the density matrix components in terms of spherical coordinates:

$$\begin{aligned} p_1 &= \Lambda \sin 2\theta \cos 2\Phi \\ p_2 &= \Lambda \sin 2\theta \sin 2\Phi \\ p_3 &= \Lambda \cos 2\theta \end{aligned} \quad (25)$$

where the radius is exactly the quantity previously defined:

$$\Lambda = \sqrt{p_1^2 + p_2^2 + p_3^2}. \quad (26)$$

Like the field vectors, the density matrix evolves through the medium. We designate the initial value of the density matrix as ρ_0 and similarly the initial values of the spherical components are θ_0 and Φ_0 .

6.3.6 Photorefractive coupling

We write the photorefractive two-beam coupling constant as a complex-valued constant Γ ,

$$\Gamma = |\Gamma| e^{i\gamma}. \quad (27)$$

The evolution equations describing the photorefractive effect always reveal the product $|\Gamma|z$. To simplify the appearance we measure the interaction distance z in units of the coupling strength, so its magnitude will no longer appear in the equations.

6.3.7 Analytical solution

With the above definitions in hand we can write the analytical solution for the transfer matrix:

$$T(z) = e^{i\beta(z)\sigma_1(z)} e^{-i\kappa(z)\sigma_3} e^{i\frac{\Delta}{2}\sin(\gamma)\sigma_{\rho 0}z}, \quad (28)$$

where the angles are:

$$\begin{aligned} \beta(z) &= -(\theta(z) - \theta_0) \\ \theta &= \arctan [e^{-\Lambda \cos(\gamma)z} \tan(\theta_0)] \\ \Phi &= \begin{cases} \Phi_0 + \ln \left[\left| \frac{\sin \theta_0}{\sin \theta} \right| \right] \tan \gamma - \frac{\Delta}{2} \sin(\gamma)z; & (\gamma = \pm\pi/2) \\ \Phi_0 \pm \frac{\Delta}{2} \cos(2\theta_0)z; & (\gamma = \pm\pi/2) \end{cases} \end{aligned}$$

and where

$$\sigma_1(z) = \sigma_2 e^{2i\Phi(z)\sigma_3}. \quad (29)$$

As mentioned earlier, this analytical solution has not been previously found in the literature. It is significant in that it provides a solution to a useful and interesting two-beam coupling problem.

6.3.8 Properties of two-beam coupling dynamics

The evolution of the optical electric field amplitudes as they propagate through the medium can be very complicated even for a relatively simple situation in which there are only two (temporal) Fourier components. In fact, it is because of this complexity that an analytical solution has not previously been found. However, the operator formulation, along with its geometrical interpretation, reveals the simplicity that underlies the merely apparent complexity of the dynamics. These simple dynamics are most readily depicted by the vector representation of the density matrix.

In this representation the density "vector" simply moves in a three dimensional space labeled by the Pauli matrix symbols (see Figure 38). The dynamics of the density vector are indeed always simple as can be seen in the following discussions of purely real ($\gamma = 0$), purely imaginary ($\gamma = \pm\pi/2$) and then complex coupling.

6.3.9 Real Coupling

For purely real-valued coupling the density matrix evolves in a plane defined by its initial value and the σ_3 axis. It always rotates towards the $+\sigma_3$ axis and, in the limit of a large interaction distance, it comes to lie along this axis. Figure 39 is an example of the density vector evolution -the solid line shows the path of the tip of the density vector. In this case, the density matrix is purely real, so its corresponding vector lies in the plane. No matter

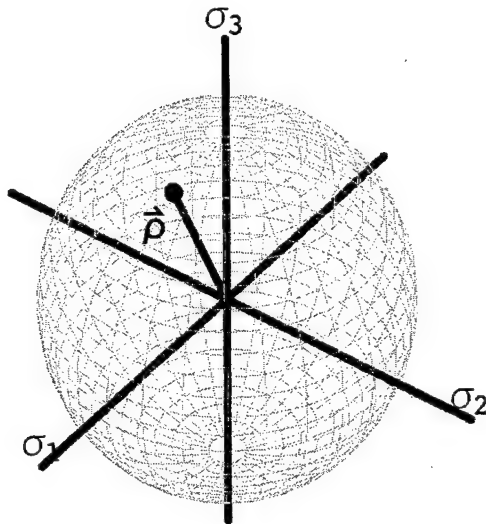


Figure 38: The density vector lies in a three dimensional space.

what it's initial condition, however, the trajectory always essentially looks like that in the figure.

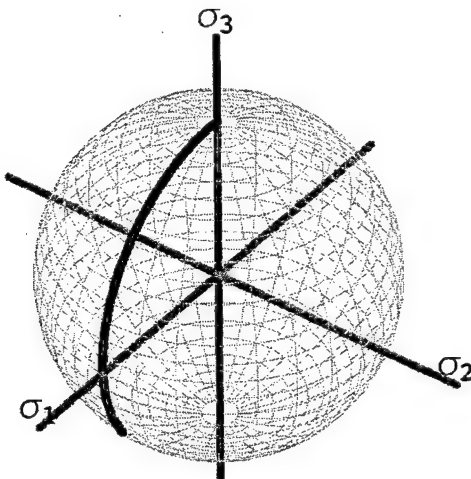


Figure 39: Dynamics of the density vector for real-valued coupling ($\sigma = 0$). In the limit of large interaction lengths the density vector becomes aligned with the $+\sigma_3$ axis.

6.3.10 Imaginary coupling

For imaginary-valued coupling the density vector again evolves in a plane, but in this instance the plane that is perpendicular to the plane defined by the initial density vector

and the σ_3 axis. Unlike the real-valued case, there is no asymptotic solution -the density vector continues to rotate about the σ_3 axis as it evolves with interaction distance. Figure 40 illustrates an example with the same initial conditions as for Figure 39.

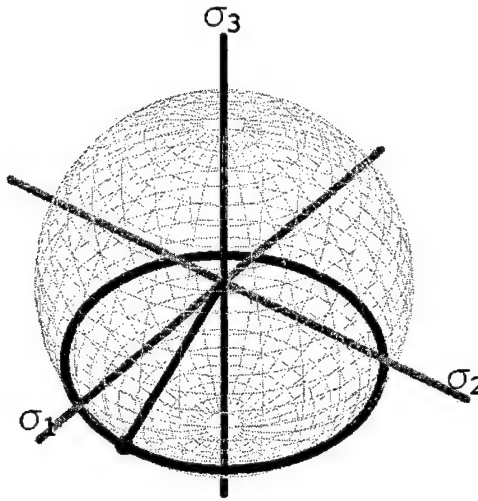


Figure 40: Evolution of the density vector for purely imaginary coupling ($\sigma = \pi/2$). The vector drawn from the origin indicates the initial value of the density vector. Rotation is counter clockwise as viewed from above.

The above considerations apply to the density vector. What about the field vectors? Their evolution can be cast in the same terms if we define individual density matrices for the various Fourier components:

$$\rho_\omega \equiv \frac{1}{I_\omega} \vec{E} \otimes \vec{E}_\omega^\dagger. \quad (30)$$

While the evolution of the total density vector is simple, the evolution of the individual components is not simple in general. Figure 41 shows a case in which there are two components. The evolution is clearly quite complicated. Yet these two components are indeed the same ones that gave rise to total density vector evolution shown in Figure 40.

6.3.11 Complex coupling

For complex-valued coupling coefficients the two in-plane motions combine into a motion that we refer to as the Damiao spiral. Figure 5a shows a case for which the initial density matrix lies almost along the $-\sigma_3$ axis. The imaginary portion of the coupling constant causes the density vector to rotate round the σ_3 axis while the real portion causes it to move toward the $+\sigma_3$ axis. As with purely real coupling, the density vector asymptotically approaches that axis at large interaction distances. Note that the direction of the rotation around the $+\sigma_3$ reverses as the density vector moves from below to above the (σ_1, σ_2) plane. For Figure

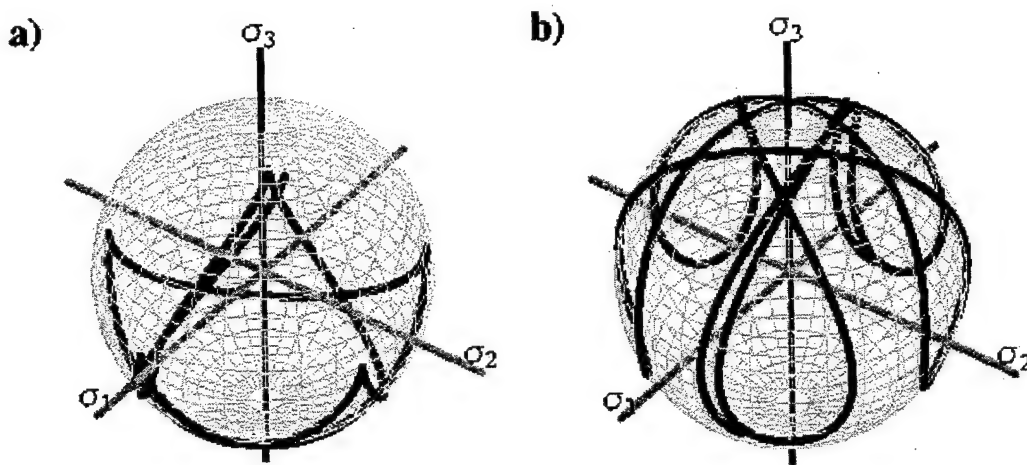


Figure 41: Evolution of the two component density vectors of the field vectors shown in Figure 40 for purely imaginary coupling.

42a a the imaginary portion of the coupling constant is large compared to the real part, while in Figure 42b the imaginary portion of the coupling constant is small.

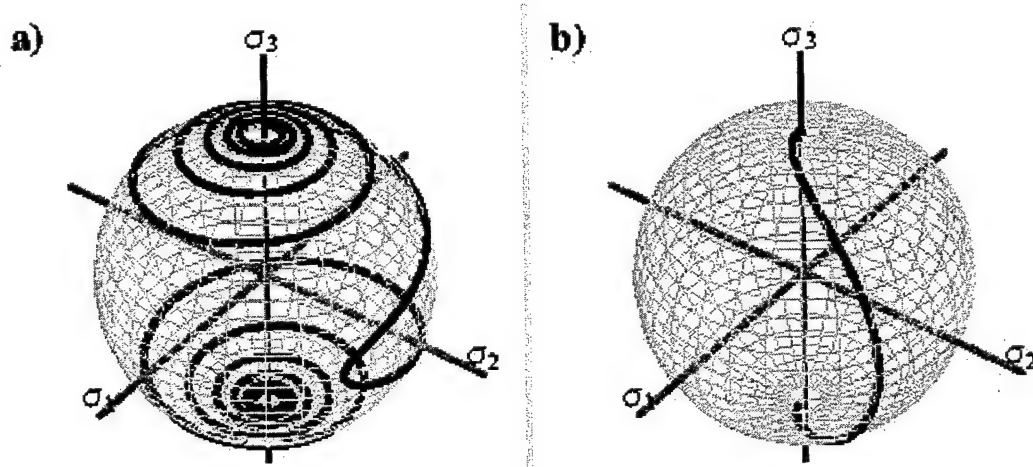


Figure 42: Damiao spirals executed by the density vector for complex-valued coupling. a). $\gamma = \pi/2 - 0.07$ b) $\gamma = -\pi/8$

While the evolution of the density vector is always the graceful Damiao spiral, the optical field amplitudes themselves can appear to evolve in a practically random manner. Figure 43a shows the density vector evolution for a case in which there are three field vector Fourier components. The evolution is very similar to Figure 42a. The density vector for one of the individual components is shown in Figure 43b -it is tangled mess!

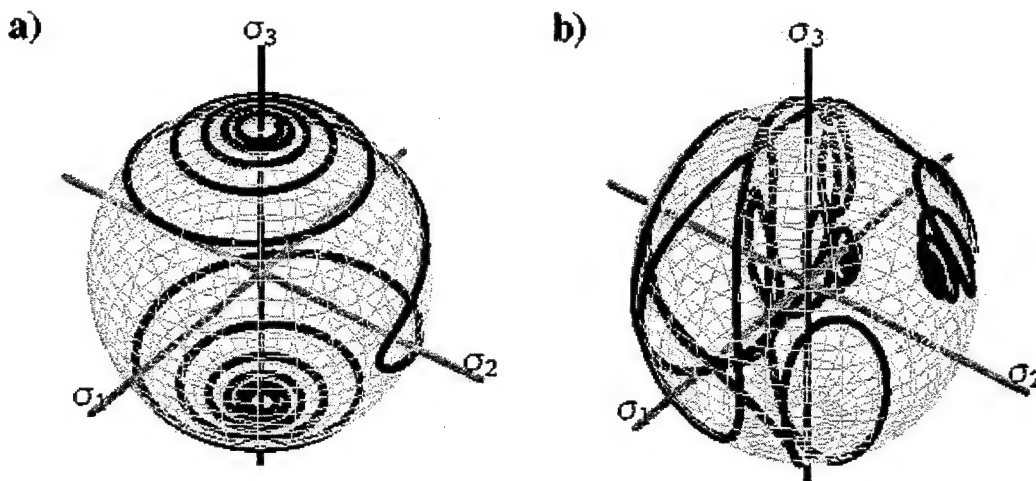


Figure 43: Evolution of the component density vectors: a) ρ_1 , b) ρ_2 . Each density vector has been normalized to unit length.

In retrospect it is remarkable that the curve is an analytical one and it is difficult to imagine it could have been obtained by the conventional coupled-mode approach to photorefractive two-beam coupling.

6.3.12 Remarks

It is useful to understand that the curves of the density vector shown in Figure 39 through Figure 43 represent unrealistically long interaction distances. In a real-life implementation the dynamics will execute only a portion of the Damiao spiral (or its two limiting versions). It is also useful to recall that it is nominally the coupling strength $|\Gamma|$ that governs the length scale. Yet so does Λ , i.e., half of the difference of density matrix eigenvalues. In general, as the number of independent (incoherent) Fourier field vector components increases, the smaller Λ becomes and the longer the physical length of the medium required to execute a given segment along the Damiao spiral.

Finally, it is generally true that the largest Fourier component dominates the dynamics, so that its density vector will closely resemble the total density vector evolution. It is the smaller ones that have the especially complicated dynamics: they do not strongly determine the dynamics. This happens because the available gain for a component is roughly determined by its power (i.e., square magnitude) relative to the total optical power. And since the gain plays its role in an exponent, the largest component dominates the dynamics and the smaller ones go along for the ride.

6.4 Theoretical considerations for the autotuning filter

This section summarizes the systematic approach to the filter's analysis and highlights the most relevant conclusions.

6.4.1 Theoretical analysis of the filter

The theoretical analysis of the reflexive-coupled photorefractive ring oscillator has two steps. The first consists of finding the possible steady-state solution for the oscillation of the ring given specific parameter values such as the gain and loss of the ring, and the relative intensities of the input beams. The second step consists of a stability analysis for each possible steady-state solution.

The stability analysis of the photorefractive feature extractor studied in the paper entitled "Stability analysis of two photorefractive circuits: the flip-flop and the feature extractor" demonstrates the first principal component extraction abilities of the auto-tuning filter. Two possible oscillation modes (one for each signal) that share a common gain medium model the feature extractor. The results of the perturbation analysis show that the only non-degenerate stable steady state is the oscillation of the stronger signal by itself in the ring. In the degenerate case of two equally intense signals the device is happy to oscillate with any linear combination of the two signals in each mode.

6.4.2 Design issues

The following discussion explores the design issues of the auto-tuning filter when only two signals are present at its input. The issues are similar for dealing with more than two signals, only more complex to present.

Ideally, the filter perfectly suppresses anything but the first principal component in the ring. Theoretically a simple ring (without a reflexive coupling unit) achieves this if the available small signal gain in the oscillator strictly equals twice the threshold gain for oscillation. This "strictly equal" is difficult to realize experimentally, hence the need for extra degrees of freedom supplied by the parameters of a reflexive ring. The filter offers four adjustable parameters:

1. the gain G_g of the two beam coupling in the gain unit
2. the round trip losses L due to absorptions and mirror reflectivities (they do not include the splitting from the BS)
3. the splitting ratio m of the reflexive coupling beams (the pump to weak beam ratio)
4. the gain G_r of the reflexive coupling.

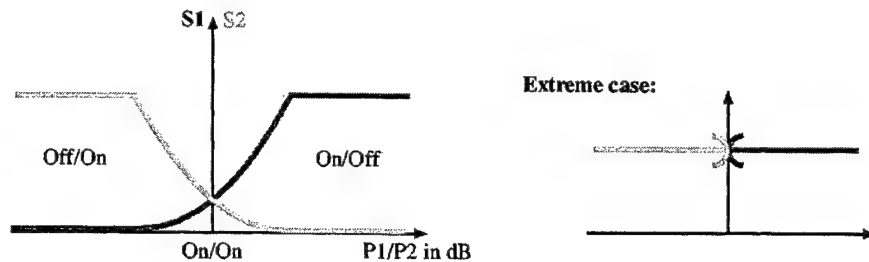


Figure 44: Generic plot of the oscillating signals S_1 and S_2 in the ring versus the input signal ratio P_1/P_2 in dB.

The filter's ability to suppress the weaker signal is best observed on the plot of the oscillating signals' intensity in the ring S_1 and S_2 versus the input signal ratio P_1/P_2 . Different points in the parameter space produce different types of plots. Figure 44 shows the plot type of interest in this discussion. Around a unity input ratio (0dB) both signals may oscillate in the ring (the on/on regime). Above some absolute boundary value of $P_1/P_2|dB$ only the stronger input signal oscillates in the ring (the on/off regime).

This section studies the parameters' influence on the P_1/P_2 boundary value of the on/on regime. A smaller boundary value means that the filter achieves a "perfect" first principle component extraction for input signal ratios closer to unity.

The boundary value of P_1/P_2 is indirectly obtained by observing the Log-Log plot of S_1/S_2 vs. P_1/P_2 : as the input signal ratio approaches the critical boundary value where the weaker signal disappears from the ring, the output signal ratio will tend to infinity. Since it is perfectly symmetric around the origin we observe the plot for $P_1 > P_2$ only.

6.4.3 Input signal ratio vs. the output signal ratio

The input signals to the filter P_1 and P_2 are supposed temporally and spatially orthogonal, i.e. they are the principle components of the input space. This statement implies that the signals allowed to oscillate in the ring will have the same temporal and spatial characteristics as the input signals. It also means that the available photorefractive gain for each signal is proportional to its relative intensity.

Assuming the plane wave approximation for the optical beams provides fairly simple formulas for the steady state values of the signals' intensities. Figure 45 defines the notations used in the following formulas.

The intensity of S_1 just after the gain unit is:

$$S'_1 = \frac{I_1 S_1}{P_1 \exp \left[-Gg \frac{I_1}{I_{tot}} \right] + S_1} \quad (31)$$

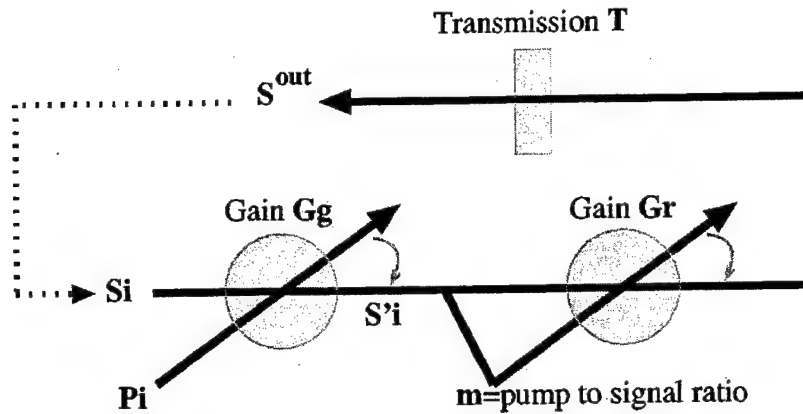


Figure 45: Notations for the signals' intensities at various points in the filter's open loop.

where $I_1 = S_1 + P_1$ and $I_{tot} = I_1 + I_2$.

The intensity of S_1 after the reflexive coupling and the ring's losses $L = 1 - T$ is:

$$S_1^{out} = T \frac{S'_1}{1 + m \exp \left[-Gr \frac{S'_1}{S'_1 + S'_2} \right]} \quad (32)$$

The loop gain G_1 for S_1 is then:

$$G_1(S_1, S_2) = \frac{T(S_1 + P_1)}{\left(P_1 \exp \left[-Gg \frac{I_1}{I_{tot}} \right] + S_1 \right) \left(1 + m \exp \left[-Gr \frac{1}{1 + \frac{(P_2 + S_2)S_2(P_1 \exp[-Gg I_1 / I_{tot}])}{(P_1 + S_1)S_1(P_2 \exp[-Gg I_2 / I_{tot}])}} \right] \right)} \quad (33)$$

These formulas are the same for intensity S_2 if the subscript 1 is replaced by 2 and vice versa.

For a signal to oscillate in steady state, its loop gain must be equal to unity. Given the parameters' values, P_1 , and P_2 , the values of S_1 and S_2 are obtained by solving the equations. For an input signal ratio close to unity these equations may yield up to three pairs of positive numbers. Figure 46 graphically represents such three solutions by the three intersections of the two gain curves. For this particular plot $P_1/P_2 = 1.05$ and the parameter values are $Gr = Gg = 10$, $m = 50$, $T = 0.5$. A dynamic study of the three solutions shows that the two extreme solutions are unstable in time and degenerate to only one signal oscillating in the ring, while the middle solution is robust under small perturbations. The stable solution moves to the bottom right of the space as the ratio P_1/P_2 is increased and eventually disappears when the on/off regime is reached.

Figure 47 illustrates a typical plot of S_1/S_2 vs. P_1/P_2 (the parameters' values are the same as in the previous example). In the region where both signals oscillate at the same

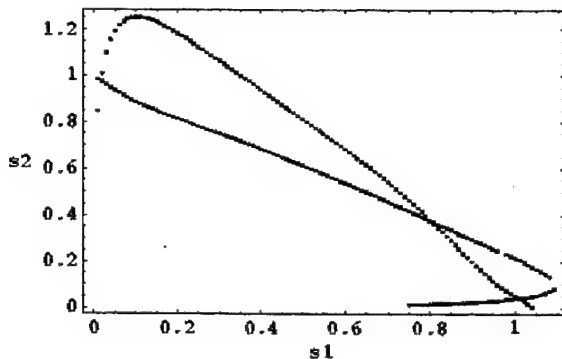


Figure 46: The intersections of the gain curves and , correspond to the steady state solutions for the two signals in the ring, with $P_1/P_2=1.05$ and the parameter values of $Gr=Gg=10$, $m=50$, $T=0.5$.

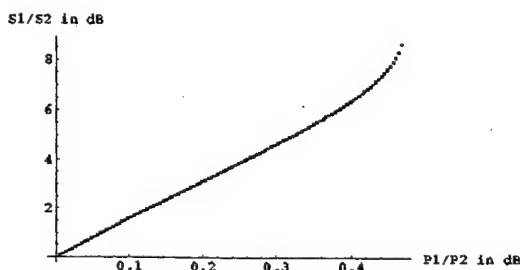


Figure 47: The Log-Log plot of the S_1/S_2 vs. P_1/P_2 curve shows a linear region when both signals are oscillating in the ring and a rapid increase toward infinity as the input signal ratio approaches the boundary value where the weaker signal disappears. The parameter values are $Gr=Gg=10$, $m=50$ and $T=0.5$.

time the curve is mostly linear. Close to the critical P_1/P_2 value where S_2 disappears from the ring, the curve rapidly tends to infinity. In general, the smaller this critical value, the steeper the slope of the linear region. The slope is a direct evaluation of the competition between the signals in the auto-tuning filter.

6.4.4 Influence of the ring's parameters on the signal competition

This section qualitatively describes the effect of the filter's parameters on the critical value of the input signal ratio above which the filter performs a theoretically perfect first principle component extraction.

The gain Gg provided by the crystal coupling the input beam to the ring essentially serves

to compensate for the losses encountered by the signals in the ring. As mentioned before, photorefractive gain is shared among the signals proportionally to their relative intensities. On one hand, to ensure that there is always a signal oscillating in the ring the minimum available gain must be above twice the threshold gain for oscillation: when the two signals are exactly equal they are both allowed to oscillate. On the other hand, a very high available gain means both signals' gains are above threshold for a wide range of input signal ratio values: both principal components may oscillate. A smaller available gain G_g is therefore preferable as long as it stays greater than twice the threshold gain.

The passive losses of the filter are embodied by the intensity transmission coefficient T . This transmission coefficient, being the same for all signals trying to oscillate, does not help the competition between the signals. Lowering T is not equivalent to decreasing the gain G_g from a signal competition point of view, it actually hinders the competition. The critical input signal ratio decreases as the transmission T increases.

The splitting ratio m determines how much power is taken out of the ring and coupled back to it through photorefractive two beam coupling. This reflexive coupling process is effectively a selective loss element: the weaker signal undergoes higher losses than the stronger. Increasing the parameter m gives more importance to the signal competition and therefore lowers the critical input signal ratio. Increasing the splitting ratio m however also imposes more difficult self starting conditions on the filter.

The optimal value of the reflexive coupling's gain G_r strongly depends on m and weakly on the other two parameters of the system. On one hand coupling back to the ring with too little gain increases the overall losses of the filter and lets the two beam coupling at the input gain unit govern the dynamics of the filter. Coupling back to the ring with too much gain on the other hand, dampens the selectiveness of the reflexive coupling. The optimal value of G_r increases for increasing values of m .

6.5 Optically Smart Antenna System Tests

6.5.1 Introduction

The optical circuitry of the system adaptively extracts the principal component of the received signal space, that is, the strongest second-order independent temporal component of the ensemble of received signals. The adaptive receiver system can be used, for example, to mitigate multi-path interference effects, and can separate one received signal from another even though their power spectra may entirely overlap. The system currently accommodates two incoming signals, yet the optical portion remains essentially unchanged as the number of independent signals, i.e., users, increases. The system consumes less than 50 watts CW. To place this work in some context we recall the salient features of the system.

A block diagram of the adaptive receiver system has been shown in Figure 37, for the case of two incident signals each of which is on the microwave carrier. The front end consists of a 30-element 10-GHz constrained lens antenna array with active antenna receivers positioned along the H-plane focal arc of the lens. Each receiver position corresponds to a specific direction of a plane wave incident and received by the lens array. Upon down-conversion, the IF signals are imposed as phase modulation (PM) sidebands onto an optical carrier using electro-optic modulation. The optical carrier is then suppressed using an adaptive holographic element, leaving the signal-bearing optical sidebands. The modulated carrier-suppressed optical beams are coupled into the adaptive optical circuit, referred to as an "auto-tuning filter", that separates the two principal components of the signal input space. The outputs of the prototype adaptive antenna are baseband signals dynamically ordered by signal strength.

6.5.2 End-to-End Characterization of the Prototype

Here we provide a qualitative description as a context in which to present the quantitative measurements given below.

In general one usually wishes to extract one or more of the originally transmitted source signals in the face of multi-path and other interference effects. The outputs of our two-channel system do not, in general, recover the original source signals. Rather, the output of the adaptive processor always provides the principal components of the signal space. The principal components are proportional to the two transmitted signals if and only if three conditions are satisfied: 1) the sources are independent, 2) they produce different received powers and (3) the signals incident on the optical processor correspond to spatially orthogonal signals. Condition 1 is always satisfied in practice unless some spurious effect causes an apparent correlation (such as the presence of the optical carrier, in our case). The limits imposed on our system by condition 2 are already revealed by the signal extraction curve of the autotuning filter, which shows a finite slope through the origin as shown in the previous annual report. This requirement reflects a fundamental limitation of principal component analysis. In principle, condition 2 could be relaxed with a more sophisticated optical circuit capable of higher-order (than correlation) signal processing. The fact, though, is that this requirement is usually satisfied in practice. Condition 3 is another matter. It reflects a particular limitation of our holographic circuit that could be relaxed with a different but more complicated optical circuit geometry. As it stands, condition 2 is the most confining one and is the focus of the end-to-end characterization of the system.

Qualitatively, one expects that the principal components will become more and more a superposition of the two source signals as the transmitters are moved close together in angular space (the receivers' positions are fixed). When they are at the same angular position, there

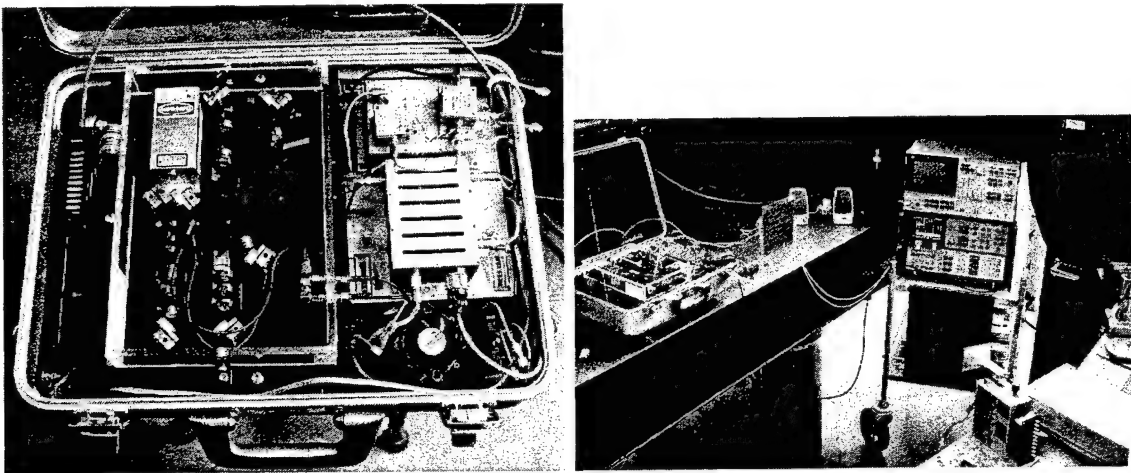


Figure 48: (a) The adaptive receiver system packaged in an aluminum 113x18x6inch briefcase. (b) Antenna system measurement arrangement with one transmitter shown in the front-right and another partially shown in the center-right. The antenna array and packaged processing system may be seen on the table on the left.

is nothing available to the optical processor to distinguish one source from two sources.

Figure 48a is a photograph of the adaptive antenna processing system. The system is packaged in an aluminum briefcase with a single power plug. The electronic portions of the system sit on the right side of the case, while the optical portion sits to the left of center. The laser power supply is visible at the far left, while the other power supplies, as well as two cooling fans, lie above the electronics. Figure 48b shows the system as it has been tested end-to-end. The processor sits towards the left and rear of the photograph, with the antenna lens array sitting just to its right. On the lower right is a transmitter with a horn antenna, and a second transmitter is partially visible on the far right and vertical middle of the photograph. The two transmitters are placed symmetrically about the antenna array bore-site.

We assessed the performance of the system by taking signal extraction curves reminiscent of the enhancement of the autotuning filter (see the previous annual report) for three different angles between the two transmitters. Figure 49 provides a context in which to describe the measurements. In general, each of the two detector outputs will be composed of a linear superposition of the transmitter signals. Since the transmitted signals are uncorrelated, one can write:

$$\begin{aligned} R_1 &= R_{11} + R_{12} \\ R_2 &= R_{21} + R_{22} \end{aligned} \tag{34}$$

where R_{jk} is the received signal power from transmitter T_k after down-conversion to the IF. With a large angle between the transmitters, the received power R_1 at the IF on one channel

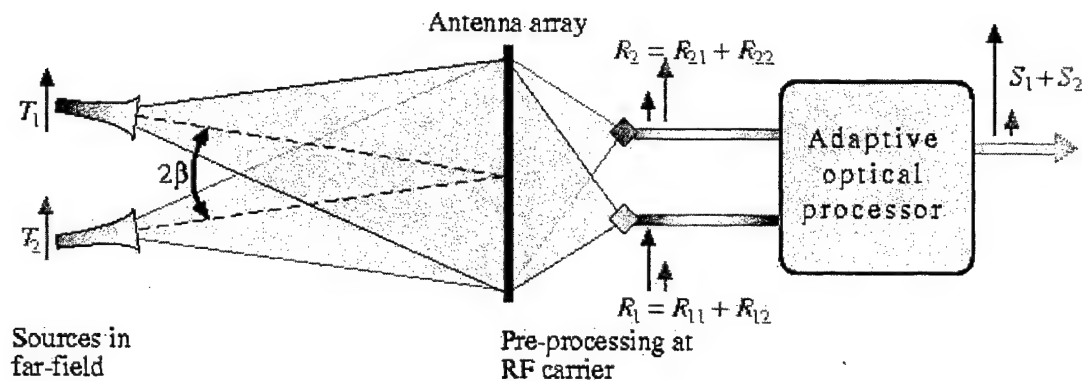


Figure 49: Schematic defining the context of the end-to-end system measurements.

of the receiver is primarily from transmitter T_1 while the received power R_2 at the other channel is primarily from transmitter T_2 . In other words, for equal transmitted powers R_{12} and R_{21} are small compared to R_{11} and R_{22} . We measure a "cross talk" between receiving channels by setting the transmitter so that the received powers R_{11} and R_{22} are equal and then determine $C_j = R_{jk}/R_{jj}(i \neq k)$. From the symmetry of our experimental arrangement, we expect the two values of cross talk to be the same, $C_1 \approx C_2 \equiv C$. Table 8 shows this cross talk C for each of three angles. At the largest angle of 48 deg between the transmitters the cross talk is $-15dB$. At the smallest angle of 20 deg it is $0dB$.

In order to keep the presentation of the quantitative data relatively simple, we define a single input signal power ratio, R_{11}/R_{22} . At the output, the autotuning filter provides the principal components of its input signals. In this experiment, we optically detect only the power from Output 1 which provides the higher power of the two principal components. We define a single output power ratio S_1/S_2 , the ratio of detected power corresponding to transmitter T_1 to the power corresponding to transmitter T_2 . Ideally this output ratio would be zero or infinity, depending on which signal was larger, that received from T_1 or that received from T_2 but otherwise independent of the input ratio. Figure 50 plots the output signal ratio versus the input ratio for three different angles between the transmitters. The two curves for the larger angles have a characteristic "S" shape. When the received signals have identical powers they are indistinguishable by the autotuning filter (this is because the two eigenvalues of the signal correlation matrix are degenerate). However, even a small power difference can provide the needed distinction. Of particular interest therefore is the slope near the origin of the curve. For the largest angle of incidence it is $76dB/dB$. This means that if the signals differ by $0.04dB$ at the input to the autotuning filter, their ratio is enhanced to about $3dB$ at the output. Once the output ratio is above $10dB$ or so, the

Angle between transmitters (α) (degrees)	Receiver cross talk (dB)	Maximum slope enhancement (dB/dB)
48	-15	76
35	-10	6.1
20	0	1.3

Table 8: Crosstalk and enhancement slope of the antenna system for three different angles between the transmitters in the far-field.

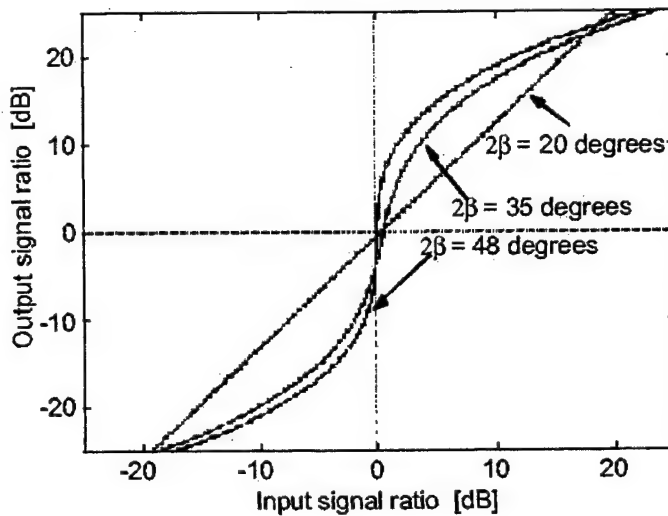


Figure 50: Signal extraction properties of the adaptive system parameterized by the mutual angle between the transmitters.

enhancement begins to level off. With the smaller angle between the transmitters of 35 deg the "S" curve becomes much shallower. The slope at the origin is $6.1\text{dB}/\text{dB}$. At an angle of 20 deg the "enhancement" is small. At the origin it is about $1.3\text{dB}/\text{dB}$.

At this latter angle we note that the cross talk is 0dB , meaning that all four IF powers R_{jk} are about the same size for equal transmitted powers. It would seem for this smallest angle that the two transmitters are unresolved by the antenna and therefore their two signals should be indistinguishable from one. However, the analysis in terms of power omits the important role of the signal phase and this is the reason there is still some observed signal contrast enhancement, however small.

6.5.3 Discussion

A number of remarks are in order concerning this prototype demonstration and the potential role of adaptive optical processing in wireless communications. The adaptive processing in the prototype developed in this work is performed by a relatively simple optical circuit. The inherent function of this circuit is principal component extraction, and it has been effectively demonstrated. It is useful to note that the role of the antenna lens array in our system design is more subtle than might first be apparent. It is true that the array performs something akin to a spatial Fourier transform on the signal space; roughly speaking it converts an angle of arrival to a spatial region in the focal surface. In this sense it does some preprocessing of the incoming signals. If the incoming signals are known to have well-defined and distinguishable directions, the adaptive processor is unnecessary. The focal-surface detectors already contain well-separated signals. That does not help in cases of multi-path and other forms of interference, however. In principle it makes no difference to the auto-tuning filter whether or not this "Fourier" transformation of the signals takes place. The actual practical benefit of the antenna lens array enters through dynamic range considerations: In a typical communications scenario one can expect the power incident on the antenna lens array to be more or less uniform over the array, while the power at the focal surface varies by a larger amount. Consider two angularly well-separated sources for example, one giving rise to a received power of 1 W, and the second giving rise to a received power of 0.1 W. At the array, each antenna element receives the same power of $1.1/N$ watts, where N is the number of array elements. At the focal surface, one detector receives 1.0 W while the second receives 0.1 W. One can clearly amplify the signal from the second detector so that the output power from the front end is the same for both signals. This could not be done were the signals taken directly at the antenna array. Such dynamic range considerations tend to remain valid when the signals are subject to a multi-path environment. Our prototype demonstration is designed for processing two signals. Among the major benefits of the optical processing is its scaling characteristics. A larger input signal space, say of size N , can be accommodated merely by increasing the number of electrodes on the electro-optic modulator to N -the autotuning filter remains largely unchanged. Increasing the number of output channels from 2 to M , requires a total of $(M-1)$ autotuning filters. Thus in general the adaptive processor scales linearly with the size of the desired signal space, rather than quadratically, as is often the case with adaptive electronic processors. The system will optimally process multi-path communication signals provided arrival time differences are negligible compared to the inverse bandwidth of the signal. Different paths are received by different focal surface receivers. Automatic gain control normalizes the received signal strengths to the same level and the autotuning filter combines the received signals coherently while the noise from different receivers adds incoherently. When the multi-path delay times

are much greater than the inverse signal bandwidth, the autotuning filter treats each as a separate source and extracts the strongest one. The prototype demonstrated here processes signals with bandwidths in the 100 MHz range. None of the components are however limited to this bandwidth. Broadband antennas, such as second resonant slots with up to 20 carrier frequency, allowing for several gigahertz IF frequencies. A possible issue in this case may be the angle-of-arrival detection quality due to higher grating lobes at the lower band edge, which is a design parameter. The electro-optic modulator presented here is effectively a lumped-element circuit, but its architecture accommodates a set of N coupled traveling wave transmission lines, and such an EO modulator can cover several gigahertz of bandwidth with good modulation efficiency. In summary, this section of the report describes the progress on the smart antenna array with optical adaptive processing. The array operates at a 10 GHz RF carrier and a 125 MHz IF signal. The input wave is an unknown superposition of a number of uncorrelated signals incident from different directions and with possibly changing spatial and temporal characteristics. The output electrical signals are adaptively separated and ordered according to their respective signal strengths. This functionality is accomplished with a compact holographic optical processor, which is completely internal to the system. The processor and associated electronics is packaged in a standard-size aluminum briefcase with a single external power plug, and consumes less than 50 W of CW power.

6.6 Progress evaluation

Our goals for this year as stated in last year's report were:

- integrate the entire RF optical system from the antenna receiver array to the output of the optical processor, including the laser, into a single portable system
- asses the signal extraction performance of the system using a pair of uncorrelated transmitters
- increase the number of RF channels processed by the optical system to seven
- increase the bandwidth of the EO modulator to 0.5GHz

The entire system has been integrated in a portable 13x18x6 inch brief case (see Figure 48). The system has shown its robustness traveling round-trip to Chicago as well as round-trip to Florida and arriving at destination always in working order. The signal extraction performance of the system was evaluated and this report presented the results.

The number of channels of the prototype system has not yet been increased for two reasons: one, the redesigning of the electronics and of the optics to be integrated in the briefcase took more time than had been planned for, and two, increasing the optical power

without significantly increasing the size of the system is a non trivial problem. We judged that the latter problem had priority over increasing the EO bandwidth: EO technology for 0.5GHz exists and therefore we do not foresee any major impediments for the day we will want to build one.

6.7 Plans for year 5

We believe that the key to solving our optical power problems is using laser diodes as sources and using laser diode amplifiers to boost the optical beams' powers. Our current photorefractive material is pure barium titanate (BaTiO_3) which works best for green wavelengths (i.e. gives a maximum intrinsic photorefractive gain). The same material appropriately doped with rhodium produces good results with red laser beams. Red laser diodes (and so indirectly amplifiers) are common industry products. The coming year we plan to research ways to incorporate these laser diode sources and amplifiers in our optical system's design. This research will in the long run also allow the development of more complex, power hungry optical circuits.

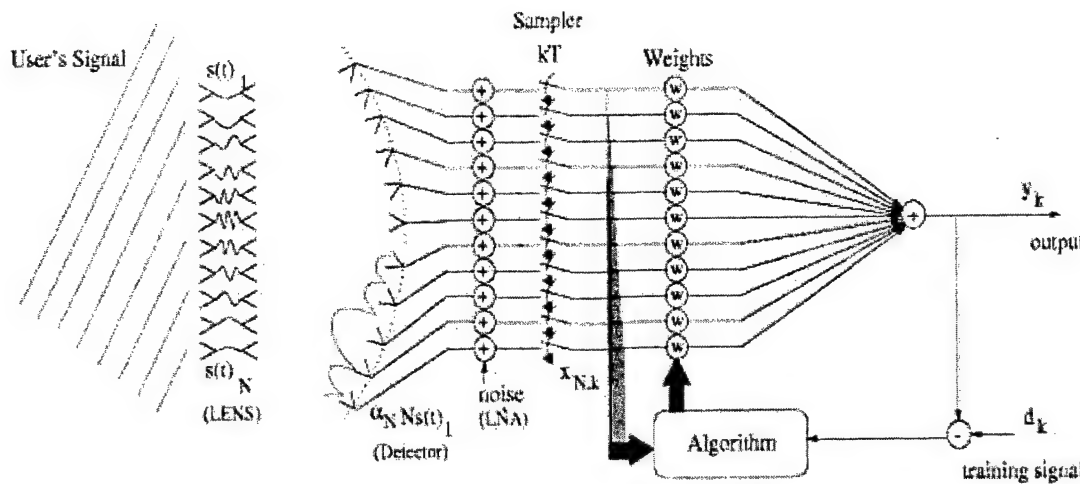


Figure 51: Schematic of an adaptive antenna array.

7 Quasi-optical Antennas for Optical Processing Front Ends

7.1 Smart Lens Array Antennas for RF-optical Front Ends

In the previous report, we described an optically-switched full-duplex transmit-receive lens antenna array. The details of the design of the optically-controlled switch, single array element and entire 27-element array were presented. In this report we discuss another aspect of such quasi-optical lens arrays: preprocessing of the signal at the analog front end. This is important in the context of adaptive (smart) arrays.

Smart (adaptive) antenna arrays are usually thought of in terms of the block diagram shown in Fig. 51. An antenna array receives a number of signals modulated onto carriers, and the receiver front end down-converts received signals that are then sampled and processed using DSP algorithms.²⁰ The purpose of the algorithm is to change the complex weights (phase and amplitude) of the signals associated with each antenna element in the array, thus performing beamforming of the received radiation pattern. A standard antenna array consists of N elements, each possibly containing a LNA, followed by a feed network. In this paper, we investigate the use of a lens antenna array, in which N array elements perform a

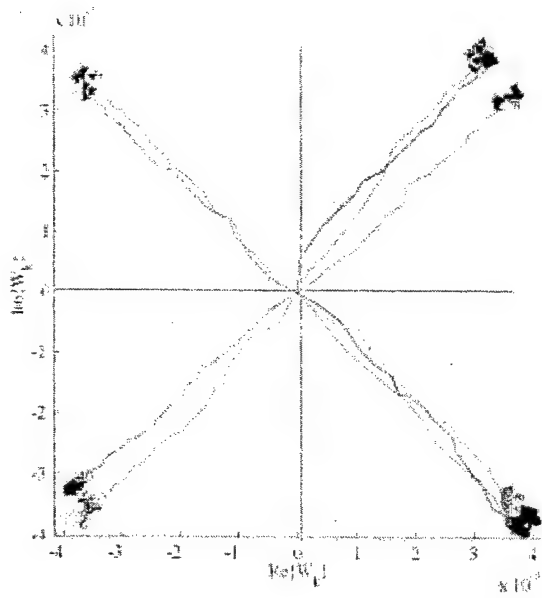


Figure 52: Weights in the complex plane for a 12-element linear array adapted to point the main beam in the +30-degree direction.

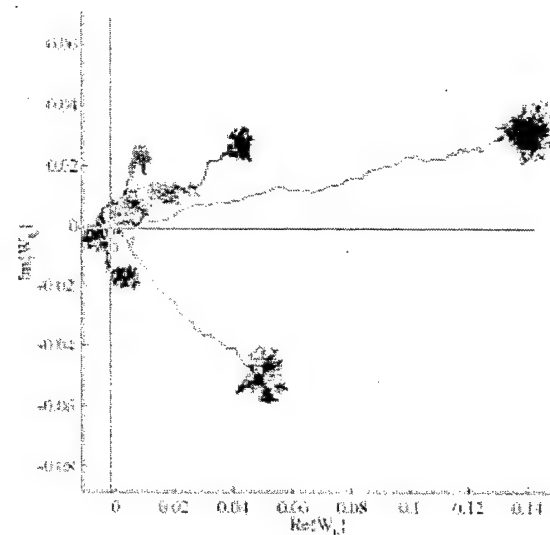


Figure 53: Weights in the complex plane for a 13-receiver element lens array adapted to point the main beam in the +30-degree direction.

Fourier transform operation on the incoming wave, and $M \leq N$ receivers are placed on a focal surface sampling this image. The lens array can include integrated amplifiers in each element, and was shown to reduce multipath fading effects due to built-in angle diversity at X and Ka bands.²² A lens array was also successfully integrated with an analog holographic optical processor in an optically-smart antenna array.²³ This smart antenna demonstrated adaptive signal ordering by strength in a multi-signal space. Here we present design of lens arrays for smart antenna systems with digital signal processing, simulations of adaptive algorithm complex weights and SNR, as well as adaptive beamforming radiation patterns for cases of multi-user and multi-path communication scenarios.

As an example of the motivation to use lens arrays in the place of more standard antenna arrays, the least mean square (LMS) algorithm was applied to 12-element linear array. The resulting optimal (Wiener) solution for the complex weights associated with each antenna element is shown in Fig. 52. The weights all lie on a circle, and as the antenna adapts to, e.g., null an interfering user, the weights rotate in the complex plane. The simulation was then performed for an 12-element lens array with 13 receivers, and the resulting complex weight adaptation is shown in Fig. 53. It is clear that the two analog front ends result in entirely

different optimal solutions for the complex weights. In the standard array, the weights are distributed on a circle, and all are equally important in adapted pattern synthesis. On the other hand, in the lens array, only a few of the weights are significantly larger than 0 after adaptation, so fewer elements (receivers) in the lens can be used for beamforming (only 3, #10, #11 and #12 in the example in Fig. 53). The lens, by doing a Fourier transform of the incoming wave, performs a portion of the processing and reduces the computational load of the smart antenna system.

A lens array consists of two antenna arrays connected with transmission lines of varying electrical length, and is similar to a Rotman lens. For example, in the experimental cylindrical X-band lens described in detail in the previous year's report, the patch antennas are connected with similar patches on the other side of the multi-layer substrate. The delay lines enable focusing of a received wave onto a focal surface, where receive antennas and circuitry is placed. The field distribution (image) on the focal surface is the Fourier transform of the original incident field, Nyquist-sampled by the lens.

A sketch of a lens array with a 6λ diameter and focal length to diameter ratio of $F/D=1$ is shown in Fig. 54. The focal surface field amplitude profile for a single source at 20 degrees off the optical axis is shown in Fig. 55. The crosses represent the possible positions of 121 receivers that sample the received field distribution. In this simulation, patch antennas with a half-wavelength spacing are used and the image is found using EM wave propagation, details are given in Jim Vian's thesis dissertation.

The received amplitude at the 121 receivers can be ordered in power to show the relative received powers, Fig. 56. The LMS algorithm is then applied to the received sampled signals, with noise added by the receiver taken into account. The SNR was then simulated for lenses of different sizes, and the result of these simulations is shown in Fig. 57 as the number of significant receivers is increased. The arrow indicates the result for the lens from Fig. 54. It can be concluded from this simulation that approximately the 10 receivers that receive most of the signal power in this 121 element array need to be taken into account to approach the optimal SNR. The same conclusion is valid for larger lenses.

The performance of the lens is evaluated in a multi-user environment with a "desired" user at 30 degrees, while another user that is a potential interferer approaches from -40 degrees, to 0, 20 degrees and finally is as close as 5 degrees from the desired user in the E plane. When the LMS algorithm is applied to the 121-element lens, the resulting adapted radiated E-plane patterns are calculated as shown in Fig. 58. Similar results can be calculated for multipath scenarios. The main conclusion at this point of the research is that, as expected, analog beamforming at the front end eases the computational burden on the signal processing for non-optimal (non-Wiener) solutions.

Our plan in the last year is to evaluate lens performance for other than LMS algorithms

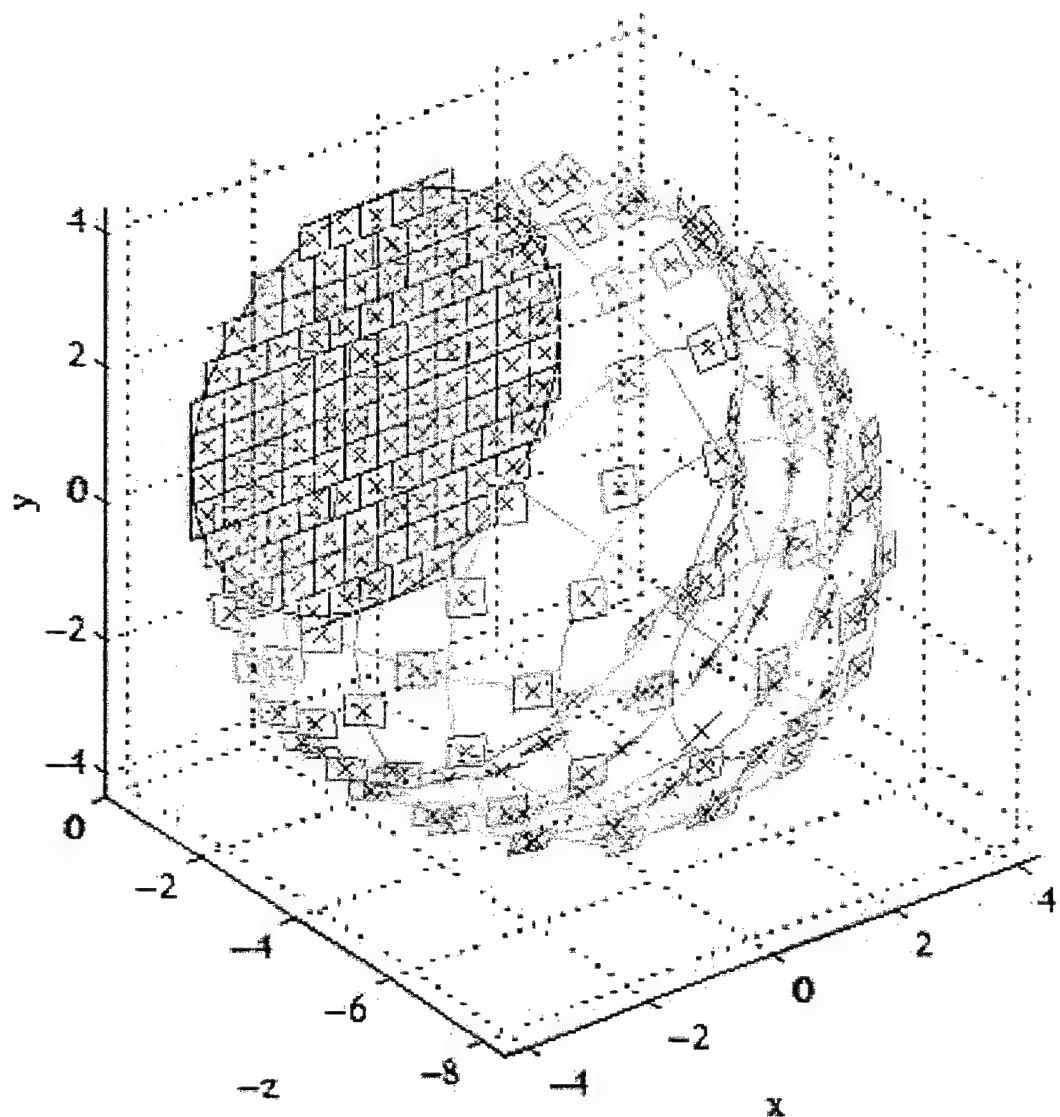


Figure 54: Sketch of a 121 lens antenna array used in the simulations. 121 receivers are positioned on the focal surface of the lens, which has an F/D=1.

and quantify computational load savings. We also plan to investigate the best place to integrate LNAs in the lens/receiver array scenario for different constraints (applications).

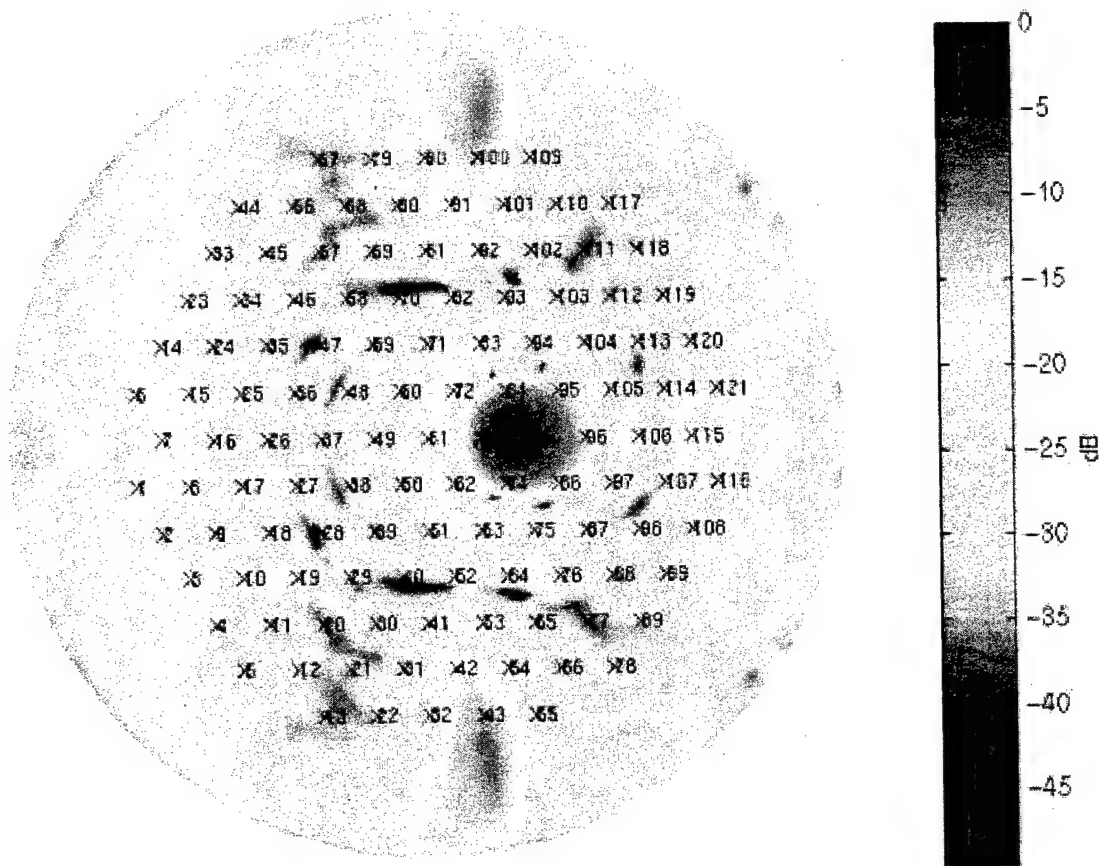


Figure 55: Nyquist-sampled image of the 121-element lens array for a wave incident from +20 degrees off boresite.

7.2 Feasibility study: QO lens arrays for passive millimeter-wave ranging

During Year 4 of this project, we have looked into an approach to millimeter-wave passive ranging using a method that has been demonstrated in the visible range. Ranging is achieved for multiple objects by way of a receiving discrete lens with modulated amplitude and/or phase response. The result is a set of image patterns with orthogonally coded, range dependent spatial frequency content. We performed simulations for a relatively small (100-element) discrete lens antenna array with a cosinusoidal amplitude mask and half-wavelength period at 94 GHz. The feasibility of the approach along with comparisons to the optical counterpart are discussed next.

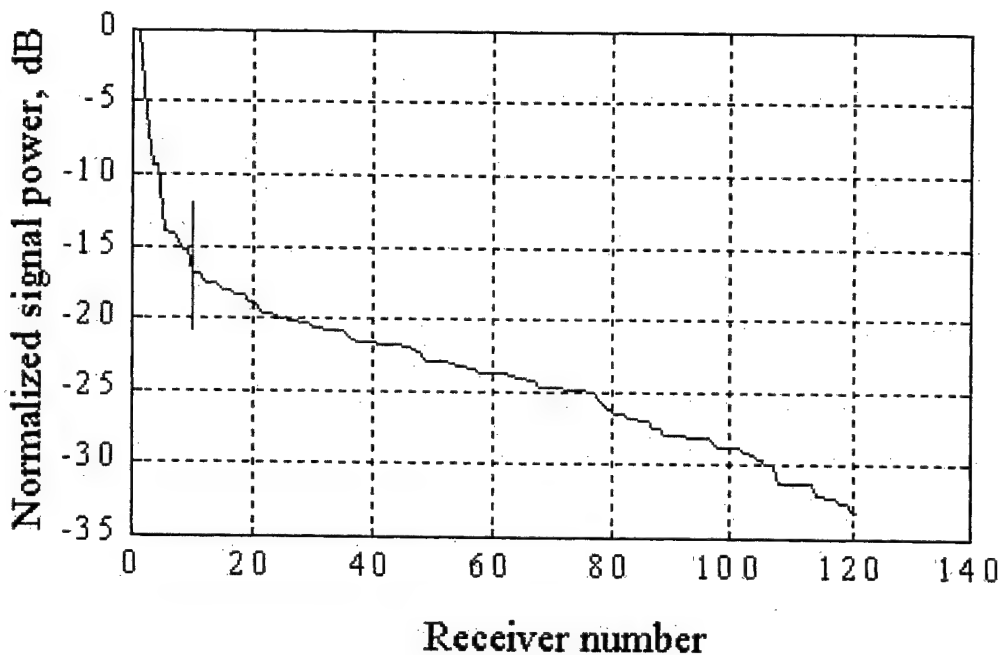


Figure 56: Distribution of power received by the receivers sampling the image of the 121-element lens array, rank order normalized.

Millimeter-wave ranging is of interest since most metal objects have high black-body emission in this range and there is also a low-attenuation window in the atmosphere absorption curve around 94 GHz. Waves in this frequency range penetrate through dust, fog and smoke and are therefore of interest to the military. Some ranging systems around 90 GHz have been demonstrated, primarily by TRW, but they involve transmission and are therefore easily detectable. A review of passive millimeter-wave ranging is presented in.²⁴

In the optical domain, a number of different ranging techniques are used. Recently, a technique referred to as *wave-front coding* as described in Fig. 59 was implemented for microscopy applications.²⁵ A standard lens images an object situated on the optical axis onto a focal point. If however a mask is used in front of the lens, as shown in Fig. 59, the range can be determined theoretically from the magnitude of the transfer function obtained by convolution of the phase front with the pupil function of the aperture. In the optical system the image is sampled with a CCD array and the spatial frequency content of the image is Fourier-analyzed using digital signal processing. The Fourier transform of the image will contain peaks that move out to the higher-order spatial modes as the range of the

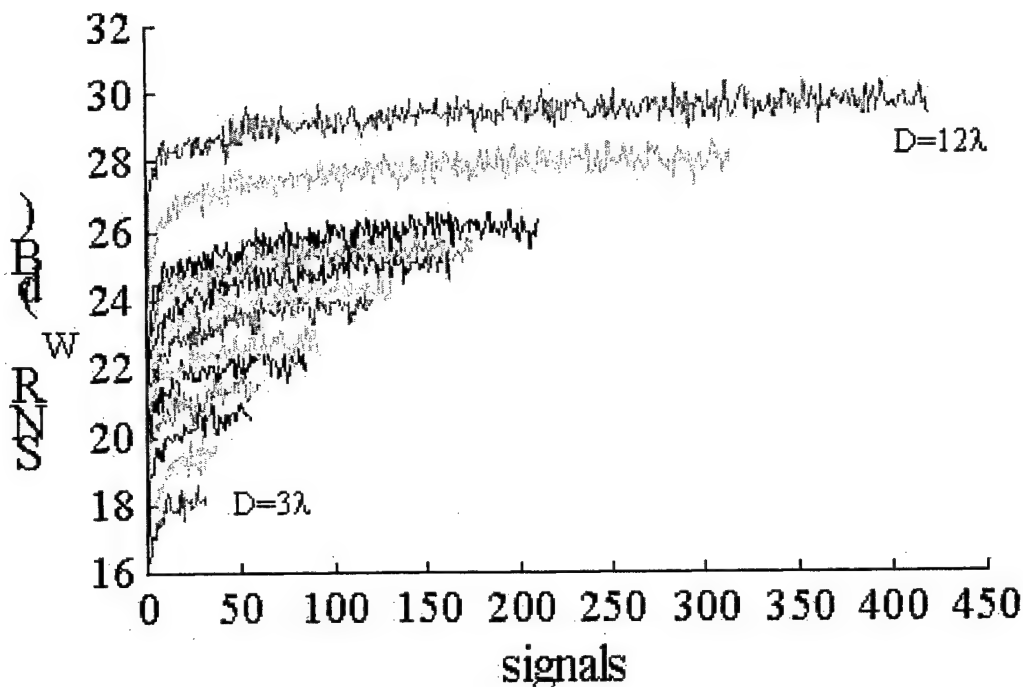


Figure 57: Signal to noise ratio (SNR) as a function of lens array size and number of receiver signals used in the LMS algorithm calculations. The 121-element lens used as the case study example is indicated with the arrow.

object increases. Peaks in measured spatial frequency are then correlated with a calculated magnitude of the transfer function in order to calibrate the range of the object.

We were interested in examining the applicability of this approach to longer wavelengths in the millimeter-wave region, e.g. at 94 GHz. We specifically use a discrete lens (a multi-beam antenna array) that can include the functions of the lens and mask in the optical system from Fig. 59. In addition, the variety of possible masks is much larger than in an optical system, and there is a possibility of adding gain into the lens as amplifiers in W-band have been demonstrated by a number of groups in the past decade.^{26–28} The millimeter-wave implementation of the optical setup from Fig. 59 includes a lens antenna array in which the delay and gain (and/or attenuation) in each element is modified from a more standard constrained lens to that corresponding to a lens with a mask. This is demonstrated schematically in Fig. 60.

At the object side of the lens array, each antenna element samples the incident wavefront. Since the antennas are spaced by a half free-space wavelength, the sampling of the wavefront

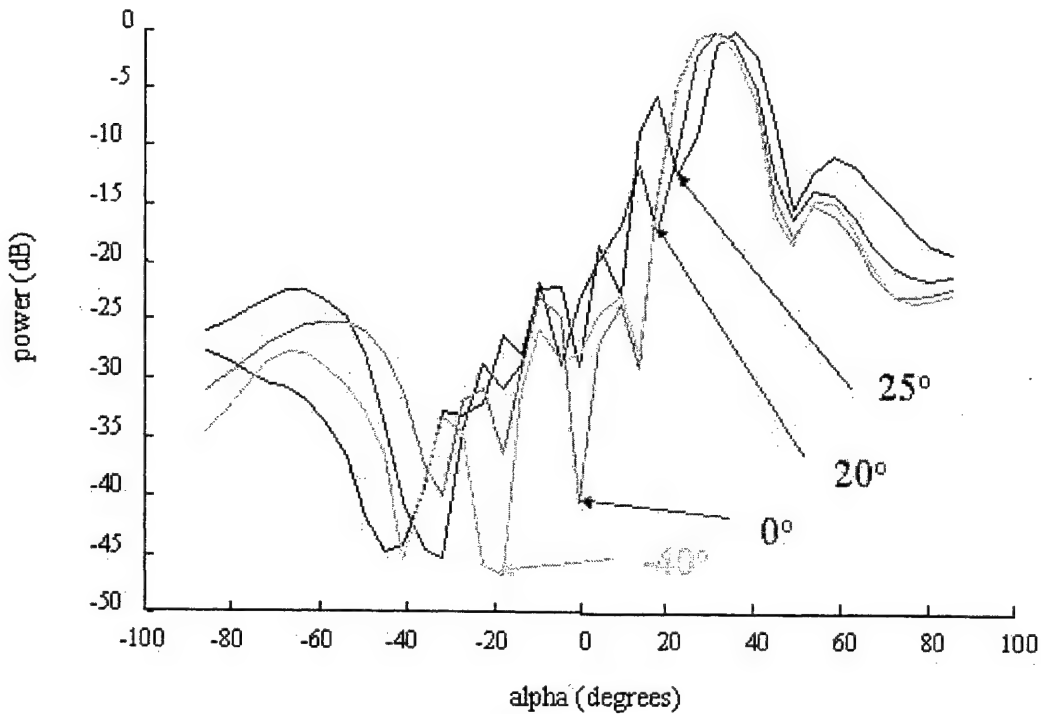


Figure 58: Adapted E-plane radiation patterns of the 121-element lens array for a desired source at 30 degrees off boresite, and an interferer moving in from -40 degrees, to 0, 20 and 25 degrees off boresight. The patterns were obtained by adapting only 10 of the 121 elements of the lens receiver array.

at bore-sight (direction of the optical axis) is Nyquist sampling. Each element introduces a delay and possibly an amplitude change before being re-radiated by the image-side antennas. Instead of a CCD array in this configuration, an array of antennas with detectors is placed on an imaging surface. The detectors can be designed to under-sample, Nyquist-sample or over-sample the image, depending on other requirements. Details on previous work in lens antenna arrays at X through Ka-bands (10 to 30 GHz) relevant to this work can be found in.^{22, 29, 30}

In order to gain some insight into the applicability of wave-front coding to millimeter-wave ranging, a very small 94 GHz array was simulated using an in-house developed electromagnetic simulator used also in.²⁹ The array is small compared to a directly scaled version of the optical system, which would be on the order of 10,000 free-space wavelengths across and would make it impractical to implement (30 m diameter).

Here, the modelled array is 5 free-space wavelengths across (100 elements, about 2 cm

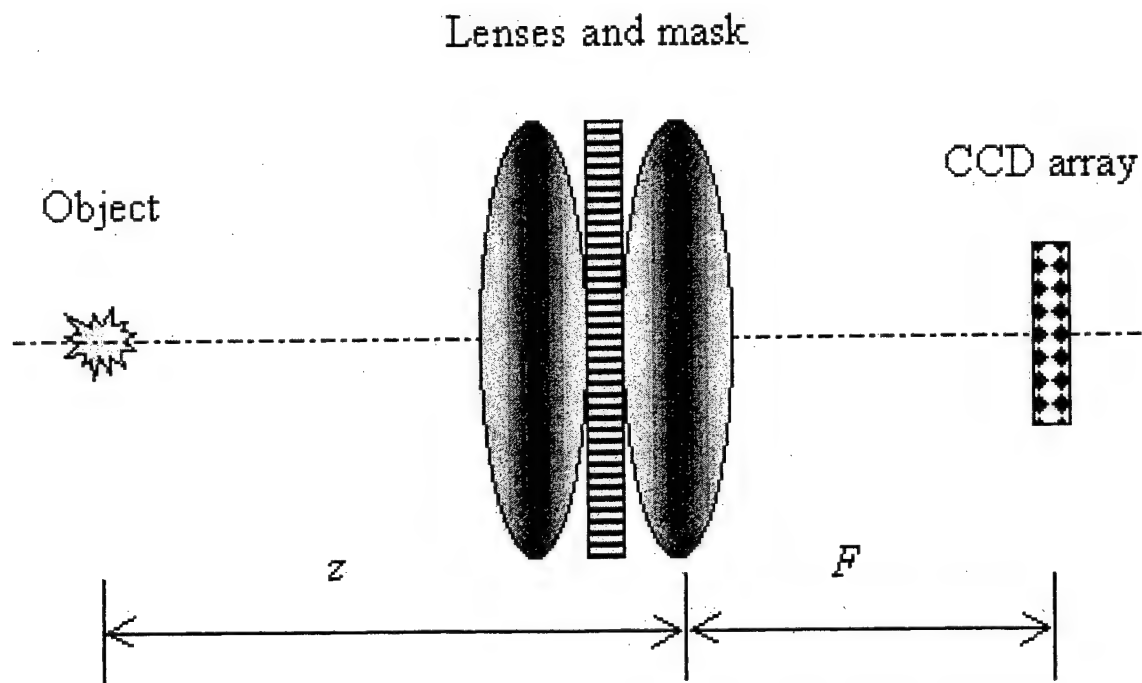


Figure 59: Schematic of an optical ranging system with wave-front coding. The phase-amplitude mask changes the transfer function of the system. The Fourier transform of the image will contain peaks that move out to the higher-order spatial modes as the range of the object increases.

in diameter), and the antenna elements are assumed to be low-gain with half-wavelength spacing. The mask is a simple cosine amplitude mask, similar to the one used in the optical system. The image surface is sampled by simulated detectors for varying object distance.

The ranging process is demonstrated for on-axis objects located 6λ and 10λ from the lens. The Fourier transform of axial slices from each image of Fig. 61 are given in Fig. 62 showing an expected peak at the zero spatial frequency, and additional peaks at higher order spatial modes. A mathematical analysis shows that the energy in these modes shifts to higher frequencies as the range of the object increases. This is demonstrated in Fig. 62 where the expected shift in spatial frequency of the image is clearly shown. In a working system, a calibration for the range is straightforward since the amount of frequency shift of a given peak is linear with the change in range. The same Fourier analysis can be done on the image patterns given for additional object distances shown in Figs. 63 and 64 where the object is progressed further from the lens.

In Figs. 61-64 the object is kept at bore-sight while the range is increased. When the

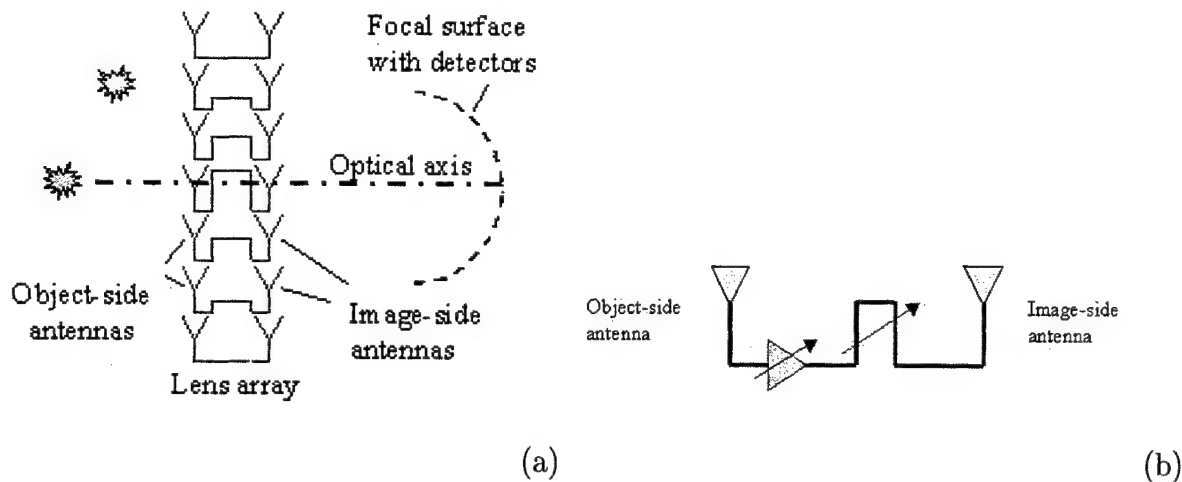


Figure 60: Schematic of millimeter-wave passive ranging front end (a) and a single element of a discrete lens antenna array (b). The delay and gain (or attenuation) vary between array elements. The variation can be modified for different masking functions.

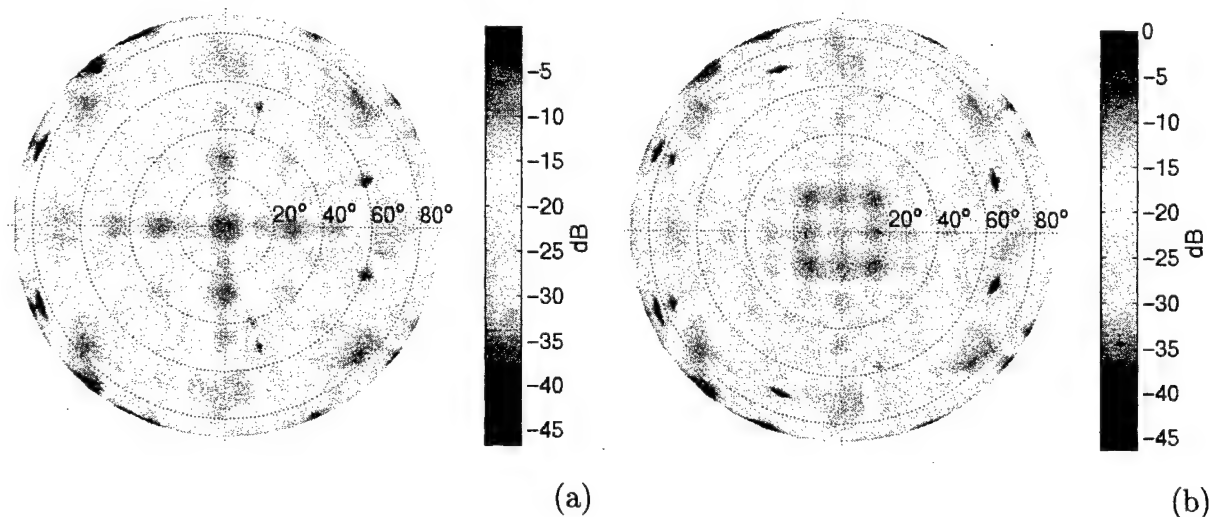


Figure 61: Simulation of images sampled by detectors positioned over the image surface of a 100-element lens with bore-sight object at 6 (a) and 10 (b) free-space wavelengths from a masked lens with half-wavelength period.

object is located at some angle with respect to the optical axis, the range on the image surface also shifts and the effects of aberrations become more pronounced as objects move off-axis.

In summary, we have performed simulations of a passive millimeter-wave ranging front end that uses wave-front coding to determine the range. Compared to the implementation in the optical region of the spectrum, there are several benefits to using this technique

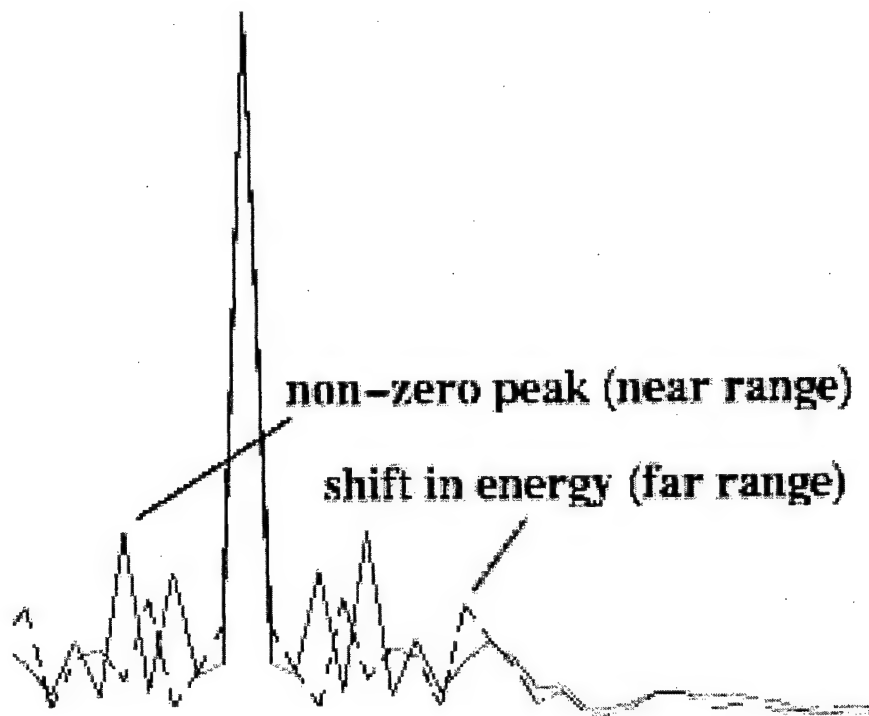


Figure 62: Fourier transforms of axial slices from the image patterns of Fig. 61. The shift in energy outward from the main peak (the zero-frequency peak) along the spatial frequency axis indicates an increase in range.

at millimeter wavelengths. In the optical implementation, the aperture efficiency suffers because roughly half of the mask is dark (absorptive), and the number of possible masks is limited. In the millimeter-wave region, the lens can be designed to have variable amplitude by using gain elements (amplifiers); but in principle, a pure phase mask with practically any phase variation can be coded into the delay lines of the discrete lens array. It should be noted, however, that a mask different from the cosine mask presented here can require a significantly different interpretation (and mathematical analysis) of the transfer functions of the images.^{25, 31}

The practicality of this technique depends on the required range and range resolution. The useful range is given by the size of the lens, so large lenses would be needed for large range requirements. The resolution depends on a number of factors, such as element spacing in the lens and detector spacing on the image plane. The implementation of the discrete lens at 94 GHz is amenable to photolithographic fabrication and there are a variety of appropriate antenna elements and guiding structures which have been developed in the past two decades that can be applied to this approach.^{32, 33} Possible detector arrays for sampling the image are Schottky diodes and bolometers.^{34, 35}

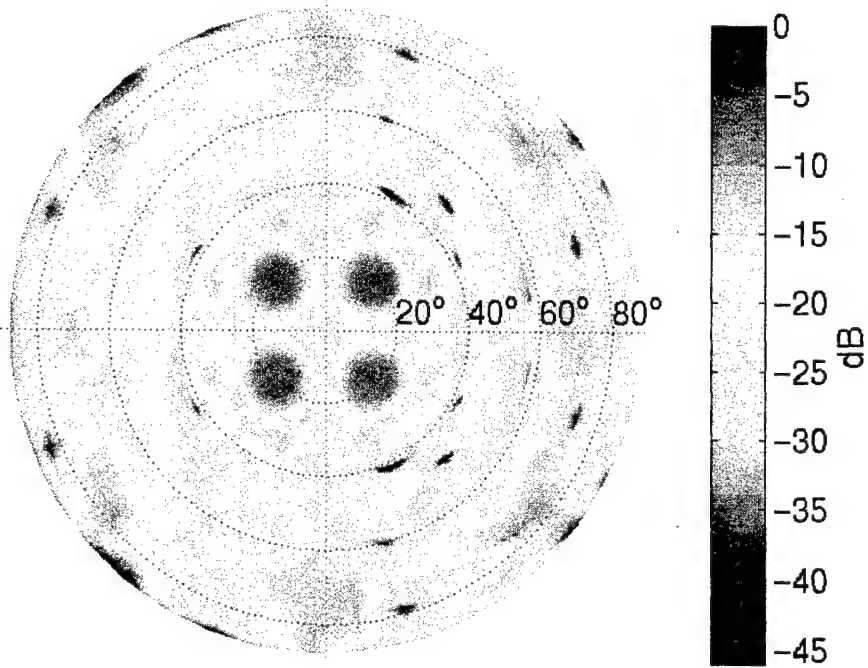


Figure 63: Simulation of image sampled by detectors positioned over the image surface of a 100-element lens with bore-sight object at 30 free-space wavelengths from a masked lens with half-wavelength period.

7.3 Summary of evaluation of progress based on plans from last year

1. Complete T/R QO front end

We have completed a 27-element optically switched half-duplex T/R lens array. There are two publications on this array, along with detailed discussions in Jim Vian's Ph.D. dissertation. If we choose to do a second iteration of such an array, we have now available a number of design tools and a solid worked-out design methodology for such QO components.

2. Integration of a QO front end with an operating photorefractive optical processor for signal extraction (with Prof. Anderson)

This has been accomplished. Details are in another part of the report, and results are submitted for publication in a special issue of IEEE Trans. on Antennas and Propagation. The rf front end was integrated with an optical processor for strongest independent signal component extraction and the system was successfully demonstrated at X-band (10 GHz) with a signal bandwidth of 10 MHz, limited by resonant high-efficiency EO modulators.

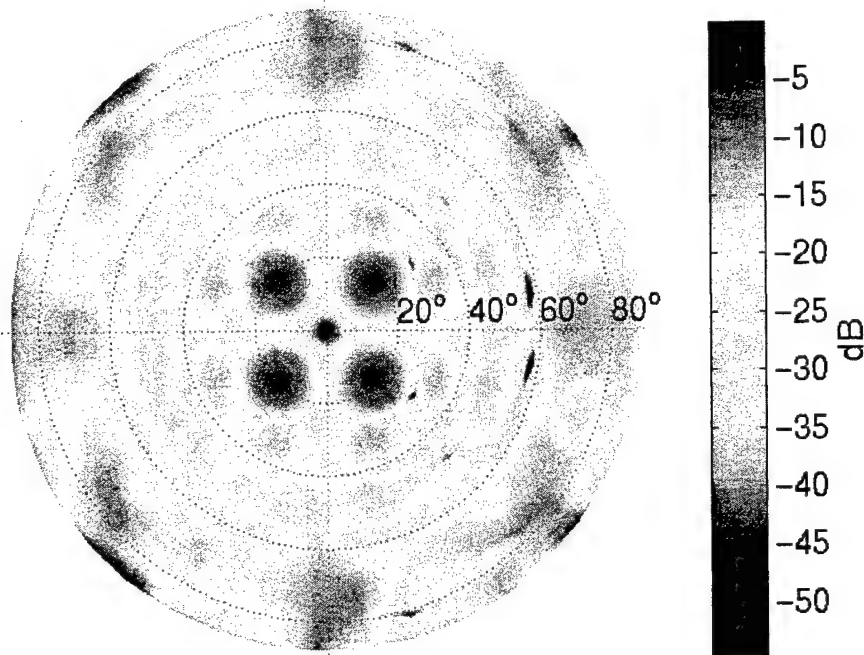


Figure 64: Simulation of image sampled by detectors positioned over the image surface of a 100-element lens with bore-sight object at 100 free-space wavelengths from a masked lens with half-wavelength period.

3. Investigation of adaptive algorithms as applied to lens arrays (with Prof. Griffiths)

This has been accomplished with an LMS adaptive algorithm and applied to interference and multi-user scenarios. The work was presented at the IEEE International Microwave Symposium in Phoenix, 2001. Technical details describing the results are presented in this report.

Continuing work resulting from this project includes application of a new MUSIC-type algorithm to lens antenna arrays for DOA (direction of arrival) estimation. This new work is funded by the German equivalent of NSF and is a collaboration with Prof. Russer at the Technical University in Munich.

4. Continue working on the front-end portion of arrays with optical processing to include feedback from the optical output to the RF front end.

The electronics at the IF. (downconverted RF to 100-200 MHz) stage in the current optically smart antenna includes variable gain amplifiers that provide up to 40 dB gain for each signal path, controlled by a feedback signal. The remaining portion of this task is to add a feedback loop from the optical output. Several other integration steps have been successfully implemented, as described in the relevant section of this report.

5. Apply some quasi-optical techniques developed under this project to systems other than radar. In particular, we are interested in passive millimeter-wave ranging that use QO lens arrays.

We have performed a theoretical study of the concept of applying QO antenna arrays at 94 GHz for passive ranging using a combination of analog and digital techniques. We have proven the feasibility of the approach and we are able to indicate some practical limitations. The results are published in the Proceedings of the 2001 European Microwave Conference. However, only one possible type of QO array was simulated, and many other similar designs could offer better performance. This, we hope will be a subject of a future project.

8 PILF modulators

PI Andre Knoesen, U.C. Davis, ECE – AMRFS/ACI subcontract

8.1 Introduction

The general objective of the research is to improve optical and electronic systems by focusing on the integration of wide bandwidth optical/electronic links using new materials and methods. Optically controlled phased arrays require optical/electronic interfaces operating at increasingly higher communication rates, with greater functionality and improved performance. This requires reliability, reduced size and weight in components, and most importantly a large spurious free dynamic range. Such characteristics can only be achieved by integrating high-speed electronic and optical components to obtain improved functionality and reliability.

At UC Davis we are investigating device concepts to integrate either compound semiconductors or electro-active polymers to passive waveguides, such as optical fibers, to implement advanced functions. Operating electro-optical components at high optical intensities is desirable in optically controlled phased arrays because photodetectors can be operated in shot-noise limited regime. In conventional electro-optic fiber devices, such as for example lithium niobate phase modulators, the optical intensities are limited to well less than 100 mW. This motivates our interest in devices where the optical beam propagates predominantly in a passive waveguide and interacts with an active region through evanescent fields. We have already demonstrated that asymmetric evanescent field coupling to an inorganic waveguide can be used to implement microwave amplitude modulators,³⁶ digital modulators,³⁷ filters,³⁸ detectors,³⁹ sources,⁴⁰ and most recently variable optical attenuators.

In this report we describe the investigation of a polymer inline fiber modulator (PILF) that uses evanescent coupling and is useful as an optical phase modulator. The anticipated application of these modulators is in coherent analog links used in optically controlled phased arrays. It should also be noted that the intended use of the phase modulator investigated in this research is in the transmitter, but it could also find use in an optical filter at the receiver.^{41,42}

The properties of the PILF are reviewed followed by a description of the optical phase modulator testing. An electromagnetic simulation of the phase modulation characteristic of the PILF is given. The results of a feasibility experiment are described next. The results of this experiment were encouraging and motivated the development of a new experimental

self-homodyne technique to measure the phase modulation in the modulators. The report concludes with a description of future work on phase modulation using the PILF.

8.2 PILF Modulator

8.2.1 Description

In 1989 Marcuse developed a coupled mode theory to model the coupling between an optical fiber and an infinite slab and analyzed to what extent the propagation constant can be modified.⁴³ To capture the subtleties of this coupling (e.g. adiabatic vs. non-adiabatic coupling) we have developed beam propagation method (BPM) models that simulate PILF's and accurately predict the device intensity modulation.⁴⁴ The PILF is shown schematically in Figure 1. The device is constructed in a similar fashion as our previous amplitude modulators.³⁶ A notable difference is that in order to form the high frequency electrode for this device the top gold layer is ablated using a laser to form a microstrip

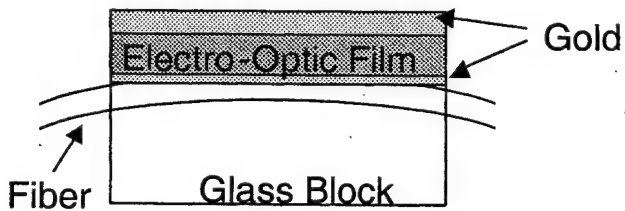


Figure 65: Schematic of PILF optical modulator

8.2.2 The PILF as a Phase Modulator

The phase of the mode propagating in a passive waveguide can be modulated by changing the index of refraction of an electro-optic thin film waveguide placed in close proximity to a passive waveguide. An electromagnetic coupling takes place between the two dissimilar waveguides when the phase velocity of the modes propagating in the individual waveguides is approximately equal. We used this asymmetric coupling to modulate the phase of the mode propagating in the passive waveguide. Previously in our group we have demonstrated 10 GHz+ intensity modulators that consist of asymmetric coupling between a single mode glass fiber to an electro-optic polymer thin films. In this research we are exploring the phase modulation characteristics of a similar device structure.

8.2.3 Simulation of PILF as a Phase Modulator

We have adapted the BPM models for PILF structures to model the phase shift in an inline fiber configuration consisting of a single mode fiber coupled at $\lambda = 1.5\mu$ m to a thin (2.2μ m) electro-optic polymer slab with an r_{33} of 50pm/Volt. The simulation results shown in Figure 2 indicate that a 10 degree phase shift can be expected for an applied voltage of 5V with an interaction length on the order of 500um. Longer interaction lengths do not increase the phase shift because the spacing between the fiber and the polymer slab increases to the point that there is no additional effect from the increase in slab length. The result demonstrated that angle modulation is possible with the PILF and stimulated feasibility experiments to verify and finally quantify the phase modulation.

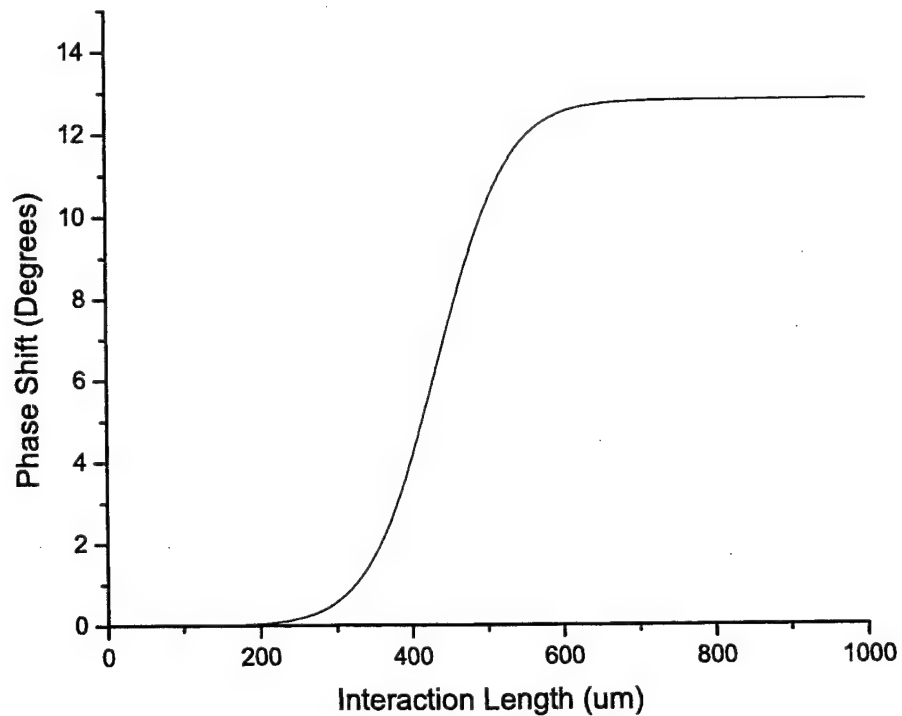


Figure 66: BPM simulation of phase shift versus interaction length for a 5V applied signal

8.3 Feasibility Experiment

8.3.1 Description

Unlike an interferometer, such as a Mach-Zehnder, where there is a reference arm, directly measuring the phase shift in a single waveguide at optical wavelengths is difficult. For the purposes of a feasibility experiment the presence of a phaseshift in a PILF modulator is observed indirectly by detecting a polarization change. The test set up is shown in figure 3. A tunable fiber coupled laser is used and the wavelength is set to the operating wavelength of the PILF modulator. A fiber compensator is used to launch a linear polarization into the region where evanescent coupling occurs. The polarization is set so that both TE and TM components are launched and only the TM component is modulated. The output is collimated then passes through the analyzer and is focused onto the detector. The detector output is measured by a voltmeter, to determine the dc value, and by a lock in amplifier to determine the signal value.

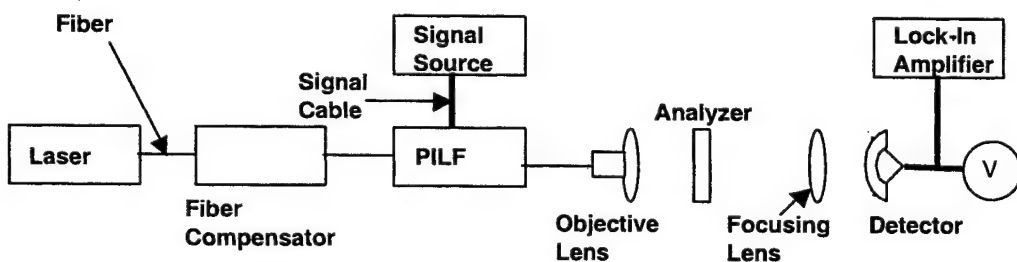


Figure 67: Simple feasibility experiment to determine if an optical phase shift is present

8.3.2 Results

If only amplitude modulation is present then the DC voltage measured on the detector and the signal voltage measured by the lock-in amplifier will have the same functional dependence on the analyzer angle and any deviation from this would indicate angle modulation. In Figure 4 is shown the DC voltage (left side axis) and the lock-in amplifier signal (right side axis) as a function of the analyzer angle. The occurrence of phase modulation is indicated by two important characteristics: 1) The angle of polarization where the detector

output is maximum is not the same as the angle for signal maximum 2) The phase of the modulated signal is negative at the minimums. This shows that the output is no longer a linearly polarized signal resulting from the sum of two in phase components. Instead it is an elliptically polarized signal due to the phase shift introduced in the TM polarization by the modulator.

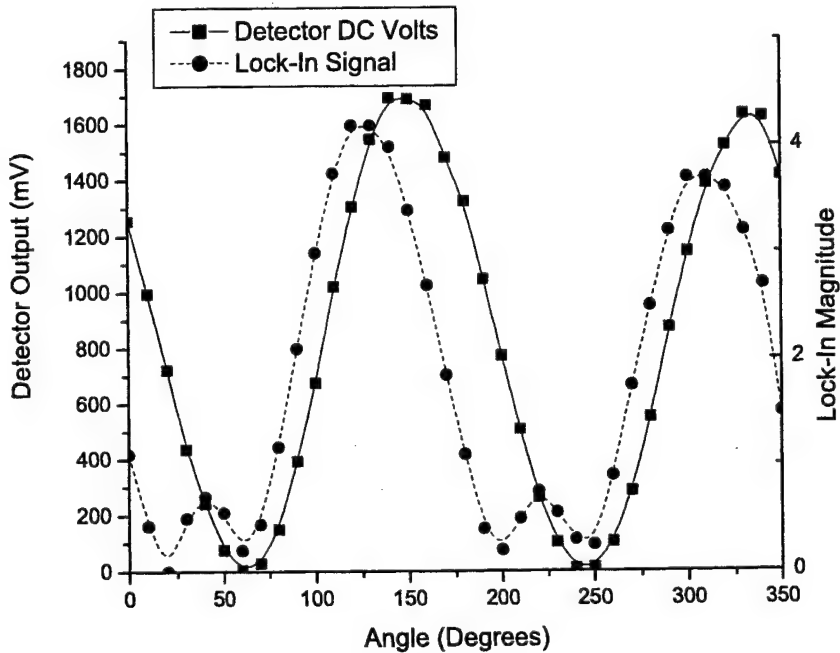


Figure 68: Phase modulation in PILF structure. DC voltage measured by the detector and the signal voltage measured by the lock-in amplifier as a function of analyzer angle.

8.4 Self-Homodyne Phase Measurement Method

In the feasibility experiment the phase shift was inferred from the change in the polarization. While adequate for proof of concept, a direct method of detecting the phase shift is needed. We have developed a self-homodyne measurement technique to accurately measure the phase shift in single arm phase modulators.

8.4.1 Description

The modulation efficiency is determined by measuring the spectrum of the modulated carrier mixed with an unmodulated signal of the same optical frequency. The spectrum depends on the form of the applied modulation and for a modulating voltage of $a \cdot \cos(\omega t)$ is

$$S(\omega) = A \sum_{n=-\infty}^{\infty} J_n(k_p a) \delta(n\omega_m)$$

where A is a constant, J_n is a Bessel function of the first kind and of order n , k_p is the phase shift/volt, δ is the Kronecker delta function, and ω_m is the modulation frequency. The spectrum is measured by a self-homodyne receiver that uses a tunable solid state laser. A portion of the optical carrier is split off and phase modulated, then recombined with the remaining carrier at the photodetector. The phaseshift/volt (k_p) is determined by analyzing the ratios between the harmonics in the spectrum. The measurement system is shown in figure 5. The output of the laser is divided into two paths; the modulated path and the delayed path. In the modulated path the light is passed through a fiber compensator that is used to set the polarization into the inline phase modulator. The sine wave signal is applied to the modulator with a frequency significantly higher than the laser linewidth. A second splitter recombines the modulated path and the delayed path in the high speed photodetector. The uncertainty principle requires that $\Delta t \Delta f$ must be greater than or equal to a constant and to improve the frequency resolution a time delay is used. A fiber delay line introduces the required time delay. A compensator sets the polarization of the delayed path so that both paths are aligned, to optimize the mixing which takes place in the photodiode. The resulting baseband signal is filtered and measured by the microwave spectrum analyzer.

8.4.2 Results

The measurement system was verified by determining the amount of optical phase shift that occurred in a commercially available narrowband modulator. The applied modulation signal was a 10 MHz sine wave with peak voltages ranging from 1 to 10V. The first four harmonics of the output signal measured by the microwave spectrum analyzer are plotted versus the applied modulation voltage in Figure 6.

It can be shown that the ratio of the magnitudes of any of the harmonics is equal to the ratio of Bessel functions of the first kind of order n , where n is the number of the harmonic.

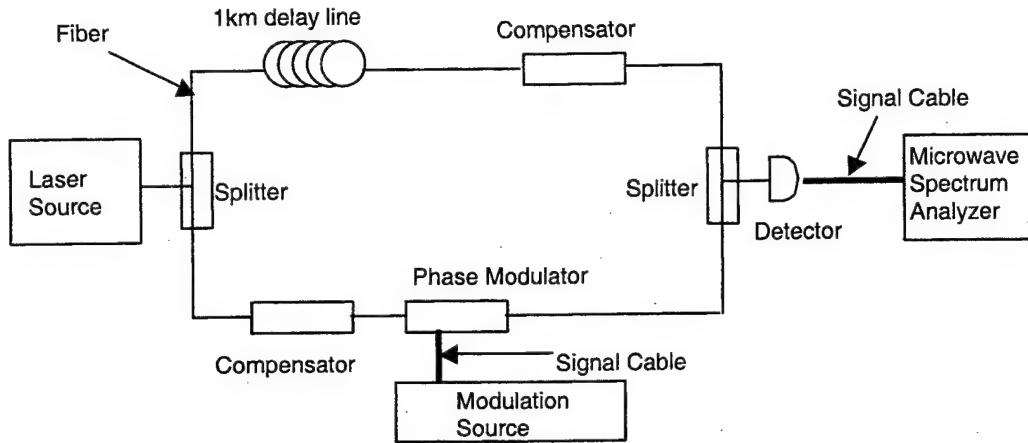


Figure 69: Self Homodyne Phase Modulation Measurement method

$$\frac{V_m}{V_n} = \frac{J_m\left(\pi \frac{V_{mod}}{V_{pi}}\right)}{J_n\left(\pi \frac{V_{mod}}{V_{pi}}\right)}$$

where $V_{m,n}$ is the magnitude of the harmonic m,n, $J_{m,n}$ is the Bessel Function of the first kind of order m,n, V_{mod} is the applied modulation voltage and V_{pi} is the voltage that produces a phase shift of π .

The V_{pi} is determined by numerically solving the previous equation and using measurements of $V_{m,n}$. The values for V_{pi} were calculated over the modulation voltage range from 6 to 8 volts. The value for V_{pi} in this region was measured as 6.78V with a standard deviation of .054.

8.5 Future Work

It has been shown by simulation and experiment that phase modulation in a PILF modulator is competitive with broadband commercial inline modulators. A new self homodyne phase measurement technique was developed to quantify the phase modulation. Measured values using this method demonstrated great consistency by measuring the phase shift within ± 0.1 radians. A PILF has been made for operation at $\lambda = 1.55\mu$ m. After completing the phase measurement of the PILF, further work on evanescently coupled phase modulators will focus on integrated optical channel waveguides and thin polymer films. The measurement technique developed for the PILF phase modulator will be used to evaluate the waveguide

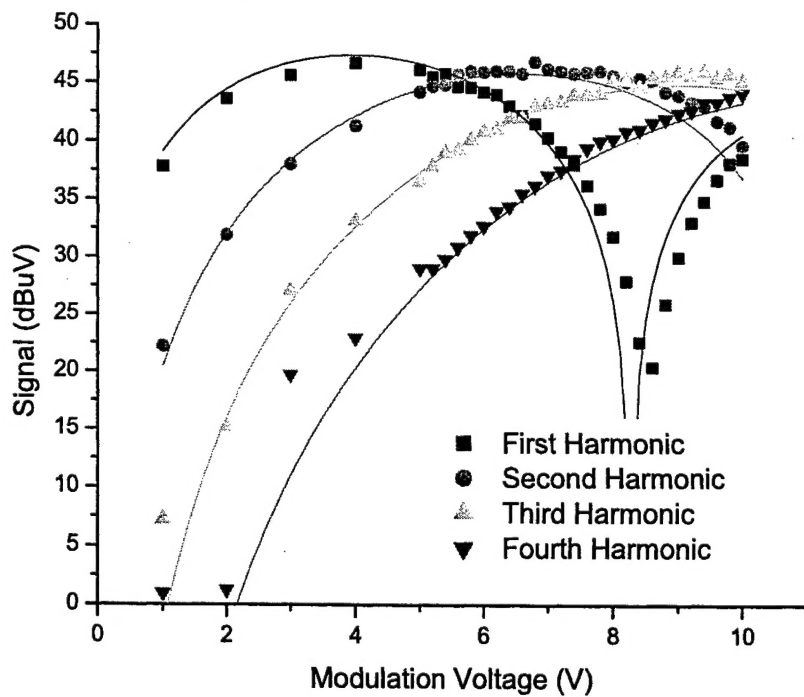


Figure 70: Experimental data compared to the theoretical values (solid lines) for the Self Homodyne Phase Modulation Measurement on the commercial modulator

devices.

References

- [1] A. W. Sarto, K. H. Wagner, R. T. Weverka, S. Weaver, and E. K. Walge, "Wide angular aperture holograms in photorefractive crystals by the use of orthogonally polarized write and read beams," *Applied Optics*, vol. 35, no. 29, pp. 5765–5775, 1996.
- [2] E. Paek, Y. Im, J. Choe, and T. Oh, "Acoustically steered and rotated true-time-delay generator based on wavelength-division multiplexing," *Applied Optics*, vol. 39, pp. 1298–1308, 2000.
- [3] D. Dolfi, T. Merlet, A. Mestreau, and J. P. Huignard, "Photodetector for microwave signals based on the synchronous drift of photogenerated carriers with a moving interference pattern," *App. Phys. Lett.*, vol. 65, pp. 2931–2933, 1994.
- [4] T. Merlet, D. Dolfi, and J. P. Huignard, "A traveling fringes photodetector for microwave signals," *IEEE JQE*, vol. 32, pp. 778–783, 1996.
- [5] G. Kriehn, A. M. Kiruluta, K. H. Wagner, D. Dolfi, and J.-P. Huignard, "Detection of a broadband rf signal using a traveling fringes detector," in *Terahertz and Gigahertz Photonics*, vol. 3795, Proc. SPIE, July 1999.
- [6] M. Y. Frankel and R. D. Esman, "True time-delay fiberoptic control of an ultrawide-band array transmitter receiver with multibeam capability," *IEEE Trans. MTT*, vol. 43, pp. 2387–2394, 1995.
- [7] M. Y. Frankel, P. J. Matthews, and R. D. Esman, "Fiberoptic true time steering of an ultrawide-band receive array," *IEEE Trans. MTT*, vol. 45, pp. 1522–1526, 1997.
- [8] P. Andrekson, N. A. Olsson, T. Tanbun-Ek, and M. Washington, "High power semiconductor laser injection locking at $1.3 \mu\text{m}$," *J. Light. Tech.*, vol. 10, no. 7, pp. 903–907, 1992.
- [9] T. B. Simpson, J. M. Liu, A. Gavrielides, V. Kovanis, and P. M. Alsing, "Period-doubling cascades and chaos in a semiconductor laser with optical injection," *Phys. Rev. A*, vol. 51, pp. 4181–85, 1995.
- [10] M. P. van Exter, W. A. Hamel, J. P. Woerdman, and B. R. P. Zeijlmans, "Spectral signature of relaxation oscillations in semiconductor lasers," *IEEE J. Quantum Electron.*, vol. 28, pp. 1470–78, 1992.
- [11] V. Kovanis, A. Gavrielides, T. Simpson, and J. M. Liu, "Instabilities and chaos in optically injected semiconductor lasers," *Appl. Phys. Lett.*, vol. 67, pp. 2780–82, 1995.
- [12] J. Troger, P. A. Nicati, L. Thevanaz, and P. A. Robert, "Novel measurement scheme for injection-locking experiments," *IEEE J. Quantum Electron.*, vol. 35, pp. 32–38, 1999.
- [13] K. Merkel and W. Babbitt, "Chirped-pulse programming of optical coherent transient true-time delays," *Optics-Letters*, vol. 23, pp. 528–30, 1998.
- [14] R. Reibel, Z. Barber, M. Tian, and W. R. Babbitt, "Temporally overlapped linear frequency chirped pulse programming for true-time-delay applications," *Opt. Lett.*, vol. To

- be published, March 2002.
- [15] R. D. Peters, "Programming high bandwidth true-time delays in an optical coherent transient material," *Research Paper, Department of Physics, Montana State University*, 2001.
 - [16] M. Tian, J. Zhao, Z. Cole, R. Reibel, and W. R. Babbitt, "Dynamics of broadband accumulated spectral gratings in $\text{tm}^{3+}:\text{yag}$," *J. Opt. Soc. Am. B*, vol. 18, pp. 673–78, May 2001.
 - [17] K. Merkel, R. Peters, P. Sellin, K. Repasky, and W. Babbitt, "Accumulated programming of a complex spectral grating," *Optics-Letters*, vol. 25, pp. 1627–9, 2000.
 - [18] E. Gazit, "Improved design of the vivaldi antenna," *IEE Proceedings*, pp. 89–92, 1988.
 - [19] G. Kriehn, A. Kiruluta, P. E. X. Silveira, S. Weaver, S. Kraut, K. Wagner, R. T. Weverka, and L. Griffiths, "Optical BEAMTAP beam-forming and jammer-nulling system for phased-array antennas," *Applied Optics*, pp. 212–230, 2000.
 - [20] B. Widrow, P. E. Mantey, L. J. Griffiths, and B. B. Goode, "Adaptive antenna systems," *Proc. of the IEEE*, vol. 55, no. 12, pp. 2143–2161, 1967.
 - [21] F. Schlottau and K. Wagner, "RF photonics for simultaneous multiple TTF beamforming for 2-D antenna arrays," in *MWP '01*, IEEE, 2001.
 - [22] Z. Popović and A. Mortazawi, "Quasi-optical transmit/receive arrays," *IEEE Trans. Microwave Theory Tech.*, vol. 45, pp. 1964–1975, Oct. 1998.
 - [23] D. Anderson, V. Damiao, E. Fotheringham, D. Popovic, S. Romisch, and Z. Popovic, "Optically smart active antenna arrays," *2000 IEEE IMS Symposium Digest*, vol. 2, pp. 843–846, 2000.
 - [24] R. W. Hardin, "Passive millimeter wave technology keeps the skies safe," *The International Society for Optical Engineering Magazine*, Apr. 2000.
 - [25] G. Johnson, E. Dowski, and W. Cathey, "Passive ranging through wave-front coding: information and application," *Applied Optics*, vol. 39, pp. 1700–1710, Apr. 2000.
 - [26] A. Werthof, T. Gravem, and W. Kellner, "W-band amplifier fabricated by optical stepper lithography," *IEEE MTT-S Int. Microwave Symp. Dig.*, pp. 689–692, June 1999.
 - [27] Y. C. Leong and S. Weinreb, "Full W-band MMIC medium power amplifier," *IEEE MTT-S Int. Microwave Symp. Dig.*, pp. 951–954, June 2000.
 - [28] D. L. Ingram, Y. C. Chen, I. Stones, B. Brunner, P. Huang, M. Biedenbender, J. Elliott, R. Lai, D. C. Streit, K. F. Lau, and H. C. Yen, "Compact W-band solid-state MMIC high power sources," *IEEE MTT-S Int. Microwave Symp. Dig.*, pp. 955–958, June 2000.
 - [29] J. Vian and Z. Popović, "Smart lens antenna arrays," *IEEE MTT-S Int. Microwave Symp. Dig.*, pp. 129–132, 2001.
 - [30] M. A. Forman, J. Vian, and Z. Popović, "A K-band full-duplex transmit-recieve lens array," *IEEE MTT-S Int. Microwave Symp. Dig.*, pp. 1831–34, 2001.

- [31] K. Brenner, A. Lohmann, and J. Ojeda-Castaneda, "The ambiguity function as a polar display of the OTF," *Optics Communications*, vol. 44, pp. 323–326, Oct. 1982.
- [32] G. P. Gauthier, J. P. Raskin, and L. P. B. K. et al., "A 94 GHz micromachined microstrip antenna," *IEEE Trans. Ant. and Prop.*, vol. 47, pp. 1761–1766, Dec. 1999.
- [33] V. M. Lubecke, K. Mizuno, and G. M. Rebeiz, "Micromaching for terahertz technology," *IEEE Trans. Microwave Theory Tech.*, vol. 46, pp. 1821–1831, Nov. 1998.
- [34] D. P. Neikirk, W. W. Lam, and D. B. Rutledge, "Far-infrared microbolometer detectors," *International Journal of Infrared Millimeter Waves*, vol. 5, pp. 245–278, 1984.
- [35] C. Zah, D. P. Kasilingam, J. S. Smith, D. B. Rutledge, T. Wang, and S. E. Schwartz, "Millimeter-wave monolithic Schottky diode imaging arrays," *International Journal of Infrared Millimeter Waves*, vol. 6, pp. 981–987, 1985.
- [36] S. Hamilton, D. Yankelevich, A. Knobles, R. Weverka, R. Hill, and G. Bjorklund, "Polymer in-line fiber modulators for broadband radio-frequency optical links," *Journal of the Optical Society of America B (Optical Physics)*, vol. 15(2), pp. 740–50, 1998.
- [37] E. Mao, C. Coldren, J. Harris, D. Yankelevich, O. Solgaard, and A. Knobles, "Gaas/AlGaAs multiple-quantum-well in-line fiber intensity modulator," *Applied Physics Letters*, vol. 75(3), pp. 310–312, 1999.
- [38] E. Mao, C. Coldren, J. S. Harris, D. Yankelevich, O. Solgaard, and A. Knobles, "Gaas/AlGaAs narrow-bandwidth in-line fiber filter," 1999.
- [39] E. Mao, D. Yankelevich, C. Lin, O. Solgaard, A. Knobles, and J. S. Harris, "Wavelength-selective semiconductor in-line fibre photodetectors," *Electronics Letters*, vol. 36(6), pp. 515–16, 2000.
- [40] E. Mao, D. Yankelevich, C. Lin, O. Solgaard, A. Knobles, and J. H. Jr., "Narrow-band light emission in semiconductor-fibre asymmetric waveguide coupler," *Electronics Letters*, vol. 36(16), pp. 1378–9, 2000.
- [41] D. Davies and G. James, "Fibre-optic tapped delay line filter employing coherent optical processing," *Electronics Letters*, vol. 20(2), pp. 95–7, 1984.
- [42] K. Jackson, X. Guoging, and H. Shaw, "Coherent optical fibre delay-line processor," *Electronics Letters*, vol. 22(25), pp. 1335–7, 1986.
- [43] D. Marcuse, "Investigation of coupling between a fiber and an infinite slab," *Journal of Lightwave Technology*, vol. 7(1), pp. 122–30, 1989.
- [44] C. Arft, D. Yankelevich, A. Knobles, E. Mao, and J. S. Harris, "In-line fiber evanescent field electrooptic modulators," 2000.